New NMR Tools for Impurity Analysis

A thesis submitted to the University of Manchester for the Degree of Doctor
Philosophy in the Faculty of Engineering and Physical Sciences

2016

Jane Elizabeth Power

School of Chemistry

The University of Manchester

List of Contents

List of Figures

List of Tables

List of Abbreviations and Symbols

ABSTRUSE	Adjustable, Sech/Tanh-Rotation Uniform Selective Excitation
ADC	Analogue-to-Digital Converter
AFP	Adiabatic Full Passage
AHP	Adiabatic Half Passage
AM	Amplitude Modulation
$A\ (\omega)$	real Absorption Lorentzian lineshape of signal
AZ	AstraZeneca
$\boldsymbol{B}_0$	static magnetic field (tesla)
B_1	radiofrequency magnetic field (tesla)
B_{eff}	effective magnetic field (tesla)
BPPSTE	Bipolar Pulse Pair Stimulated Echo
bw	bandwidth (Hz)
CASE (award)	Co-operative Award in Pure Science and Engineering
CHORUS	CHirped, Ordered Pulses for Ultra-broadband Spectroscopy
COSY	COrrelation SpectroscopY
CPMG	Carr-Purcell-Meiboom-Gill spin echo sequence
CSA	Chemical Shift Anisotropy
CTP	Coherence Transfer Pathway
CYCLOPS	Cyclically-ordered phase sequence for quadrature detection
D	Diffusion coefficient ($\times\ 10^{-10}$ m^2 s^{-1})
1D	one-Dimensional
2D	two-Dimensional
dmf	decoupler modulation frequency (Hz)
DOSY	Diffusion-Ordered SpectroscopY
$D\ (\omega)$	Dispersion Lorentzian lineshape of signal
DW	DWell time (s)
EPSRC	Engineering and Physical Sciences Research Council
EXORCYCLE	phase cycle to suppress phantom and ghost signals

ΔF	total sweep width (for swept-frequency chirp pulses) (Hz)
4FBA	4-FluoroBenzoic Acid
FID	Free Induction Decay
FIDDLE	Free Induction Decay Deconvolution for Lineshape Enhancement
FM	Frequency Modulation
f_{max}	frequency sweep (for HS pulses) (Hz)
f_{r}	friction factor
FT	Fourier Transform
G	pulsed field Gradient amplitude (G cm^{-1})
h	Planck constant (= 6.26×10^{-34} J s)
$\hbar$	reduced Planck constant (Planck constant divided by 2π) (= 1.055×10^{-34} J s)
$\widehat{H}$	the Hamiltonian Operator
HS	Hyperbolic Secant
i	imaginary number ($\sqrt{-1}$)
I	nuclear spin quantum number
$\hat{I}$	operator for spin angular momentum for spin I
$\hat{I}_{i+}$	raising product operator
$\hat{I}_{i-}$	lowering product operator
INADEQUATE	Incredible Natural Abundance Double Quantum Transfer Experiment
INEPT	Insensitive Nuclei Enhanced by Polarization Transfer
J	scalar coupling constant (Hz)
k	a factor which defines the threshold for adiabaticity (for HS pulses)
k_{B}	Boltzmann constant (= 1.38×10^{-23} J K^{-1})
LB	Line Broadening
m	nuclear magnetic quantum number
M	net Magnetisation vector
M_0	equilibrium net Magnetisation vector
M_z	z component of M

M_{xy}	transverse component of M
M_s	total spin quantum number
N	Number of spins
NaTrif	sodium trifluoromethanesulfonate
NMR	Nuclear Magnetic Resonance
NOESY	Nuclear Overhauser Effect Spectroscopy
O1p	spectrometer operating frequency (ppm)
p	coherence order
$\boldsymbol{P}$	quantized intrinsic angular momentum
PFG	Pulsed Field Gradient
PFGSE	Pulsed Field Gradient Spin Echo
PFGSTE	Pulsed Field Gradient Stimulated Echo
PM	Phase Modulation
pw	(90°) pulse width (μs)
Q	adiabaticity factor
q^2	gradient pulse area
qNMR	quantitative NMR
R_1	longitudinal Relaxation rate (s^{-1})
R_2	transverse Relaxation rate (s^{-1})
RF, rf	RadioFrequency
r_s	hydrodynamic radius for a spherical particle in a continuum solution
RSD	Relative Standard Deviation
S	Signal intensity
SNR (or S/N)	Signal-to-Noise-Ratio
SW	Spectral Width (Hz)
S(q)	net attenuation of Signal, which shows a Gaussian dependence on q
T	Temperature (K)
T_1	longitudinal relaxation time constant (s)
T_2	transverse relaxation time constant (s)

T_2^*	effective relaxation Time including contributions from T_2 and T_{inhom} (s)
T_{inhom}	relaxation Time constant contribution due to B_0 field inhomogeneities (s)
TDSE	Time-Dependent Schrödinger Equation
TMS	TetraMethylSilane (chemical shift reference compound)
t_1	incremented time in 2D experiments (s)
T_{p}	pulse duration (s)
WALTZ	decoupling sequence
$W_{\text{G}}(t)$	Gaussian Weighting function
$W_{\text{LB}}(t)$	exponential Weighting function used for Line Broadening
$W_{\text{RE}}(t)$	exponential Weighting function used for Resolution Enhancement
WURST	decoupling sequence using adiabatic pulses
α	the lower energy state of a spin (+1/2) nucleus, aligned with $\boldsymbol{B}_0$ for positive γ
β	the higher energy state of a spin (−1/2) nucleus, aligned against $\boldsymbol{B}_0$ for positive γ
δ	chemical shift (ppm) <u>or</u> diffusion encoding / decoding PFG duration (ms)
η	dynamic viscosity
Δ	diffusion delay (s)
Δ'	effective diffusion delay corrected for gradient pulse width (s)
φ	phase of pulse
γ	gyromagnetic ratio (also referred to as magnetogyric ratio) (rad $\text{T}^{-1}\text{s}^{-1}$)
$\hat{\rho}$	density operator
ψ	wavefunction of a spin
$\boldsymbol{\mu}$	nuclear magnetic moment or magnetic dipole
ν_0	Larmor frequency (Hz)
ν_{ref}	reference frequency (Hz)
ω	angular frequency (in rad / s)

Abstract

New NMR Tools for Impurity Analysis was written by Jane Power and submitted for the degree of Doctor of Philosophy in the Faculty of Engineering and Physical Sciences at the University of Manchester, on 31st March 2016.

NMR spectroscopy is rich in structural information and is a widely used technique for structure elucidation and characterization of organic molecules; however, for impurity analysis it is not generally the tool of choice. While ^{1}H NMR is quite sensitive, due to its narrow chemical shift range (0 - 10 ppm) and the high abundance of hydrogen atoms in most drugs, its resolution is often poor, with much signal overlap. Therefore, impurity signals, especially for chemically cognate species, are frequently obscured.

^{19}F NMR on the other hand offers extremely high resolution for pharmaceutical applications. It exhibits far wider chemical shift ranges (± 300 ppm) than ^{1}H NMR, and typical fluorinated drugs, of which there are many on the market, have only one or two fluorine atoms. In view of this, ^{19}F NMR is being considered as an alternative for low-level impurity analysis and quantification, using a chosen example drug, rosuvastatin.

Before ^{19}F NMR can be effectively used for such analysis, the significant technical problem of pulse imperfections, such as sensitivity to B_1 inhomogeneity and resonance-offset effects, has to be overcome. At present, due to the limited power of the radiofrequency amplifiers, only a fraction of the very wide frequency ranges encountered with nuclei such as fluorine can be excited uniformly at any one time.

In this thesis, some of the limitations imposed by pulse imperfections are addressed and overcome. Two new pulse sequences are developed and presented, CHORUS and CHORUS Oneshot, which use tailored, ultra-broadband swept-frequency chirp pulses to achieve uniform constant amplitude and constant phase excitation and refocusing over very wide bandwidths (approximately 250 kHz), with no undue B_1 sensitivity and no significant loss in sensitivity.

CHORUS, for use in quantitative NMR, is demonstrated to give accuracies better than 0.1%. CHORUS Oneshot, a diffusion-ordered spectroscopic technique, exploits the exquisite sensitivity of the ^{19}F chemical shift to its local environment, giving excellent resolution, which allows for accurate discrimination between diffusion coefficients with high dynamic range and over very wide bandwidths.

Sulfur hexafluoride (SF_6) is investigated and shown to be a suitable reference material for use in ^{19}F NMR. The bandshape of the fluorine signal and its satellites is simple, without complex splitting patterns, and therefore good for reference deconvolution; in addition, it is sufficiently soluble in the solvent of choice, DMSO-d_6.

To demonstrate the functionality of the CHORUS sequences for low-level impurity analysis, 470 MHz ^{1}H decoupled ^{19}F spectra were acquired on a 500 MHz Bruker system, using a degraded sample of rosuvastatin, to reveal two low-level impurities.

Using a standard Varian probe with a single high frequency channel, simultaneous ^{1}H irradiation and ^{19}F acquisition was made possible by time-sharing. Simultaneous ^{19}F{^{1}H} and ^{19}F{^{13}C} double decoupling was then performed using degraded and fresh samples of rosuvastatin, to reveal three low-level impurities (in the degraded sample) and low-level ^{1}H and ^{13}C modulation artefacts.

Declaration

The author hereby declares that all the work presented in this thesis has been completed at the premises of The University of Manchester; in addition, the author declares that no portion of the work has been submitted in support of an application for another degree or qualification for this or any other university or other institute of learning. AstraZeneca and the EPSRC, through an Industrial CASE Studentship, supported this work.

Copyright Statement

i. The author of this thesis (including any appendices and/or schedules to this thesis) owns certain copyright or related rights in it (the “Copyright”) and she has given The University of Manchester certain rights to use such Copyright, including for administrative purposes.

ii. Copies of this thesis, either in full or in extracts and whether in hard or electronic copy, may be made only in accordance with the Copyright Designs and Patents Act 1988 (as amended) and regulations issued under it or, where appropriate, in accordance with licensing agreements which the University has from time to time. This page must form part of any such copies made.

iii. The ownership of certain Copyright, patents, designs, trade marks and other intellectual property (the “Intellectual Property”) and any reproductions of copyright works in the thesis, for example graphs and tables (“Reproductions”), which may be described in this thesis, may not be owned by the author and may be owned by third parties. Such Intellectual Property and Reproductions cannot and must not be made available for use without the prior written permission of the owner(s) of the relevant Intellectual Property and/or Reproductions.

iv. Further information on the conditions under which disclosure, publication and commercialisation of this thesis, the Copyright and any Intellectual Property and/or Reproductions described in it may take place is available in the University IP Policy (see http://documents.manchester.ac.uk/DocuInfo.aspx?DocID=487), in any relevant Thesis restriction declarations deposited in the university library, the university library’s regulations (see http://www.manchester.ac.uk/library/aboutus/regulations) and in the university’s policy on Presentation of Theses.

Acknowledgements

I would like to acknowledge, sincerely and with heartfelt thanks, my academic supervisors, Prof. Gareth A. Morris and Dr. Mathias Nilsson. The PhD has been an incredible journey, which without their support would not have been possible. They have made themselves available at all times (despite their own busy schedules) to give freely of their expertise and knowledge, offering their guidance, support and patience. This acknowledgment must be extended to my industrial supervisors Dr. Steven R. Coombes and Dr. Andrew R. Phillips. They have allowed me to work at their premises for many hours at a time, offering patience and humour, helping me to keep the PhD on track with a sense of perspective!

It has been a pleasure, a valuable and most enjoyable experience, being part of the Manchester NMR Methodology Group, working alongside undergraduate, postgraduate and post-doctoral colleagues. In particular, I would like to thank Dr. Mohammadali Foroozandeh; he has been inspirational at times, offering depth and guidance to certain aspects of the work. In addition, I would like to thank Dr. Ralph Adams and Dr. Iain Swan, who have also given freely of their advice and support.

Thanks must go to the School of Chemistry and The University of Manchester for excellent facilities and accessibility to secure “out of hours” access. The environment lends itself well for learning, encouraging dedication and focus to work.

Finally, I would like to thank my children for the sacrifices they have had to make without Mum being around as much as they would like; and of course, my parents (Grandma and Grandad), what would we have done without them!

“I read a book -

somewhere within the book

an insect chirps”

Tomiyasu Fūsei

Chapter 1

Introduction

1. Introduction

NMR uses the principle of angular momentum or ‘spin’ and its associated nuclear magnetic moment. Spin, in the microscopic world of elementary particles such as electrons and nucleons, is a difficult property to conceptualize. This is not an angular momentum related to motion, such as an electron orbiting the nucleus, as in classical mechanics, but an intrinsic property of a particle.[1] In 1922, Stern and Gerlach performed an experiment to test the theory of space quantization;[2] it is in this work that the concept of ‘spin’ was first demonstrated. The experiment involved passing a beam of silver atoms in a vacuum through an inhomogeneous magnetic field: the result observed was a two-fold splitting of the beam.[2-4] Classical mechanics would have predicted one beam, broader and with no deflection.[2, 3] The beam splitting confirmed the quantum mechanical theory: quantization in space with discrete energy levels.[1]

In 1925 Uhlenbeck and Goudsmidt theorized that the beam splitting, known as the Stern-Gerlach effect, was due to the electron having ‘spin’, and, implicit with the spin, quantized angular momentum.[2] This was later rationalised in 1928 by Dirac, who derived the relativistic quantum theory for a hydrogen atom that has spin-1/2 for both the electron and proton.[1, 3] Exploiting the principle intrinsic nuclear spin of a proton and its associated nuclear magnetic moment, the first NMR signals were observed. The discovery was made independently in 1945 by Bloch, Hansen and Packard at Harvard University,[5] and by Purcell, Torrey and Pound from Stanford University;[6] Bloch and Purcell shared the Nobel Prize for Physics in 1952 for their work. In the late 1940s and early 1950s the “chemical shift” was discovered, which causes the frequencies at which nuclei resonate to depend on their chemical environment.[7] Thereafter, NMR rapidly grew as a tool for characterization and structure elucidation (particularly for organic molecules).

However, for NMR to realize its full potential, issues of sensitivity and spectral resolution had to be addressed. In the 1960s, signal-to-noise ratio (SNR) (Section 2.6.2) was greatly improved with the introduction of the Fourier transform (FT) method (Section 2.5), which interconverts the time domain and frequency domain, and of signal averaging (Section 2.6.2).[8, 9] A further gain in more recent times has been the development of cryogenically cooled probes (Section 3.4.3.5.1), which increase SNR three to fourfold. In the 1970s, resolution began to improve with the development of superconducting magnets, starting with a factor of two improvement.[10]

The largest advance in signal resolution began in 1975 with the first published 2D NMR experiment by R. Ernst, which was furthered and documented in detail by Aue *et al*.[11] The technique introduced the acquisition of data with two independent time dimensions to which a double Fourier transformation was applied. Such dimensionality allowed signals to be identified in two dimensions, allowing correlations to be separated. The classic example is COSY (**CO**rrelated **S**pectroscop**Y**), which correlates the chemical shifts of scalar coupled spins, a very useful tool for structure elucidation and today one of the most widely used multi-dimensional techniques. The discovery of 2D NMR was a pivotal moment in the development and application of NMR, on which many experiments are now based.

As an analytical tool, NMR remains largely a qualitative technique and it has become arguably the most powerful technique available to the synthetic chemist.[12] NMR for quantitative purposes, though not as familiar as the former, should not be disregarded. It covers a wide range of uses, e.g. content determination (assay), characterization and determination of low-level impurities, degradation and decomposition of drugs, residual solvent analysis etc., and is used in many industries such as pharmaceutical, food and agriculture.[13-15]

For quantitative analysis, it is important to have good resolution with well-separated signals without signal distortion. This allows for precise accurate signal integration, and prevents impurity signals from being obscured by signal overlap. For high precision, signal-to-noise-ratio (SNR) is important.[13] This is exemplified in the two sets of results of Chapter 3, Table 3.3 (Section 3.4.2) and Tables 3.5 and 3.6 (Section 3.4.3), where the percentage relative standard deviations (%RSDs) of the latter are significantly poorer due to lower SNR. Another important consideration is the choice of instrumental set up and processing parameters such as relaxation delay (Section 2.4), zero filling (Section 2.6.1) and application of weighting functions to increase signal-to-noise-ratio (SNR) (Sections 2.6.2 and 2.6.3).[13]

^{1}H NMR (the most commonly observed nucleus) is not the obvious tool of choice for quantitative analysis, since, despite extremely useful and effective multidimensional experiments (1D, 2D, 3D etc.), which enhance signal separation, there is an underlying problem of poor resolution. This is particularly apparent for molecules of increasing complexity, e.g. proteins, where higher numbers of hydrogen atoms give rise to many resonances. The narrow ^{1}H chemical shift range (0-10 ppm) means signal overlap is inevitably prevalent, obscuring low-level impurities.

This thesis sets out to circumvent the poor resolution of overcrowded ^{1}H spectra by using the alternative tool of ^{19}F NMR. For low-level impurity analysis of many pharmaceutical drugs, this is quite a feasible option, since a quarter of the drugs on the market contain fluorine. As presented in Chapters 3 and 4, fluorine offers extremely high resolution for pharmaceutical applications, with comparable sensitivity to ^{1}H NMR. However, using ^{19}F NMR does not come without problems (Chapter 3), since the wide chemical shift ranges often encountered (± 300 ppm) mean that the signals are susceptible to pulse imperfections such as B_1 inhomogeneity and resonance-offset effects.

It is shown here that some problems with pulse imperfections can be overcome using swept-frequency chirp pulses.[16-25] Two new pulse sequences are introduced, CHORUS[26] (**CH**irped, **OR**dered pulses for **U**ltra-broadband **S**pectroscopy) (Chapter 3) and CHORUS Oneshot (Chapter 4). CHORUS achieves excellent results for quantitative ^{19}F NMR, as demonstrated using two measures of performance, repeatability and robustness with respect to offset (Section 3.4.2), where accuracies better than 0.1% over the entire chemical shift range are achieved, an order of magnitude better than the common pharmaceutical criterion for acceptability of ≤ 1%.[15, 27] CHORUS Oneshot is used in its application to ^{19}F DOSY. DOSY (Section 2.10) is a powerful tool for mixture analysis; however, in its application to ^{1}H NMR, signal overlap can render the method ineffective, compromising the accuracy of diffusion coefficients and obscuring impurities. ^{19}F is particularly suitable for DOSY; the exquisite sensitivity of the ^{19}F chemical shift to local environment, means that overlap between signals is far rarer than in ^{1}H NMR. In addition, the high abundance and high gyromagnetic ratio γ give excellent SNR, where high γ allows strong diffusion encoding with relatively short field gradient pulses. CHORUS Oneshot is developed from the parent sequence Oneshot[28] in two stages, diffusion encoding and diffusion decoding (Section 4.2.2). It delivers uniform excitation over more than 250 kHz, well beyond the width of most ^{19}F spectra, in comparison to conventional Oneshot (< 10 kHz).

For low-level impurity analysis of a representative drug rosuvastatin, it was necessary to find a suitable reference material for use in ^{19}F NMR (Chapter 5). Of the three materials investigated, sulfur hexafluoride (SF_6) was found to be the most suitable. The bandshape of the fluorine signal and its satellites is without complex splitting patterns, and is very suitable for accurate reference deconvolution,[29-31] an important method to remove low-level lineshape disturbances, beneath which low-level impurity signals (~ 0.1%) may be hidden. The solubility of SF_6 was investigated in five deuterated solvents of increasing polarity, and it was found to be sufficiently soluble (2.4 mM at 298 K) in DMSO-d_6, the solvent of choice for analysis of rosuvastatin.

In Chapter 6, the use of the CHORUS sequences for low-level impurity investigation is demonstrated and two impurity signals are detected in the 470 MHz ^{1}H decoupled ^{19}F spectra of a sample of rosuvastatin. These are presumably degradation products of the drug, as they were not seen in a fresh sample (Section 6.2.2). To reveal low-level impurities, a triple resonance experiment should be performed to decouple ^{19}F{^{13}C} and ^{19}F{^{1}H} couplings simultaneously. This was not possible using the Bruker AVIII spectrometer, with a 5 mm BBO probe and QNP switch, since ^{19}F and ^{13}C share the same channel (see Section 6.2.3). As an alternative approach, a Varian VNMRS 500 MHz spectrometer was used with a triple resonance HCN triple axis gradient 5 mm probe; however, this presented a technical problem of a different kind. The probe used in the Varian system has a single high frequency channel; therefore, when the probe is tuned to ^{19}F, the spectrometer cannot produce sufficient RF amplitude for full broadband ^{1}H decoupling. By manipulation of the control system of the Varian software, it was possible to overcome the hardware limitations to allow simultaneous ^{1}H irradiation and ^{19}F acquisition (Section 6.2.3.1). This is made possible by time-sharing of the high frequency channel between the two nuclei; time-sharing was first applied to homonuclear decoupling in 1972 by Jesson and Meakin.[32]

With ^{19}F{^{1}H} decoupling being made possible, simultaneous ^{1}H and ^{13}C decoupling of ^{19}F was performed using a continuous sine modulated waveform and adiabatic pulse

WURST40[33] waveform respectively (Section 6.2.3.1.1). The doubly decoupled ^{19}F spectrum of rosuvasatin, using degraded and fresh samples, reveals three impurity signals in the degraded sample; in addition, low-level modulation artefacts are detected, which are shown to be related due to the ^{1}H and ^{13}C decoupler modulation frequencies (dmfs).

Performing a triple resonance experiment as above is tricky. Ideally, a triple resonance probe, built to allow simultaneous irradiation of ^{1}H and ^{13}C while tuned to ^{19}F, should be used, which would allow a more efficient experiment to be performed; this, combined with reference deconvolution (using SF_6 as a reference material) should provide a powerful tool for low-level impurity analysis.

Chapter 2

The Theory of NMR

2. The Theory of NMR

2.1. Nuclear Spin and Magnetization

Nuclei with the intrinsic property of nuclear spin have a quantized angular momentum $\boldsymbol{P}$ with an associated magnetic moment $\boldsymbol{\mu}$. The total $\boldsymbol{P}$ is the combined effect from the proton and neutron contributions, where the proportions of each determine the nuclear quantum spin number, I.[34, 35] If the number of protons and neutrons are both even, e.g. ^{12}C and ^{16}O, then $I = 0$ and the sample is NMR inactive and has no magnetic moment. If the number of protons and neutrons are both odd, e.g. ^{2}H and ^{14}N, then I is a positive integer (1, 2, 3, etc.); for mixed even and odd numbers of nucleons, I is a half integer (1/2, 3/2, 5/2, etc.).

The magnitude of the quantized angular momentum is given by:

$$P = \sqrt{I\,(I + 1)}\;\hbar \qquad 2.1$$

where $\hbar$ is the reduced Planck constant $(h\,/\,2\pi)$ and the magnetic moment is:

$$\boldsymbol{\mu} = \gamma\,\boldsymbol{P} \qquad 2.2$$

where $\boldsymbol{P}$ and $\boldsymbol{\mu}$ are vector quantities with direction, and γ is the gyromagnetic ratio, a proportionality constant. Detection sensitivity is dependent on γ; a large absolute value of γ is more detectable than a smaller value.[34] The z-component of the angular momentum $\boldsymbol{P_z}$ and of the magnetic moment $\boldsymbol{\mu_z}$, when placed in a magnetic field $\boldsymbol{B_0}$, are given by Equations 2.3 and 2.4 respectively:

$$P_z = m\,\hbar \qquad 2.3$$

$$\mu_z = m\,\gamma\,\hbar \qquad 2.4$$

where m is the magnetic quantum number, that can take the values $-I$ to $+I$ in steps of 1. The energy of interaction between the magnetic moment $\boldsymbol{\mu_z}$ interacting with $\boldsymbol{B_0}$ is given by:[35]

$$E = -\boldsymbol{\mu_z}\boldsymbol{B_0} \qquad 2.5$$

For a nucleus with quantum spin number I, there are $(2I+1)$ spin states, where in the absence of an applied magnetic field the spin states are degenerate. If a magnetic field is applied, then the spin states split, which is known as Zeeman splitting.[1] Substituting for $\boldsymbol{\mu_z}$ in to Equation 2.5, gives the nuclear Zeeman energy levels:

$$E = -m\gamma\hbar \mathrm{B}_0 \qquad 2.6$$

For a proton of spin $I = 1/2$, the energy states are split into two, of slightly different energies, commonly referred to as α (+1/2) and β (−1/2), when $m = \pm 1/2$. The difference in energy between the two states is directly proportional to γ for the nucleus, and to the strength of the applied field $\boldsymbol{B_0}$:

$$\Delta E = \gamma\hbar B_0 \qquad 2.7$$

Equation 2.6 shows that the energy of interaction of the nuclear spin, with an applied magnetic field, is dependent on the magnetic quantum number m. The energy is also dependent on the angle θ, where for a positive value of the gyromagnetic ratio γ, the lower energy is for the α-state (spin up, low θ), and the higher energy is for the β-state (spin down, high θ) (Figure 2.1).[36]

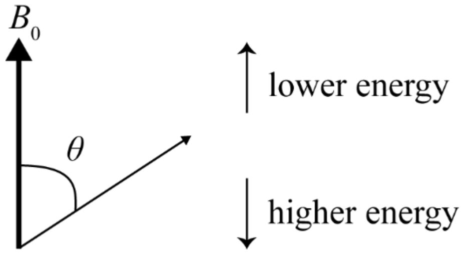

Figure 2.1: The energy of interaction between the magnetic moment, represented by the small arrow, and the applied magnetic field $\boldsymbol{B}_0$, is lowest for low values of θ and highest for high values of θ, where the lowest energy arrangement is when $\theta = 0$.[36]

In a sample, in the absence of an applied field, the orientation of the nuclear magnetic moments (magnetic dipoles) is random, since all orientations have the same energy. When subjected to an applied magnetic field $\boldsymbol{B}_0$, the magnetic dipoles of the nuclei tend to align parallel with $\boldsymbol{B}_0$, which is the lower energy arrangement (Figure 2.1), but this alignment is disrupted by random thermal motion of the molecules, the energy of which is much greater than the energy of interaction of the nuclear spin with $\boldsymbol{B}_0$. The disruption is not complete, and there is an overall net magnetic dipole alignment, comparable to one spin in 10^5, in the direction of $\boldsymbol{B}_0$.[36] To achieve net alignment for the bulk magnetization vector ($\boldsymbol{M}$) takes a finite time; the steady value at thermal equilibrium ($\boldsymbol{M}_0$) is reached by relaxation (see Section 2.4). The net difference in population at equilibrium between the α and β states is given by the Boltzmann distribution:

$$\frac{N_\beta}{N_\alpha} = e^{-\frac{\Delta E}{k_B T}} \qquad 2.8$$

where N_α is the net population of the lower energy state, N_β is the net population of the higher energy state, k_B is the Boltzmann constant, ΔE is given by Equation 2.8 and T is the absolute temperature in Kelvin.[34]

Applying a radiofrequency (RF) pulse (B_1) perpendicular to $\boldsymbol{B_0}$ perturbs the bulk magnetization away from its equilibrium position such that it rotates towards the transverse plane through an angle θ, and then sweeps out a cone with a constant angle β to the *z*-axis, the magnitude of which is dependent on the duration and amplitude of B_1. The frequency of the precessing magnetization is referred to as the Larmor frequency v_o (Hz) and is defined by:

$$v_0 = -\frac{\gamma B_0}{2\pi} \qquad 2.9$$

(or alternatively by the angular velocity $\omega_o = -\gamma B_0$ in rad s^{-1}).

For a spin-half nucleus such as a proton, the Larmor frequency is equal to the frequency of the allowed transition between the two energy levels α and β, and by convention, for a positive gyromagnetic ratio γ, e.g. for nuclei such as ^{1}H and ^{13}C, the Larmor frequency v_o is negative.

2.1.1. Detection of Precessing Magnetization

The Larmor frequency is detected by a coil of wire or metal foil mounted in the probe, which is inserted into the bore of the magnet, where the coil is aligned perpendicular to $\boldsymbol{B_0}$. As the transverse component of $\boldsymbol{M}$ cuts across the detector (or receiver) coil in the probe it induces an oscillating electrical current; the same coil is used to transmit the RF power as to detect the signal. The current is amplified, and to reduce the frequency of the signal from MHz to kHz, its frequency is subtracted from a receiver reference signal, with a value at the middle of the spectrum, using a radio frequency mixer.[37] It is then digitized as a free induction decay (FID), which decays away exponentially. Fourier Transformation (FT) of the FID, yields a spectrum of signals at the Larmor frequencies (v_0) of the spins.

2.1.2. Frames of Reference

A frame of reference, using a co-ordinate system with Cartesian axes (x, y, z), is used in NMR spectroscopy to describe the precession of magnetization $\boldsymbol{M}$ with angular velocity (ω) fixed about the z-axis, which is expressed in terms of vectors M_x, M_y and M_z. An RF pulse (B_1) applied, most commonly along the x-axis perpendicular to $\boldsymbol{B_0}$, defines the frame. However, B_1 is an oscillating field consisting of two counter-rotating components B_1^+ and B_1^- of the same magnitude; by convention, the component B_1^- is used.

2.1.2.1. Laboratory Frame of Reference

In the stationary "laboratory frame", $\boldsymbol{M}$ is rotating simultaneously about two axes, i.e. the transverse x-y plane is rotating about the z-axis. The behaviour of $\boldsymbol{M}$ over time, as it evolves, without the consideration of relaxation (Section 2.4), is described classically by the Bloch equations, where for each vector component (M_x, M_y and M_z) the Bloch equations are:

$$\frac{\mathrm{d}M_\mathrm{x}}{\mathrm{d}t} = \gamma\left(M_\mathrm{y}\,B_\mathrm{z} - M_\mathrm{z}\,B_\mathrm{y}\right) \tag{2.10}$$

$$\frac{\mathrm{d}M_\mathrm{y}}{\mathrm{d}t} = \gamma\,(M_\mathrm{z}\,B_\mathrm{x} - M_\mathrm{x}\,B_\mathrm{z}) \tag{2.11}$$

$$\frac{\mathrm{d}M_\mathrm{z}}{\mathrm{d}t} = \gamma\left(M_\mathrm{x}B_\mathrm{y} - M_\mathrm{y}\,B_\mathrm{x}\right) \tag{2.12}$$

Two axes of rotation are difficult to interpret; therefore, as an alternative, the "rotating frame" is introduced.

2.1.2.2. Rotating Frame of Reference

In this frame of reference, the transverse *x*-*y* plane is rotating about the *z*-axis at the same frequency and the same direction as the Larmor frequency v_o of the spins. Under these conditions, the magnetization is stationary; it no longer precesses in the transverse plane and it is referred to as being “on-resonance”. Equation 2.13 defines the offset (Ω) in terms of angular velocity (ω) in rad s^{-1} rotating about the *z*-axis:

$$\Omega = \omega_0 - \omega_{\text{frame}} \tag{2.13}$$

where ω_{frame} is the rate of rotation of the frame, ω_0 is the Larmor frequency of the spins and on-resonance $\omega_0 = \omega_{\text{frame}}$.[36]

Substituting for offset Ω in Equation 2.9, gives an apparent or reduced magnetic field ΔB**,** as shown by Equation 2.14:

$$\Delta B = -\frac{\Omega}{\gamma} \tag{2.14}$$

The combined effects of the reduced magnetic field ΔB and the RF field B_1 add together to give an effective magnetic field B_{eff} around which the magnetization precesses (Figure 2.2).

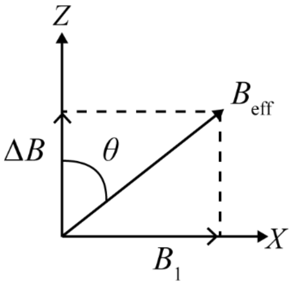

Figure 2.2: The effective field B_{eff} experienced by the spins is the vector sum of the reduced field ΔB and the RF field B_1, where angle θ is the tilt (flip) angle.

The size of the effective field B_{eff} is given by:

$$B_{\mathrm{eff}} = \sqrt{{B_1}^2 + (\Delta B)^2} \qquad 2.15$$

B_1 is a weak RF field in comparison to the field strength of a superconducting magnet such as $\boldsymbol{B_0}$; however, as shown in Equation 2.15, alongside the reduced magnetic field ΔB, as depicted in the rotating frame of reference, it has a strong influence.

The presence of a second, off-resonance, RF field B_2 can cause an apparent shift in Larmor frequency (the Bloch-Siegert shift) that is proportional to $(B_2/\Delta B)^2$. This is because the magnetization precesses about B_{eff}, which is very slightly stronger than ΔB (see Section 6.2.3.1).[38]

2.2. Chemical Shift

The rate of precession (v) of a nucleus is dependent on the applied magnetic field $\boldsymbol{B_0}$ and on the gyromagnetic ratio (γ) of the nucleus (Section 2.1); however, within a molecule not all nuclei resonate at the same frequency, which gives rise to different chemical shifts. This is explained, since for nuclei within a molecule, there are differences in electronic environments due to electronic factors such as electronegativity of atoms withdrawing electrons through chemical bonds to different extents. Therefore, due to differences in local electronic distribution within the molecule, variations in $\boldsymbol{B_0}$ are experienced by the nuclei, which is dependent on their position, i.e. $\boldsymbol{B_0}$ induces motion in the surrounding electrons, generating small magnetic fields, which interfere in a positive or negative sense; this effect is called nuclear shielding.[39]

Since the resonant frequency v of a nucleus is directly proportional to the applied magnetic field $\boldsymbol{B_0}$, then spectra from different spectrometers cannot be directly compared. This dependency is removed by adding a reference material to the sample;

the difference between the resonant frequency ν of a nucleus and the frequency of the reference nucleus ν_{ref} is measured ($\nu - \nu_{\mathrm{ref}}$) and divided by ν_{ref}. The chemical shift δ is scaled by a factor of 10^6 and is in units of parts per million (ppm) as defined in Equation 2.16:

$$\delta = 10^6 \times \frac{\nu - \nu_{\mathrm{ref}}}{\nu_{\mathrm{ref}}} \qquad \text{(ppm)} \tag{2.16}$$

A typical reference material for ^{1}H and ^{13}C is tetramethylsilane (TMS). For both ^{1}H and ^{13}C, it shows strong nuclear shielding; therefore, TMS can be referenced at zero chemical shift ($\delta = 0$), which is at the lower end of the frequency scale, and which is conveniently ‘upfield’ of most other, less shielded, nuclei. For proton NMR, TMS is favourable since it gives a strong ^{1}H resonance from 12 identical protons, it is chemically inert, and it is soluble in most organic solvents.[39]

2.3. Spin-Spin Coupling

Spin-spin couplings can be divided into two categories: direct and indirect dipole-dipole coupling. Direct coupling is the result of magnetic field interaction between spins through space, and can be intra- or intermolecular; this interaction is disrupted and averaged to zero in isotropic liquids, due to the rapid tumbling of molecules.[40]

Indirect (scalar or *J*-) coupling is the result of the interaction between nuclei transmitted through the electrons of chemical bonds. This interaction is not affected by the rapid tumbling of molecules and the effects are observable in the spectrum as splitting patterns of the signals.

For a spin-half nucleus such as ^{1}H, when placed into a magnetic field, the energy levels are split according to the magnetic quantum number m (Section 2.1). For two interacting spin-half nuclei, e.g. A and X, the energy states (α and β) of A with X, can interfere in a positive or negative sense with the two energy states of X (and vice versa); thus the local electronic distributions around A and X are altered, which in turn affects the applied field experienced by the nuclei (see Section 2.2). The effects are to move the resonant frequency of the A and X to lower or higher frequencies resulting in the observed splitting pattern of a doublet.

Magnetically equivalent nuclei have identical magnetic environments, since not only do they have the same chemical shifts, but identical couplings, and even though they may couple, there is no splitting. For weak couplings, the coupling constant, J, which is the magnitude of separation of signals in a multiplet structure, is much smaller than the difference in chemical shifts ($\Delta\nu >> J$); for strong couplings, the frequency separation is similar in magnitude to J.

2.4. Relaxation

As described in Section 2.1, the magnetization vector $\boldsymbol{M}$ in a magnetic field $\boldsymbol{B_0}$ can be perturbed away from the equilibrium state by application of an RF pulse, where the orientation of $\boldsymbol{M}$ can be described by three vector components M_x, M_y and M_z. By the process of relaxation, M_z returns to thermal equilibrium and M_x and M_y approach zero. To describe the process of relaxation, Felix Bloch in 1946,[5] introduced two time constants, T_1 and T_2, into Equations 2.10, 2.11 and 2.12 (Section 2.1.2.1), to account for longitudinal (spin-lattice) relaxation and transverse (spin-spin) relaxation respectively, where Bloch assumed the exponential decay rates to be first order (Equations 2.17, 2.18 and 2.19).

$$\frac{\mathrm{d}M_\mathrm{x}}{\mathrm{d}t} = \Omega\, M_\mathrm{y} - \frac{M_\mathrm{x}}{T_2} \tag{2.17}$$

$$\frac{\mathrm{d}M_\mathrm{y}}{\mathrm{d}t} = -\ \Omega\, M_\mathrm{x} + \gamma\, B_1\, M_\mathrm{z} - \frac{M_\mathrm{y}}{T_2} \tag{2.18}$$

$$\frac{\mathrm{d}M_\mathrm{z}}{\mathrm{d}t} = -\,\gamma\, B_1 M_\mathrm{y} + \frac{M_\mathrm{z}^0 - M_\mathrm{z}}{T_1} \tag{2.19}$$

To simplify the mathematical representation of the Bloch Equations (Section 2.1.2.1), the offset of Larmor frequency from resonance has been introduced into Equations 2.17, 2.18 and 2.19, where $\Omega = \gamma\, B_0 - \omega$; therefore, the terms including Ω, correspond to the precession of magnetization around the main magnetic field B_0. The terms including B_1 represent evolution of the magnetization due to the RF field applied along the x-axis, rotating magnetization from the z-axis towards $-\,y$.

2.4.1. Local Magnetic Fields

In a sample of spins, the associated individual magnetic moments generate “local” magnetic fields. Due to molecular motions, such as rotation and translation, the magnitude and orientation of the local fields fluctuate randomly from spin to spin, where the field of a single spin interacts with surrounding spins. The random nature of the interactions has a net effect of driving the z-component of the magnetization M_z to M_z^0. This is referred to as longitudinal relaxation and is a non-secular contribution, affecting the net energy of the spins, and the balance between α and β states in the wave functions of the spins.[41] Transverse relaxation, which is also affected by molecular tumbling, has an additional secular contribution, i.e. the random contribution of the z-component of the local fields causes spins to precess about the z-axis at slightly different rates. Over time the spins become out of step with each other, losing their phase coherence, bringing the transverse components M_x and M_y to zero.[41] For M_z to reach M_z^0, it follows that M_y must be zero, it is almost always true that $T_1 \geq T_2$.[42]

2.4.2. Relaxation Mechanisms

Relaxation due to local magnetic fields can arise through various mechanisms, e.g. dipolar (dipole-dipole) interactions, chemical shift anisotropy (CSA), paramagnetic interactions and quadrupolar interactions. The main contributions to longitudinal relaxation for spin half nuclei, are dipolar and CSA. For dipolar relaxation, the strength of the dipole-dipole interaction is dependent on the gyromagnetic ratio of the spin, the inverse cube of the distance between the spins, and the orientation of the vector joining the two spins relative to the *z*-axis.[41] In CSA relaxation, molecular tumbling causes the shielding of the nucleus by local electrons to vary rapidly. The average effect is to give the isotopic chemical shift (Section 2.2). The effect of the field caused by anisotropic shielding is to generate CSA relaxation.[41]

2.4.2.1. Quadrupolar Relaxation

Nuclei with $I \geq 1$ possess an electric quadrupole moment (Q) as well as a nuclear dipole magnetic moment. For these nuclei, there is an interaction between the quadrupole moment and the electric field gradient. The electric field gradients exactly cancel for highly symmetrical molecules so there is no net quadrupolar interaction. In the absence of such symmetry, the quadrupolar interactions can be large, and depend on the orientation of the molecule in the magnetic field $\boldsymbol{B_0}$. Random molecular motions (in liquids) cause fluctuations in the interactions, which are a source of relaxation. This form of relaxation can be quite effective, resulting in line-broadening of NMR signals to the extent that multiplet structures can be hidden.[43]

2.4.3. Longitudinal Relaxation

For longitudinal relaxation, Equation 2.19 can be simplified to:

$$\frac{\mathrm{d}M_z(t)}{\mathrm{d}t} = -R_1\,[M_z(t) - M_z^0] \qquad 2.20$$

where R_1 is the rate constant for decay, which can be defined in terms of the time constant for longitudinal relaxation T_1, where $T_1 = 1 / R_1$. If Equation 2.20 is integrated, then:

$$M_z(t) = \left(M_z(0) - M_z^0\right)e^{-R_1 t} + M_z^0 \qquad 2.21$$

To measure longitudinal relaxation, an inversion-recovery experiment can be performed. A 180° pulse is used to invert the magnetization along the $-z$-axis; it is then allowed to relax back for a time τ, after which the magnetization is rotated into the transverse plane by a 90° read pulse and detected. This is repeated for different values of τ, to give a series of signal amplitudes as a function of τ, from which the T_1 can be estimated using Equation 2.21. Since the rate of change of magnetization is exponential, it takes an infinite amount of time for complete relaxation. To gain 99 % recovery, a delay of five times T_1 is sufficient.[41]

2.4.4. Transverse Relaxation

For transverse relaxation, Equations 2.17 and 2.18, can be written in terms of the differential of M_x or M_y:

$$\frac{\mathrm{d}M_x(t)}{\mathrm{d}t} = -R_2\,M_x(t) \qquad \text{or} \qquad \frac{\mathrm{d}M_y(t)}{\mathrm{d}t} = -R_2\,M_y(t) \qquad 2.22$$

where $R_2 = 1/T_2$ is the rate constant for transverse relaxation. If the offset is not zero then there is precession of the *x*- and *y*-components in the transverse plane. The effect of this can be eliminated by applying Equation 2.23:

$$M_{\mathrm{xy}} = \sqrt{M_{\mathrm{x}}^2 + M_{\mathrm{y}}^2} \qquad 2.23$$

M_{xy} is now independent of phase and only dependent on the transverse relaxation T_2, therefore:

$$\frac{\mathrm{d}M_{\mathrm{xy}}(t)}{\mathrm{d}t} = -R_2\, M_{\mathrm{xy}}(t) \qquad 2.24$$

If Equation 2.24 is integrated, and the exponentials taken of both sides, then:

$$M_{\mathrm{xy}}(t) = M_{\mathrm{xy}}(0)\, e^{-R_2 t} \qquad 2.25$$

Using a spin echo[44] or a Carr-Purcell-Meiboom-Gill (CPMG) experiment,[45] a series of signal amplitudes as a function of τ, can be recorded, from which T_2 can be estimated using Equation 2.25.

2.4.4.1. Time Constant T_2^*

Due to $\boldsymbol{B_0}$ field inhomogeneities, when an RF pulse is applied, the individual spins precess with slightly different Larmor frequencies; thus, there is additional loss of phase coherence during transverse relaxation. The time constant T_2^* seeks to combine the signal decay due to field inhomogeneities T_{inhom} and the relaxation from random motions of the local fields T_2 (Equation 2.26).

$$\frac{1}{T_2^*} = \frac{1}{T_2} + \frac{1}{T_{\text{inhom}}} \qquad 2.26$$

where it is assumed that field inhomogeneities cause a Lorentzian distribution of signal strength. The effects of T_{inhom} can be reversed using a spin echo experiment, unlike the loss of phase coherence due to transverse relaxation from random molecular motions (the frequencies at which these spins evolve are not constant and are not reversible).

2.5. The Fourier Transform

In NMR spectroscopy, the data are acquired as an FID, which is a function of time. For ease of interpretation, a Fourier Transformation (FT) is applied to produce a spectrum as a function of frequency.

Applying a 90° RF pulse along the y-axis in the transverse plane perturbs the equilibrium magnetization M_0 such that it rotates about y onto the x-axis. The x- and y- components of the magnetization, $M_x = M_0 \cos(\Omega\, t)$ and $M_y = M_0 \sin(\Omega\, t)$, are detected to give separate signals of intensity S_x and S_y; signal intensity is proportional to the magnetization, therefore the x- and y- components, M_x and M_y, can be written in terms of signal intensity:[46]

$$S_x(t) = S_0 \cos \Omega\, (t)\, e^{-t/T_2} \qquad 2.27$$

$$S_y(t) = S_0 \sin \Omega\, (t)\, e^{-t/T_2} \qquad 2.28$$

where exponential decay terms are introduced and where S_0 is a proportionality constant. If the x- and y-components are considered as a complex signal, then:

$$S(t) = S_x + \mathrm{i}\, S_y \qquad 2.29$$

Using Euler's relationship $\left(\mathrm{e}^{\mathrm{i}x} = \cos x + \mathrm{i}\sin x\right)$, Equation 2.29 can be represented as a complex time domain signal as a function of S(t) of the FID:

$$S(t) = S_0\,\mathrm{e}^{\,\mathrm{i}\Omega t} e^{-t/T_2} \qquad 2.30$$

Each resonance in the spectrum i has its own intensity S_i, frequency Ω_i and rate of decay $1/T_2$; the complex time domain signal is the sum of each resonance in the spectrum and represents the FID, $S_{\mathrm{FID}}(t)$.

Fourier transformation of the FID can be understood as multiplying it by a series of cosine waves of different frequencies. If multiplied by a cosine wave, which has the same frequency as a cosine component of the FID, then the product of the waveforms is always positive and the integral is proportional to the amplitude S, of the FID. If the FID is multiplied by a cosine wave which is not of the same frequency, then the product waveform oscillates about zero with positive and negative values and the integral is zero. The mathematical expression for this procedure is shown in Equation 2.31:[46]

$$\mathrm{S}(f) = \int_0^{+\infty} S_{\mathrm{FID}}\,(t)\;\cos\;(\,2\,\pi f\;t)\;\mathrm{d}t \qquad 2.31$$

where S(f) is the intensity in the spectrum at frequency f and $S_{\mathrm{FID}}(t)$ is the amplitude of the FID at time t; the integration is repeated for a range of frequencies.

2.5.1. Linewidths and Lineshapes in NMR

Substituting for the $S_{\mathrm{FID}}(t)$, Equation 2.30 into 2.31, and integrating, the expression transforms the complex time domain signal into the complex frequency domain signal $S(\omega)$, where the identity $\cos\,(2\omega t) = \left(e^{\mathrm{i}\omega t} + e^{-\mathrm{i}\omega t}\right)/2$ is used and where ω is in rad s^{-1} (Equation 2.32).

$$\mathrm{S}(\omega) = S_0 \int_0^{+\infty} e^{\,\mathrm{i}(\Omega-\omega)t - R_2 t} \times \left(\mathrm{e}^{\,\mathrm{i}\omega t} + e^{-\mathrm{i}\omega t}\right)/2 \ \mathrm{d}t \qquad 2.32$$

where $\mathrm{S}(t) = S_{\mathrm{FID}}\,(t)$ and $R_2 = 1/T_2$. The solution of Equation 2.32 gives two terms resulting in two lineshapes of signal in the spectrum, the desired real absorption Lorentzian mode $A(\omega)$, and the imaginary dispersion Lorentzian mode $D(\omega)$, normally not displayed, since it is broader with both positive and negative signal intensities (Equations 2.33 and 2.34):[39, 46]

$$A\,(\Delta\omega) = \frac{R_2}{R_2^2 + (\omega - \Omega)^2} \qquad 2.33$$

$$D\,(\Delta\omega) = \mathrm{i}\frac{-\,(\omega - \Omega)}{R_2^2 + (\omega - \Omega)^2} \qquad 2.34$$

where A is the amplitude of the absorption mode signal, $\Delta\omega = \omega - \Omega$ is the frequency offset centred at Ω. When $\omega = \Omega$, then the peak height of the Lorentzian lineshape is given by $1/\,\mathrm{R}$ and the half height linewidth by $R_2\,/\,\pi$ Hz (or $2\,R_2$ rad s^{-1}).[46] The greater the rate constant R_2 and the faster the relaxation, the broader the lines become.

2.6. Data Processing

Before FT, the analogue FID is stored in digital form in the computer. The waveform is sampled at regular intervals by an analogue-to-digital converter (ADC). As described in Section 2.1, the frequencies of NMR signals are too high for an ADC, so the signals are mixed down to a lower frequency, i.e. from MHz to kHz.[37] To represent the FID accurately the sampling rate must be at least two data points per cycle, as defined by the Nyquist Theorem.[37]

The dwell time (DW) is the time interval between data points. For a defined spectral width (SW), the range of frequencies within the window is defined by the DW between data points; the lower DW the higher the frequency that can be faithfully measured (Equation 2.35):[47]

$$\mathrm{DW} = \frac{1}{2\,\mathrm{SW}} \tag{2.35}$$

Alternatively, for simultaneous sampling with the transmitter frequency at the centre of the spectrum, the frequency range becomes $\pm$ SW/2 and the sampling rate becomes equal to SW, such that $\mathrm{DW} = 1/\mathrm{SW}$; thus, for a signal to be sufficiently digitized, it must have a sampling rate less than or equal to SW.

2.6.1. Zero Filling

Consider (np) as the total number of data points in the FID; since the complex spectrum has two parts, real and imaginary, the displayed Lorentzian signal contains only half the number of data points (np/2) and hence only uses half of the information in the FID. Zero filling is manipulation of the data by adding more data points with zero intensity to the end of the FID, without adding noise. One zero filling to the FID adds one set of zeros $(= \mathrm{np}/2)$, which can improve the spectral resolution, since the displayed Lorentzian signal now has the full set of data points; further to this, zero filling only interpolates.[47]

2.6.2. Sensitivity Enhancement

Sensitivity in NMR is dependent on two main factors: the intrinsic magnetic properties of the nucleus such as the gyromagnetic ratio γ, and the size of the applied magnetic field $\boldsymbol{B_0}$ (Section 2.1). These two factors affect the size of the Larmor frequency ν_0 which is detected by the spectrometer. The relative abundance of the active NMR species also needs to be considered; the combined effect of γ and natural abundance cause poor sensitivity for ^{13}C in contrast to the spectrum of ^{1}H.

Since NMR generally has low sensitivity, then it is important to maximize signal-to-noise ratio (SNR). To improve SNR, time averaging is applied, where the experiment is repeated many times and the resultant free induction decays (FIDs) are added together. For N transients the signal adds up in direct proportion; the noise, however, since it is random, adds up more slowly at the rate of $\sqrt{N}$; thus, SNR ~ $\sqrt{N}$.[48]

A common method to optimize the SNR is multiplication of the time-domain signal with an exponential decay using a mathematical procedure called apodization (Equation 2.36):[46]

$$W_{\mathrm{LB}}(t) = e^{-R_{\mathrm{LB}}\, t} \tag{2.36}$$

where $W_{\mathrm{LB}}(t)$ is an exponential weighting function (referred to as a line broadening term) and R_{LB} is a rate constant which determines the rate of decay of the exponential. The weighting function maintains the early part of the FID, where the signal is strongest, and attenuates the later part where the signal is weakest, thus collecting less noise and increasing SNR. However, R_{LB} has to be chosen carefully, since line broadening decreases peak heights, which opposes the desired effect. Multiplication of Equation 2.36 by the complex time domain signal (Equation 2.30, Section 2.5) gives:[46]

$$W_{\mathrm{LB}}(t) \times S\,(t) = S_0\, \mathrm{e}^{\,\mathrm{i}\Omega t}\, \mathrm{e}^{-[\,R_2 + R_{\mathrm{LB}}]\, t} \tag{2.37}$$

Fourier transformation of Equation 2.37, gives a peak at half height of width $(R_2 + R_{\mathrm{LB}})\,/\,\pi$ Hz (Section 2.5.1); therefore, the peak width $R_2\,/\,\pi$ in the original spectrum has been increased by $R_{\mathrm{LB}}\,/\,\pi$. To optimise the SNR, a matched filter is used, which is when $R_{\mathrm{LB}} = R_2$, such that the line is broadened equal to the linewidth in the original spectrum.[46]

2.6.3. Resolution Enhancement

For resolution enhancement the linewidth is forced to decrease and the signal becomes sharper; here the weighting function increases in time:[46]

$$W_{\mathrm{RE}}(t) = e^{R_{\mathrm{RE}}t} \qquad 2.38$$

where $W_{\mathrm{RE}}(t)$ is a resolution enhancement term and the rate constant is $R_{\mathrm{RE}} > 0$. The continuously rising exponential amplifies the FID as it decays away towards the tail; however, it also amplifies the noise reducing the SNR. To address this problem, a second Gaussian weighting function is applied, which is bell-shaped and symmetrical about its centre:[46]

$$W_{\mathrm{G}}(t) = \mathrm{e}^{-\alpha t^2} \qquad 2.39$$

where α is a parameter that sets the decay rate. The time domain signal (Section 2.5), is multiplied by the rising exponential followed by the falling Gaussian; this is referred to as a Lorentz-to-Gauss transform. Thus, the latter part of the FID is enhanced, while the Gaussian, which initially decays more slowly than the exponential, becomes more rapid, attenuating the noise more effectively towards the end of the FID. The resulting signals are Gaussian in lineshape, more compact at the base in comparison to Lorentzian.

2.6.4. Reference Deconvolution

NMR experiments are subject to instrumental distortions due to instrumental imperfections caused by, e.g. field inhomogeneity in an applied magnetic field $\boldsymbol{B_0}$ or an RF field B_1. The resulting effects on the spectrum can be to introduce phase errors, amplitude irreproducibility, frequency shifts, spinning sidebands or line broadening.[29-31] Reference deconvolution endeavours to correct these effects by using the known lineshape of a reference signal to deduce the correction required.

Reference deconvolution is of particular importance when examining low-level impurities, since impurities may be hidden beneath low-level disturbances caused by the instrumental imperfections.

2.7. NMR and Quantum Mechanics

In Section 2.1.2.1, the Bloch equations were introduced to describe the behaviour of magnetization $\boldsymbol{M}$ over time in terms of the three-vector components M_{x}, M_{y} and M_{z}. However, this classical approach is limited when applied to more complex interactions such as spin-spin couplings. To do this a quantum mechanical approach is required.

2.7.1. The Hamiltonian Operator

To explain the energy of a system, a wavefunction is used from which the Hamiltonian operator $\widehat{H}$ can extract the information. For a nuclear spin I in a magnetic field of magnitude $\boldsymbol{B_0}$, applied along the z-axis, the energy of interaction between the spin and the magnetic field is represented by:

$$\widehat{H}_{\text{one spin}} = -\gamma B_0 \hat{I}_z \qquad 2.40$$

where $\hat{I}_z$ is an angular momentum operator used to describe the z-component of the nuclear spin angular momentum interacting with B_0.[48]

For a spin I there are $2I + 1$ wavefunctions ψ_{m}, referred to as eigenfunctions of $\hat{I}_z$, for which the Equation 2.41 holds:

$$\hat{I}_{\mathrm{z}}\, \psi_m = m\, \hbar\, \psi_m \qquad 2.41$$

where $\hbar = h / 2\pi$ and h is the Planck constant. Substitution of Equation 2.41 into the Hamiltonian (Equation 2.40), gives the energies of the eigenfunctions available to the system, E_m[48] (Equation 2.42).

$$E_m = -m\,\gamma\,\hbar\,B_0 \qquad 2.42$$

$\hat{I}_z$ is characterized by an associated quantum number m, which can take values between $-I$ and $+I$ in integer steps. Therefore, for a spin half nucleus $I = 1/2$ (Section 2.1), the angular operator $\hat{I}_z$ has two energy states (eigenvalues) available, $m = \pm 1/2$, and two associated eigenfunctions ψ_α and ψ_β. For a positive value of the gyromagnetic ratio (γ), the energy of the allowed transition from the lower energy α-state to the higher energy β-state is:

$$\Delta E_{\alpha\rightarrow\beta} = E_\beta - E_\alpha \qquad 2.43$$

Since the energy of a photon of frequency (v) is given by hv, then:

$$v_{\alpha\rightarrow\beta} = \Delta E_{\alpha\rightarrow\beta} / h \qquad 2.44$$

This can be applied to NMR spectroscopy, such that allowed transitions give a signal at the Larmor frequency v_0, as shown by:

$$v_{\alpha\rightarrow\beta} = \frac{\gamma\,B_0}{2\,\pi} \qquad 2.45$$

The Hamiltonian (Equation 2.45), can be written in terms of frequency (Hz):[48]

$$\widehat{H}_{\text{one spin}} = -v_0\,\hat{I}_{\text{z}} \qquad 2.46$$

2.7.2. The Hamiltonian Operator for Two Spins

For a two spin system the Hamiltonian is extended to:

$$\widehat{H}_{\text{two spins, no coupl.}} = -v_{0,1}\,\hat{I}_{1\text{z}} - v_{0,2}\,\hat{I}_{2\text{z}} \qquad 2.47$$

where $v_{0,1}$ is the Larmor frequency of the first spin and $v_{0,2}$ is the Larmor frequency of the second spin with corresponding different operators $\hat{I}_{1\text{z}}$ and $\hat{I}_{2\text{z}}$. If there is scalar coupling between the spins, and the spins are weakly coupled, then a third term is introduced to give:

$$\widehat{H}_{\text{two spins}} = -\nu_{0,1}\,\hat{I}_{1z} - \nu_{0,2}\,\hat{I}_{2z} + J_{12}\,\hat{I}_{1z}\,\hat{I}_{2z} \qquad 2.48$$

where J_{12} is the scalar coupling in Hz between spins one and two.[48]

2.7.2.1. Allowed Transitions

For two coupled spins, the total spin quantum number (M_s) can change by ± 1; however, only one of the spins can change by $\Delta m = \pm 1$, called the ‘active’ spin; the other spin is ‘passive’. The change in the total quantum number (ΔM_s), is found by adding the magnetic quantum number (m) values for each spin, where the allowed transitions ($\Delta M_s = \pm 1$) are called single-quantum transitions.[48]

2.7.2.2. Forbidden Transitions

For a two-spin system, there can be forbidden transitions, which cannot be seen in the spectrum; however, they can be detected indirectly using, e.g. 2D NMR. The forbidden transitions are double-quantum, where $\Delta M = -2$, $(\alpha\,\alpha \leftrightarrow \beta\,\beta)$ and zero-quantum, where $\Delta M = 0$, $(\alpha\,\beta \leftrightarrow \beta\,\alpha)$.[48]

2.8. The Density Operator

In NMR experiments, nuclear magnetization evolves over time; the way in which the wavefunction changes over time is predicted by the Time-Dependent Schrödinger Equation 2.49 (TDSE):[49]

$$\frac{\mathrm{d}\psi(t)}{\mathrm{d}t} = -\,\mathrm{i}\,\widehat{H}\,\psi(t) \qquad 2.49$$

where the wavefunction $\psi\,(t)$ is a function of time. However, to solve the TDSE can be lengthy. This process is simplified by introducing the density operator $\hat{\rho}$. The time evolution of $\hat{\rho}$ is represented by the Liouville-von Neumann Equation 2.50:[49]

$$\frac{\mathrm{d}\hat{\rho}\,(t)}{\mathrm{d}t} = -\,\mathrm{i}\left(\widehat{H}\,\hat{\rho}(t)\,-\,\hat{\rho}(t)\,\widehat{H}\right) \tag{2.50}$$

For a time-independent Hamiltonian the solution of Equation 2.50 is:

$$\hat{\rho}\,(t) = e^{-\,\mathrm{i}\,\widehat{H}\,t}\,\hat{\rho}\,(0)\,e^{\mathrm{i}\,\widehat{H}\,t} \tag{2.51}$$

where $\hat{\rho}(t)$ and $\hat{\rho}(0)$ are the density operator at time t and time zero respectively and where $\widehat{H}$ determines how the spins evolve over time zero to time t.

2.8.1. Product Operator Formalism

Density matrix theory provides an accurate method for analysis of the evolution of the nuclear spin states over time. However, for large spin systems and increasingly complex pulse sequences, analysis becomes more complicated; a more convenient analysis is provided by the product operator formalism.[50] This formalism incorporates the visual representation of the vector model, using geometric rotations in the Cartesian co-ordinate system, while maintaining the accuracy given by the density matrix.

For a single spin half nucleus, there are four product operators, the identity operator $\widehat{E}$, and three Cartesian components of spin angular momentum $\hat{I}_x$, $\hat{I}_y$ and $\hat{I}_z$. For a two spin heteronuclear system I and S, there are sixteen operators (Table 2.1).

	$\hat{\boldsymbol{E}}$	$\hat{\boldsymbol{S}}_x$	$\hat{\boldsymbol{S}}_y$	$\hat{\boldsymbol{S}}_z$
$\hat{\boldsymbol{E}}$	$\hat{E}$	$\hat{S}_x$	$\hat{S}_y$	$\hat{S}_z$
$\hat{\boldsymbol{I}}_x$	$\hat{I}_x$	$2\hat{I}_x\hat{S}_x$	$2\hat{I}_x\hat{S}_y$	$2\hat{I}_x\hat{S}_z$
$\hat{\boldsymbol{I}}_y$	$\hat{I}_y$	$2\hat{I}_y\hat{S}_x$	$2\hat{I}_y\hat{S}_y$	$2\hat{I}_y\hat{S}_z$
$\hat{\boldsymbol{I}}_z$	$\hat{I}_z$	$2\hat{I}_z\hat{S}_x$	$2\hat{I}_z\hat{S}_y$	$2\hat{I}_z\hat{S}_z$

Table 2.1: Product operators of a two spin system, *I* and *S*, showing the sixteen possible combinations, where a factor of two is included for normalization.

The terms $\hat{I}_z$ and $\hat{S}_z$ represent the *z*-magnetization operators.

($\hat{I}_x$, $\hat{I}_y$, $\hat{S}_x$, $\hat{S}_y$) and ($\hat{I}_x\,\hat{S}_z$, $\hat{I}_y\,\hat{S}_z$, $\hat{I}_z\,\hat{S}_x$, $\hat{I}_z\,\hat{S}_y$) represent in-phase and anti-phase magnetization respectively. The two groups of product operators are referred to as single quantum coherences, and they are the only sets that are directly detectable by NMR.

($\hat{I}_x\,\hat{S}_x$, $\hat{I}_x\,\hat{S}_y$, $\hat{I}_y\,\hat{S}_x$, $\hat{I}_y\,\hat{S}_y$) represent double and zero quantum coherences, classed as multiple quantum coherences, which are not directly detectable.

$\hat{I}_z\,\hat{S}_z$ represents anti-phase *z*-magnetization for both spins, referred to as a *J*-ordered state.

As described in Section 2.8, nuclear magnetization evolves over time. The product of formalism allows us to express this evolution economically. During free precession, Equation 2.52 gives the Hamiltonian in the rotating frame of reference.

$$\widehat{H}_{\text{free}} = \Omega\,\hat{I}_{\text{z}} \qquad 2.52$$

where Ω is the offset of the spin from resonance and $\hat{I}_{\text{z}}$ is the *z*-component operator for spin angular momentum. Using Equation 2.52, and substituting for the Hamiltonian and for $\hat{\rho}\,(0)$ in Equation 2.51, allows the evolution of the magnetization to be evaluated:

$$\hat{\rho}\,(t) = e^{-\,\mathrm{i}\,\Omega\,t\,\hat{I}_z}\ \hat{I}_x\, e^{\,\mathrm{i}\,\Omega\,t\,\hat{I}_z} \qquad 2.53$$

where at time zero the density operator $\hat{\rho}\,(0)$ is $\hat{I}_{\text{x}}$, which is obtained from the matrix representations of the product operators $\hat{I}_z$, $\hat{I}_x$ and $\hat{I}_y$.[49] Equation 2.53 can be written in terms of an identity:

$$e^{-\,\mathrm{i}\,\Omega\,t\,\hat{I}_z}\ \hat{I}_x\, e^{\,\mathrm{i}\,\Omega\,t\,\hat{I}_z} \equiv \cos\Omega\,t\,\hat{I}_x + \sin\Omega\,t\,\hat{I}_y \qquad 2.54$$

This methodology can be applied to the rotation of any operator about a defined axis. A preferred notation for Equation 2.54 is:

$$\hat{I}_x \xrightarrow{\Omega\,\tau\,\hat{I}_z} \cos(\Omega\tau)\,\hat{I}_x + \sin(\Omega\tau)\,\hat{I}_y$$

where, for this example, the operator $\hat{I}_{\text{x}}$ is rotated about the *z*-axis by the offset operator $\Omega\,\tau\,\hat{I}_z$; by convention, rotations follow the right-handed axis rule.[36, 49]

For coupled spins and a delay *τ*, the magnetization for each spin evolves under the coupling as well as the offset. This generates anti-phase terms, which interconvert with in-phase terms causing *J*-modulation, and which distort multiplet structures in the NMR spectrum.

The evolution on spin one is shown by:[49]

$$\hat{I}_x \xrightarrow{\Omega\,\tau\,\hat{I}_z} \xrightarrow{2\pi J_{12}\tau\hat{I}_{1z}\hat{I}_{2z}} \cos(\Omega_1\tau)\cos(\Omega_1\pi\,J_{12}\tau)\hat{I}_{1x} + \cos(\Omega_1\tau)\sin(\Omega_1\pi J_{12}\tau)\,2\,\hat{I}_{1y}\hat{I}_{2z}$$
$$+ \sin(\Omega_1\tau)\cos(\Omega_1\pi\,J_{12}\tau)\hat{I}_{1y} - \sin(\Omega_1\tau)\sin(\Omega_1\pi\,J_{12}\tau)\,2\,\hat{I}_{1x}\hat{I}_{2z}$$

where $J_{12}\,\tau$ is the scalar coupling in Hz between spins one and two (see Section 2.7.2, Equation 2.48).

2.9. Coherence Transfer Pathway Selection

As discussed in Section 2.8.1, for a two spin system there are sixteen possible combinations of operators; subsequently, during a sequence of RF pulses, the perturbed magnetization from equilibrium ($\boldsymbol{M_0}$), will generate many different coherences at different stages in the sequence, e.g. single quantum and multiple quantum coherences. It is important in an experiment, particularly in 2D NMR, to select the desired coherence pathway, since unwanted coherences complicate spectra making interpretation difficult. To aid in the process of coherence pathway selection, the concept of coherence order (p) is used. Two methods to achieve such selectivity are phase cycling and pulsed field gradients (PFGs); they can be performed independently or in combination.

2.9.1. Coherence Order

Coherence order (p) is defined in terms of the phase (θ) acquired by an operator (or product operator). When subjected to rotation at an angle θ about the z-axis, the operator will acquire a phase of $-p\,\theta$.[51]

Coherence orders of $p = 0$, $p = \pm 1$ and $p = \pm 2$, define the operators in terms of coherence order, as zero, single and double quantum respectively, where for operators with $p = 0$ are either zero quantum or z-magnetization; for $p = \pm 1$, magnetization is detectable in the transverse plane. By convention, the coherence detected is taken to be that with $p = -1$.

Product operators can be defined by coherence order in terms of $\hat{I}_+$ (raising operator) and $\hat{I}_-$ (lowering operator), which have coherence orders $p = +1$ and $p = -1$ respectively.[51] For a single spin, then for $\hat{I}_x$ and $\hat{I}_y$, the following identities are true:

$$\hat{I}_x \equiv \frac{1}{2}(\hat{I}_+ + \hat{I}_-) \quad \text{and} \quad \hat{I}_y \equiv \frac{1}{2i}(\hat{I}_+ - \hat{I}_-) \qquad 2.55$$

Thus to summarize: a 90° pulse applied to $\hat{I}_z$ will generate only $\hat{I}_x$ or $\hat{I}_y$, which have equal amounts of coherence order $p = +1$ and $p = -1$; in addition, for a 180° pulse, the sign of the coherence order is reversed.

Using these observations, changes in coherence order (Δp) during a series of 90° and 180° pulses, such as the Oneshot pulse sequence,[28] can be demonstrated in a coherence transfer pathway (CTP) diagram (Figure 2.3).

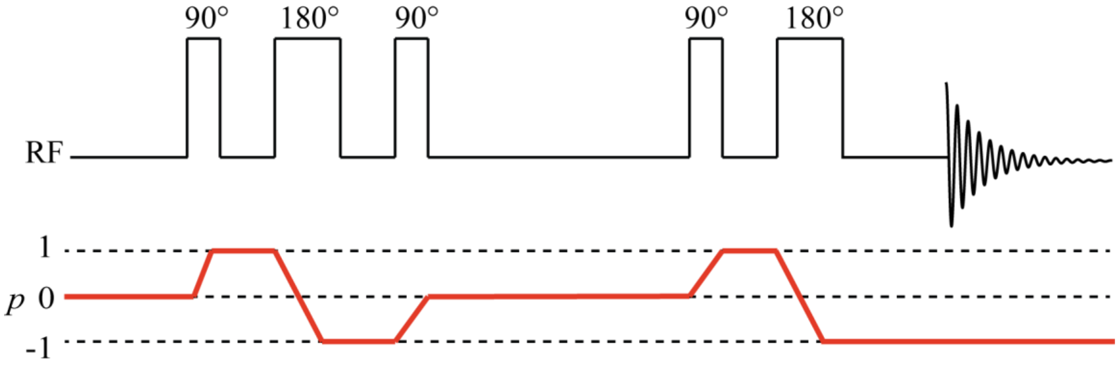

Figure 2.3: Oneshot pulse sequence, with a coherence transfer pathway (CTP) diagram drawn below, without the PFGs. The CTP (red) demonstrates a suitable path, which results in detectable magnetization of coherence order $p = -1$. Progressive changes of coherence order are shown, as each pulse is applied, starting with equilibrium magnetization $p = 0$.

2.9.2. Phase Cycling

Phase cycling is a method whereby a desired coherence pathway can be selected and unwanted pathways suppressed. This is possible since if a pulse of phase φ is applied, and it causes a change in coherence order (Δp), then the coherence, and thus any subsequent detected signal, experiences a phase shift of $\Delta p \times \Delta\varphi$; the change in phase of a coherence carries through from one pulse to the next in a progressive manner.[51] Thus, by altering the phases of pulses, and controlling the phase shifts of the coherences, signals can be forced to add together or cancel out. To achieve a certain outcome, it is necessary to repeat an experiment several times, with different values of $\Delta\varphi$. Once the full phase cycle is completed, the results are combined by co-addition of the FIDs.

An added advantage of this method is that the phase of the receiver can be controlled, thus it can be matched in sympathy to the sum of the phase shifts of the pulses, ensuring the desired pathway is detected.[51]

One of the first phase cycles developed was EXORCYCLE,[52] named as it was used to remove "phantom" and "ghost" signals from a 2DJ spectrum. These signals arise from imperfect refocusing by a 180° pulse, which is a common problem. EXORCYCLE is a four-step sequence in which the phase of the 180° pulse is cycled through the phases [0°, 90°, 180°, 270°] and the phase of the receiver through [0°, 180°, 0°, 180°]; therefore, a 90° phase shift is combined with inversion of the receiver phase, and for an even number of repeats, the unwanted coherences cancel out.[52]

Limitations of phase cycling include increased experiment time, since the full phase cycle has to be completed. In addition, unwanted coherences may not completely cancel out, due to variations in phases and amplitudes, related to field instabilities or changes in temperature between steps in the cycle.

2.9.3. Pulsed Field Gradients (PFGs)

PFGs offer an alternative method for CTP selection. Incorporation of PFGs into a pulse sequence allows the magnetic field $\boldsymbol{B_0}$ to be made intentionally inhomogeneous. The effect of the field inhomogeneity is to cause dephasing of magnetization, which can be refocused for wanted coherences while unwanted coherences can be left dephased, so that the signals are removed from the spectrum.

2.9.3.1. Loss of Phase Coherence

To create a PFG a coil is placed near to the RF coil in the NMR probe, such that a field gradient can be generated by a flowing current; this causes a linear variation in $\boldsymbol{B_0}$ along the direction of the *z*-axis and the magnetic field becomes spatially dependent. The linear variation in $\boldsymbol{B_0}$ causes the spins to precess at different Larmor frequencies about the *z*-axis; therefore, in a similar fashion to transverse relaxation (Section 2.4), the spins rapidly become out of step with each other, losing their phase coherence and decaying away. The dephasing can then be reversed and the coherences refocused by application of a second PFG, of equivalent strength and duration, but of opposite sign, generated by reversing the direction of current.

Using the above principle of dephasing and refocusing, a wanted CTP can be selected, as long as the refocusing condition of Equation 2.56 is met:

$$\frac{G_1\tau_1}{G_2\tau_2} = -\frac{P_2}{P_1} \qquad 2.56$$

where G_1 and G_2 are the magnetic field gradients in T m^{-1}, τ_1 and τ_2 are respective durations of the field gradients, and the desired coherence orders for the selected pathway are given by P_1 and P_2.

A limitation of using PFGs is that the field gradients can generate eddy currents in conducting parts of the probe and magnet; this may result in lineshape and phase distortions of the detected signals in the spectrum.

The variation in $\boldsymbol{B}_0$ is not perfectly linear; thus for measurements of diffusion coefficients, this needs to be corrected for during processing.[53]

2.10. Diffusion-Ordered Spectroscopy (DOSY)

2.10.1. Diffusion

Brownian motion describes the diffusion of molecules in a fluid system, where Albert Einstein developed the quantitative bases for the motion between 1905-1908. He described the motion as directly related to the molecular-kinetic theory of heat, which results in collisions of particles with surrounding molecules, driven by their random translational and rotational movements, where it is assumed that the movements of individual particles are independent of each other.[54] Therefore, it follows that diffusion is correlated to factors such as temperature, shape and size of particles and fluid viscosity, as shown in the Stokes-Einstein Equation 2.57:

$$D = \frac{k_\mathrm{B}\, T}{f_\mathrm{r}} \tag{2.57}$$

where D is the diffusion coefficient, k_B is the Boltzmann constant, T is the absolute temperature, and f_r is the friction factor. For a spherical particle of hydrodynamic radius r_s in a continuum solution, where η is the viscosity of the solution, the friction factor is given by:[55]

$$f_\mathrm{r} = 6\, \pi\, \eta\, r_\mathrm{s} \tag{2.58}$$

2.10.2. DOSY

Diffusion-ordered spectroscopy (DOSY) is a 2D NMR experiment which correlates chemical shift with diffusion coefficient. Signals of different species within a mixture can be distinguished by their diffusion rates, using data acquired as a function of pulsed field gradient (PFG) strength.[10] The prototype experiment for DOSY is the pulsed field gradient spin echo (PFGSE) (Figure 2.4).[56]

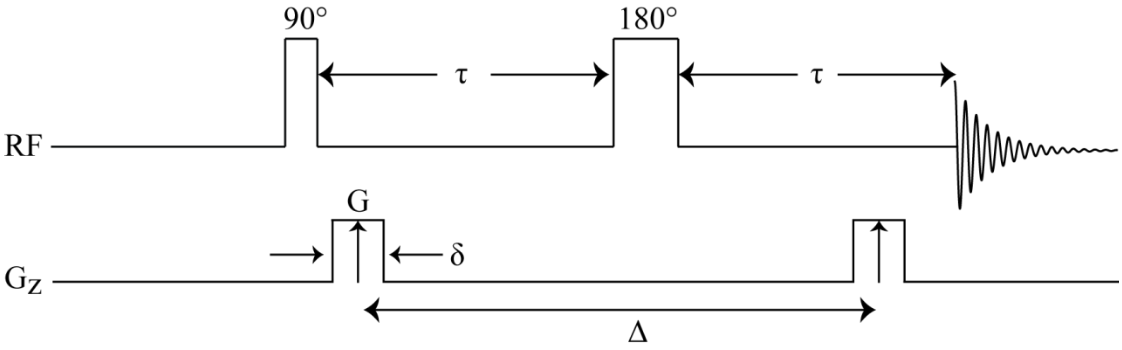

Figure 2.4: Pulsed field gradient spin echo (PFGSE), where G is the amplitude incremented during the experiment, δ the duration of the PFGs and Δ is the diffusion delay measured between the midpoints of the two diffusion encoding and decoding PFGs.

After the equilibrium magnetization $\boldsymbol{M_0}$ has been excited into the transverse plane by the 90° pulse, a PFG is applied and the spins of the precessing magnetization become defocused; they are now spatially encoded with a position-dependent phase. A diffusion delay Δ allows the spins to diffuse along the gradient direction. A second PFG, of equal duration and amplitude to the first, decodes the position-dependent phase, allowing the 180° pulse to refocus exactly spins, which have had no net movement. Spins that diffuse experience different magnetic field strengths, the effect of which is to cause a distribution of signal phases such that the magnetization cannot be completely refocused. There is a net attenuation of signal $S_{(q)}$, which shows a Gaussian dependence on q (and an exponential dependence on q^2); it is dependent on the rate of diffusion as described by the Stejskal-Tanner Equation 2.59:[10]

$$S_{(q)} = S(0)\ e^{-D \Delta' q^2} \qquad 2.59$$

where D is the diffusion coefficient, Δ' is the effective diffusion delay corrected for gradient pulse width and q is defined as the gradient pulse area, e.g. for a rectangular PFG, $\Delta' = \Delta - \delta / 3$ and $q = \gamma\, \delta\, G$.[10]

In order to optimise the experimental conditions for a given diffusion rate, the parameters G, Δ and δ can be adjusted to give appropriate signal attenuation; however increasing Δ, increases loss of magnetization due to T_2 relaxation (Section 2.4), since the magnetization is in the transverse plane. To allow for diffusion for more viscous liquids, the diffusion delay needs to be increased, but T_2 is much shorter for viscous liquids and hence the loss in magnetization due to T_2 relaxation is more noticeable; to avoid such losses in magnetization, (or for when $T_1 > T_2$), the pulsed-field gradient stimulated echo (PFGSTE) sequence (Figure 2.5) is used.[10, 57, 58]

2.10.2.1. Pulsed field Gradient Stimulated Echo (PFGSTE)

In order to reduce the length of time the magnetization is in the transverse plane, two 90° pulses replace the 180° refocusing pulse. The second 90° pulse rotates only half of the in-phase magnetization to the z-axis, where magnetization decays less rapidly than in the transverse plane; however, using this pulse sequence results in a sensitivity loss of a factor of 2, since the remainder of the magnetization is converted into unobservable terms or is dephased during the diffusion delay. The third 90° pulse rotates the magnetization back into the transverse plane, where it is refocused and detected.

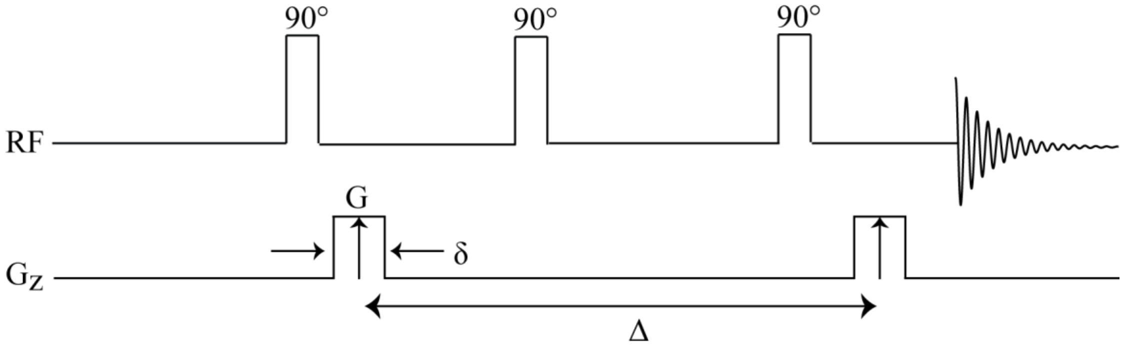

Figure 2.5: Pulsed field gradient stimulated echo (PFGSTE) used to acquire DOSY data adapted from the PFGSE sequence (Figure 2.4) to reduce loss of magnetization through T_2 relaxation; the symbols are as defined in Figure 2.4.

2.10.2.2. Bipolar Pulsed Pair Stimulated Echo (BPPSTE)

The introduction of PFGs to the pulse sequence perturbs the applied magnetic field $\boldsymbol{B_0}$, from which recovery is slow, causing distortions at the start of the FID; in addition, there is interference with the deuterium field-frequency lock.[10, 57] Such disturbances in $\boldsymbol{B_0}$ can arise from eddy currents in conducting parts of the probe and magnet. In modern instruments, these effects are minimized using “actively shielded” gradient coils. Using a bipolar pulsed pair stimulated echo (BPPSTE) sequence, adapted from the PFGSTE, gives a further method for dealing with the disturbances. BPPSTE uses bipolar pairs of PFGs, which are of the same magnitude but of opposite polarity, such that perturbations and interferences partially cancel out (Figure 2.6).[10, 57]

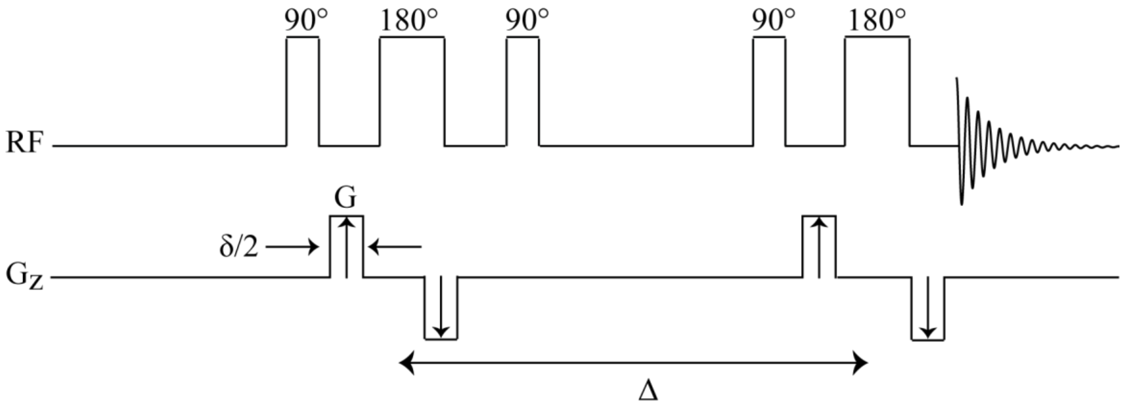

Figure 2.6: Bipolar pulse pair stimulated echo (BPPSTE) pulse sequence used to acquire DOSY data. The sequence is adapted from the PFGSTE sequence of Figure 2.5, with the addition of bipolar pairs of PFGs to partially cancel out perturbations and interferences; the symbols are as defined in Figure 2.4.

Using bipolar PFGs necessitates the inclusion of 180° refocusing pulses, to invert magnetization after the first PFG of the pair, without which the second PFG would simply prevent encoding, and subsequently the decoding, of the magnetization. The deuterium signal does not experience the 180° pulse; therefore, interference to the deuterium field-frequency lock is minimized.

For a multiple pulse sequence, such as those used in DOSY, it is important that unwanted magnetization is suppressed and the desired CTP selected, to avoid unwanted signals causing distortions to the DOSY spectrum. Even with strong gradient pulses, the decay of unwanted signals is not always complete, since the rate of decay is only inversely proportional to the pulse field area.[10] For the BPPSTE sequence, effects can be further compounded, i.e. magnetization can arise from imperfect 180 ° pulses, which results in the bipolar PFGs generating a ‘gradient echo’. Full phase cycling for both the PFGSTE and BPPSTE is therefore important, the latter requiring EXORCYCLE[52] of the 180° pulses.

2.10.2.3. Oneshot

The Oneshot pulse sequence[28] (Figure 2.7), developed from BPPSTE, allows for rapid measurement of a DOSY spectrum without lengthy phase cycling. High resolution spectra can be acquired using only one scan, while still refocusing magnetization as a function of chemical shifts and $\boldsymbol{B_0}$ inhomogeneity. To do this the following adjustments are made. First, the bipolar PFGs are unbalanced to a ratio of $(1+\alpha)$: $(1-\alpha)$, where α is usually between $0.1-0.2$;[10] magnetization not refocused by the 180° pulses is now dephased. Second, the unbalanced PFGs are no longer able to refocus the deuterium lock signal; therefore, to retain the lock, balancing gradient pulses are added to the beginning and end of the diffusion delay Δ. Third, a purge gradient is added to the beginning of Δ to dephase coherences greater than zero order. And fourth, dummy pulses (or heating compensating pulses), can be added before the start of the pulse sequence to keep the net energy dissipated in the gradient coil constant for each transient.[10, 28]

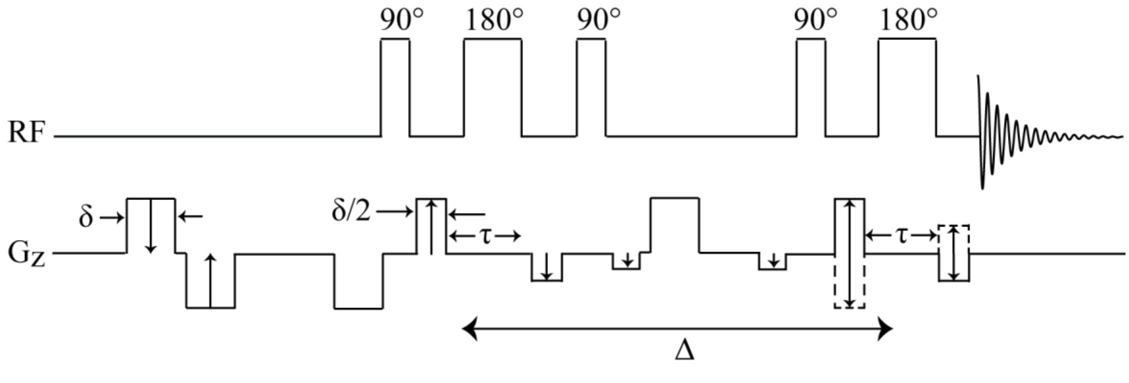

Figure 2.7: Oneshot DOSY sequence adapted from the BPPSTE sequence of Figure 2.6, with added PFGs as explained in the main text; the symbols are as defined in Figure 2.4.

Chapter 3

Increasing the Quantitative Bandwidth of NMR Measurements

3. Increasing the Quantitative Bandwidth of NMR Measurements

3.1. Introduction

Quantitative NMR (qNMR) of ^{1}H and a few other nuclei such as ^{13}C and ^{31}P can give excellent results and as a quantitative tool it is widely used in many areas such as pharmacy and agriculture.[14] However, for many elements with wide frequency ranges, as encountered for nuclei such as ^{19}F (± 300 kHz), it is not possible to achieve quantitative excitation of more than a fraction of the observed chemical shift range. This significant technical problem arises due to limited radiofrequency (RF) pulse power, which causes pulse imperfections such as resonance offset effects (Section 3.1.1, 3.1.2 and 3.1.3), and to a greater or lesser extent B_1 inhomogeneity, to distort signal intensities and signal phases compromising accuracy of quantitative integrals.[26] In order to avoid such effects, it is common to acquire fluorine spectra in sections, with a separate reference compound for each chemical shift range.

Despite this inconvenience, ^{19}F NMR is still widely used and is an important tool in the pharmaceutical industry with a quarter of drugs currently on the market containing fluorine. It offers extremely high resolution due to the combination of wide frequency ranges (± 300 kHz) and only a few fluorine atoms in most drugs. This is unlike ^{1}H NMR, where the resolution is often poor with overlapping signals (Section 4.1). In addition, ^{19}F NMR shares the relatively high sensitivity of ^{1}H NMR with a 100% abundance and high gyromagnetic ratio (γ).

In this chapter a new pulse sequence is introduced CHORUS (**CH**irped, **OR**dered pulses for **U**ltra-broadband **S**pectroscopy),[26] which overcomes the technical problems described above, such that for the first time it is possible to increase the chemical shift range of qNMR by a factor of four or more. The new method, achieves more than

99.9% excitation, with reproducibility better than 0.1%, over a bandwidth of more than 250 kHz, sufficient to allow measurement of the entire shift range of ^{19}F in a single acquisition.

While focused on the important application to qNMR, CHORUS offers a general method that can be used to extend the range of excitation for all types of spectra. It should be applicable to all spin-1/2 nuclides in the Periodic Table, the majority of which have spectra that currently are too wide to be measured in a single acquisition, and thus has potentially important applications across a very wide range of chemistry.

Throughout this chapter and the next, excitation profiles are used to illustrate different stages of development. The profiles have been constructed from a series of individual ^{1}H or ^{19}F spectra, where the frequency of the excitation was varied in steps over a specified range but the receiver was kept on resonance throughout to eliminate any bias caused by the receiver filter characteristics. Also throughout, simulations were carried out in Mathematica *v.9* using compiled analytical solutions of the Bloch equations, which have been adapted or developed from the work of Dr. R. Adams, Dr. M. Foroozandeh and/or Professor G. A. Morris.

3.1.1. The Scale of the Problem

The scale of the problem of resonance offset effect and B_1 inhomogeneity, for a typical 90° pulse and acquire experiment, is illustrated in the excitation profile of Figure 3.1. The data were acquired using a sample of rosuvastatin (an AstraZeneca (AZ) drug) in DMSO-d$_6$ on a 500 MHz spectrometer using a hard 90° pulse width of 8.1 µs and a 4-step phase cycle, EXORCYCLE;[52] the frequency of the excitation was varied in steps of 25 kHz over a 250 kHz (500 ppm) range.

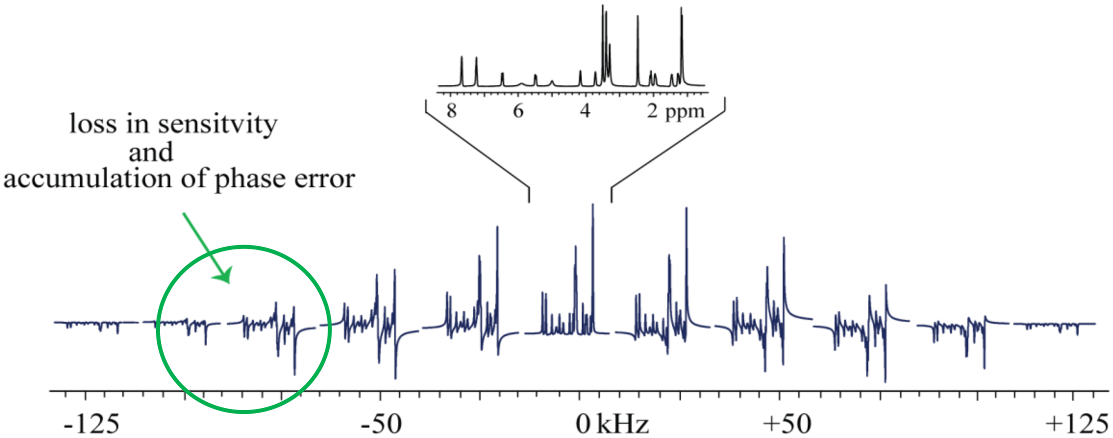

Figure 3.1: ^{1}H excitation profile of rosuvastatin in DMSO-d_6 over a 250 kHz range.

At the centre of the excitation profile, on resonance, the spectrum of rosuvastatin is correctly phased with no loss in signal. However, with increasing resonance offset, towards the edges of the frequency range, there are large losses in signal amplitude and large phase errors, which cannot easily be corrected. This implies that while for ^{1}H NMR spectra, which have a narrow chemical shift range of 10 ppm, quantification is relatively straightforward using hard pulse excitation, this is not the case for nuclei such as ^{13}C and ^{19}F that have much wider chemical shift ranges.

The excitation profile of Figure 3.2 is constructed in a similar manner to Figure 3.1; however, in this example the ^{1}H spectra were acquired using a sample of doped water ($GdCl_3.6H_2O$, 1 mg / ml) in D_2O, and contains only one signal. The Gd^{3+} ion is paramagnetic, with unpaired electrons that increase the T_1 and T_2 relaxation rates. The faster relaxation allows for shorter recovery delays between scans, allowing for faster experiments with more time averaging, which improves signal-to-noise ratio; however, faster relaxation results in a broader signal.

The experiments were performed on a 500 MHz spectrometer using a 90° pulse width of 8.1 μs, with the frequency of excitation varied in steps of 1 kHz over a 300 kHz (600 ppm) range. The profile shows a similar pattern of signal loss and phase distortion to Figure 3.1; however, since the doped sample has only one signal, the profile has a better-defined shape, from which it is easier to evaluate signal loss.

.

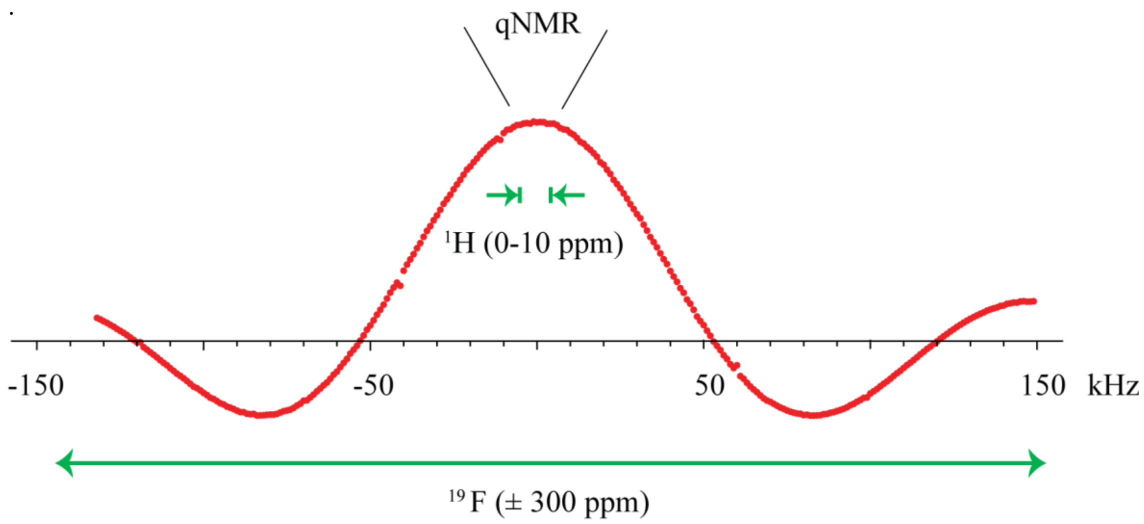

Figure 3.2: Excitation profile using a sample of doped water, over a 300 kHz range. The only portion of the profile to give sufficient uniformity for qNMR is that typically used for proton NMR (0-10 ppm).

3.1.2. Evaluation of Signal Loss

In order to evaluate the loss in signal intensity, simulations of excitation profiles were carried out in Mathematica *v.9*. The red dashed profile of Figure 3.3 was calculated for the same frequency range as Figure 3.2, and since it uses the same 90° pulse width (8.1 µs), the profiles are superimposable.

To evaluate the scale of the problem for fluorine, profiles were simulated using a typical 90° pulse width of 12.5 µs. The profiles are shown with (purple) and without (green) a linearly frequency-dependent phase correction, corresponding to a delay of $2\text{pw}/\pi$ (Figure 3.3).

For the phase corrected profile (purple), on a 500 MHz spectrometer, the losses in signal intensity towards the edges of the frequency range for a narrow bandwidth (^{1}H, ± 5 ppm) and wide bandwidth (^{19}F, ± 200 ppm), are respectively negligible and almost total (86%). Thus, the scale of the problem is illustrated both graphically and numerically.

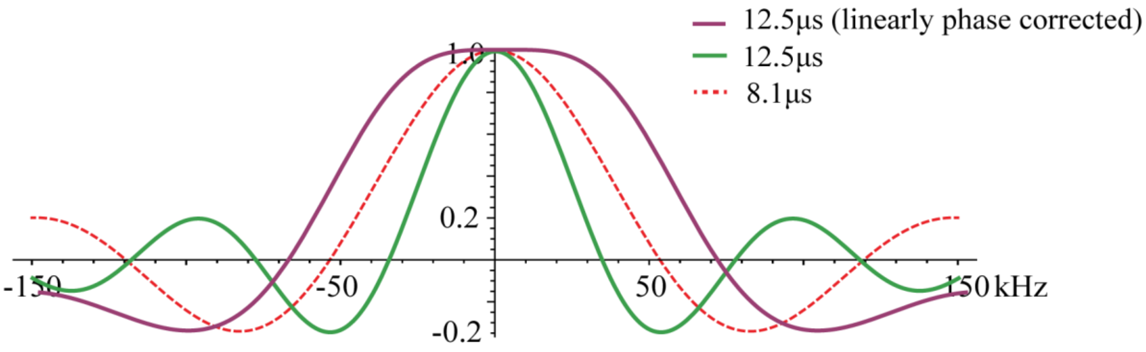

Figure 3.3: Simulated excitation profiles using a 90° pulse width of 8.1 μs (red dashed line) and 12.5 μs (green and purple lines), over a spectral width of ± 150 kHz, where the purple profile has been corrected for a linearly frequency-dependent phase error corresponding to a delay $2pw/\pi$. The simulations were adapted from the work of Professor Gareth Morris.

3.1.3. The Nature of the Problem: Resonance Offset Effects

To excite very wide frequency ranges is very challenging since pulse imperfections such as resonance-offset effects, due to the limited radiofrequency power available for pulsed excitation, distorts both signal intensities and signal phases, greatly reducing the excitation bandwidths, as illustrated in Sections 3.1.1 and 3.1.2.

For ^{1}H NMR (0-10 ppm / 5 kHz), a typical 90° pulse width of 8.1 μs ($\gamma B_1 / 2\pi \approx 30$ kHz), will generate an effective field B_{eff} (Section 2.1) of sufficient strength to excite all the resonances in the spectrum fully. This is not the case for ^{19}F NMR, i.e. up to 300 kHz frequency range, where for a typical pulse width of 12.5 μs ($B_1 \equiv 20$ kHz), the bandwidth of excitation falls far short of that required.

The effect of increasing resonance-offset from 0 kHz to 60 kHz is shown in the Bloch sphere of Figure 3.4a for a simple 90° excitation. When a pulse is applied along the *x*-axis on-resonance, the effective field B_{eff} experienced by the spins is the same as the

B_1 field and the magnetization precesses in the *yz*-plane. When off-resonance the fields are no longer the same, so the magnetization trajectory curls up from the *x*-axis towards the *z*-axis, away from the *zy*-plane, and the excitation experienced by the spins is reduced (Figure 3.4b).

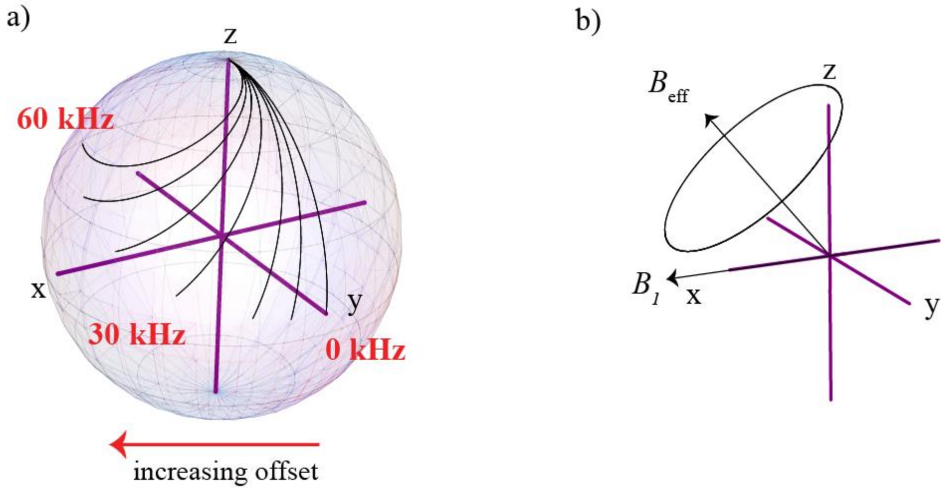

Figure 3.4: a) The Bloch sphere, showing the paths the magnetization takes using simple 90° excitation with increasing offset from the transmitter frequency; b) shows that when the applied field B_1 is not at the Larmor frequency of the spins, the effective field B_{eff} is tilted up towards the *z*-axis. The simulations were adapted from the work of Dr. Ralph Adams.

3.2. Adiabatic Pulses

In the quest to overcome pulse imperfections such as B_1 inhomogeneity and resonance offset effects, many different types of RF excitation have been developed, e.g. composite pulses[16, 17, 59-62] and adiabatic pulses. For the latter, the pulses are swept-frequency, which means that the transmitter frequency is rapidly swept over a wide range of spectral frequencies during the pulse. This is in contrast to conventional pulsed excitation, where the transmitter frequency is generally set at the centre of the spectral window, so that the full frequency range is excited simultaneously.

For the purposes of overcoming offset dependence and B_1 inhomogeneity, two types of swept-frequency pulses[16-25] are reviewed here, hyperbolic secant (Section 3.2.4) and chirp (Section 3.2.5). To achieve adiabaticity for any such pulse, the following adiabatic condition must be satisfied.

3.2.1. Adiabatic Condition

The adiabatic theorem is a quantum mechanical concept and was introduced in 1928 by Born and Fock. It states that if a system is perturbed such that the change is sufficiently slow and gradual, the wave function can adapt to the changing conditions. At the end of the perturbation, the system is in an eigenstate of the final Hamiltonian that corresponds to the initial eigenstate it started with. In NMR spectroscopy, the theory of adiabaticity is applied to swept-frequency pulses, as described in the frequency modulated (FM) frame of reference.

3.2.2. Frames of Reference

The rotation of a magnetization vector M about the effective field B_{eff}, during an adiabatic pulse, is best explained using the visual representation of the frequency modulated (FM) frame of reference, which is a co-ordinate system defined by axes (x', y', z'). The FM frame is comparable to the conventional frame of reference (Section 2.1.2), where B_1^- defines the x-axis; however, in the context of adiabatic pulses, in the FM frame, the frequency is constantly changing.

A more helpful frame of reference is a secondary frame of reference, the effective field (B_{eff}), defined by the co-ordinates (x'', y'', z'').[16, 19, 61, 63] In this frame of reference B_{eff} defines the z''-axis, where the orientation of the B_{eff} frame changes at a rate relative to the FM frame.

With respect to the FM frame, M is rotated with an instantaneous frequency of the radiofrequency pulse (ω_{RF}) at an angular frequency (or velocity) ($\mathrm{d}\theta/\mathrm{d}t$), where angle θ is the tilt (flip) angle (Section 2.1.2, Figure 2.1). The rate of the sweep is determined only by the frequency modulation $\omega_{\mathrm{RF}}(t)$ of the pulse while the direction of the RF field vector $B_1(t)$ remains fixed. Equation 3.1 shows the offset from resonance $\Delta\omega$, when the RF field is at frequency ω_{RF} and ω_0 is the Larmor frequency:[16]

$$\Delta\omega = \omega_0 - \omega_{\mathrm{RF}} \qquad 3.1$$

Along the z'-axis in the FM frame, the reduced field ΔB (Section 2.1.2) component is given by $(\Delta\omega/\gamma)$. Therefore, the effective field B_{eff} experienced by the spins is defined as the vector sum of $\Delta\omega/\gamma$ and $B_1(t)$. Consider a swept-frequency (chirp) pulse that starts with $\omega_{\mathrm{RF}} \ll \omega_0$ and ends with $\omega_{\mathrm{RF}} \gg \omega_0$, then at the beginning of the pulse B_{eff} is approximately collinear with z'-axis. As ω_{RF} increases, B_{eff} rotates toward the transverse plane until it is equal to ω_0; this corresponds to an adiabatic half passage (AHP) pulse. An adiabatic full passage (AFP) pulse is when the frequency sweep continues until B_{eff} is orientated along $-z'$, to give a maximum value of $-\Delta\omega$.

The adiabatic condition of Equation 3.2 ensures that the orientation of B_{eff} changes very slowly in comparison to the rate of precession of the magnetization vector M, such that it follows $B_{\mathrm{eff}}(t)$ for all values of t. In other words, the criterion is defined by how well M stays spin locked to the B_{eff} field throughout the pulse:

$$|\gamma B_{\mathrm{eff}}(t)| \gg |d\theta/\mathrm{d}t| \qquad 3.2$$

When B_{eff} is large, e.g. far off-resonance, the adiabatic condition is more easily satisfied in comparison to on-resonance, i.e. $B_{\mathrm{eff}} \approx B_1$.

The adiabaticity factor Q (Equation 3.3) is a measure of the extent to which the adiabatic condition is met; in typical uses Q is 5:[33, 64]

$$Q = \frac{\omega_{\mathrm{eff}}}{|\mathrm{d}\theta/\mathrm{d}t|} \qquad 3.3$$

The adiabatic condition can be achieved by using a relatively high B_1 amplitude, or alternatively by slow frequency sweep.[16] Adiabatic pulses are referred to as “fast passage”,[19, 65] where the total pulse duration of the adiabatic rotation, must be more rapid than relaxation processes (Section 2.4).

3.2.3. Adiabaticity and B_1 Insensitivity

As noted in the previous section, AHP and AFP give respectively B_1 independent excitation and inversion of magnetization initially at zero. Of course, if the magnetization is not initially at equilibrium its final state may not be B_1 independent. This problem is encountered using the double HS and double chirp sequences (Section 3.3.2), where the refocusing element (180° pulse) is adiabatic but not B_1 independent such that the strength of B_1 affects the phase of the refocused magnetization. The problem is solved by adding the 3rd pulse in the sequence ABSTRUSE (Section 3.3.2.5).

One advantage of the robustness of adiabatic pulses to B_1 inhomogeneity (over wide frequency ranges), is in their application in biomedical NMR applications, e.g. *in vivo* NMR, where large volumes of tissues (whole organisms) are analysed. Surface coils are unable to generate uniform B_1 field throughout the sample; however, using such pulses allows useful experiments still to be performed.[65]

3.2.4. The Hyperbolic Secant (HS) Pulse

The use of hyperbolic secant (HS) pulses in NMR was derived from its use in coherent optics.[66, 67] In NMR, HS pulses are typically used for band-selective inversion.[66] With respect to the former and under the adiabatic condition, any bandwidth of inversion can be achieved with appropriate choice of pulse duration and sweep width.

For band-selective inversion, the HS pulse has the advantage of sharp transitions, where outside the transition zone there is little effect.[25]

The complex hyperbolic secant (sech) waveform is given by Equation 3.4:

$$B_1(t) = B_1^0 \left(\text{sech}\,(\beta\, t)\right)^{1+\mathrm{i}\mu} \quad \text{or} \quad B_1(t) = B_1^0\, \text{sech}\,(\beta\, t)\mathrm{e}^{\,\mathrm{i}\mu \ln \text{sech}\, \beta t} \qquad 3.4$$

where the parameters μ and β determine the degree of phase modulation and truncation respectively, where typically the truncation is at 1% of the amplitude function; both μ and β combine to define the usable bandwidth $(\Delta\omega_{\mathrm{BW}} = 2\,\mu\,\beta)$.[65, 66]

The differential of the modulated phase (Equation 3.5) gives the modulation frequency $\Delta\omega(t)$ of Equation 3.6:[65, 66]

$$\varphi(t) = \mathrm{i}\,\mu\ \ln \text{sech}(\beta\, t) \qquad 3.5$$

$$\Delta\omega(t) = -\mu\,\beta \tanh\ (\beta\, t) \qquad 3.6$$

The RF amplitude required for a 180° HS pulse $\left(\gamma\, {B_1}^{180}/2\pi\right)$ can be calculated from Equation 3.7:[25]

$$\frac{\gamma\, B_1}{2\pi} = k\sqrt{\frac{f_{\max}}{T_{\mathrm{p}}}} \qquad 3.7$$

where $f_{\max}$ is the frequency sweep (Hz), T_{p} is the pulse duration (s) and k is a factor which defines the threshold for adiabaticity.

Equation 3.7, as taken from the literature Cano *et al*[25], is only approximate; however, as long as $f_{\max} \gg T_{\mathrm{p}}^{-1}$ then it is fairly accurate.

The HS pulse is the product of the pulse amplitude and the modulated phase, the profiles of which are illustrated in Figures 3.5a, 3.5b and 3.5c respectively.

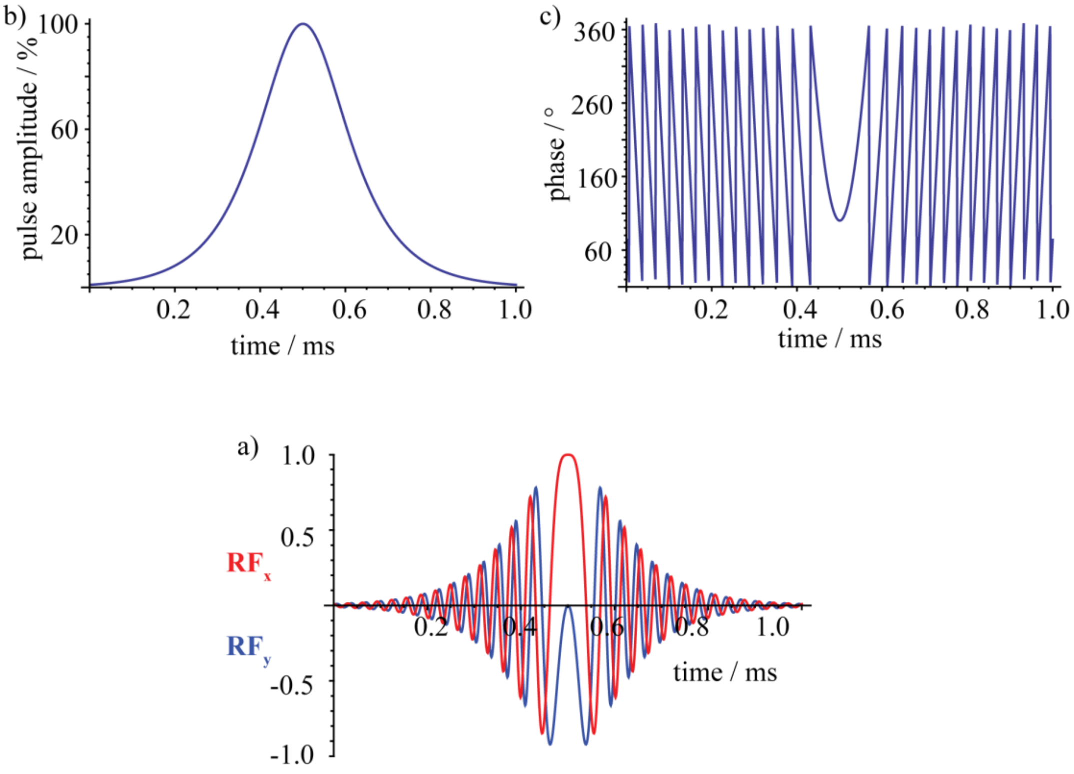

Figure 3.5: a) HS pulse, with real (red) and imaginary (blue) parts, using 1000 points, a total sweep (ΔF) of 64 kHz (k = 1.93) and a pulse duration of 1 ms; b) and c) amplitude and modulated phase of the HS pulse respectively.

3.2.5. Chirp Pulses

In contrast to the hyperbolic secant pulse, the chirp pulse has a linear frequency sweep:

$$f(t) = f_0 + k\,t \qquad 3.8$$

where f_0 is the starting frequency at time $t = 0$, f_1 is the final frequency, k is the rate of frequency increase (or chirp rate) and $f(t)$ varies linearly with time:

$$k = \frac{f_1 - f_0}{t_1} \qquad 3.9$$

The complex chirp waveform is expressed as Equation 3.10:

$$B_1(t) = A(t)e^{i\varphi(t)} \qquad 3.10$$

where A is the amplitude. The $\omega(t)$ can be integrated to give the quadratic phase:

$$\varphi\,(t) = \varphi_0 + 2\pi\left(f_0\,t + \frac{k}{2}\,t^2\right) \qquad 3.11$$

where φ_0 is the initial phase at time $t = 0$.

The RF amplitude required for a 180° chirp pulse $\left(\gamma\, B_1{}^{180}/\,2\pi\right)$ can be calculated from Equation 3.12:

$$\frac{\gamma\,B_1}{2\pi} = \sqrt{\frac{\left(T_{\mathrm{p}} \times Q \times \Delta F\right)}{2\pi}}\Big/T_{\mathrm{p}} \qquad 3.12$$

where ΔF is the total sweep width (Hz), T_{p} is the pulse duration (s) and Q is the adiabatic factor as defined by Equation 3.3.

The modulated chirp pulse is the product of the pulse amplitude and the modulated phase, the profiles of which are illustrated in Figures 3.6a, 3.6b and 3.6c respectively.

Throughout this chapter (and most of the next), the RF amplitude at the edges of the chirp pulses used, have 5% smoothing applied. This removes the effect of lack of adiabaticity at the edges of the pulse, when the RF power is in transition from zero to maximum (or vice versa).[22, 26]

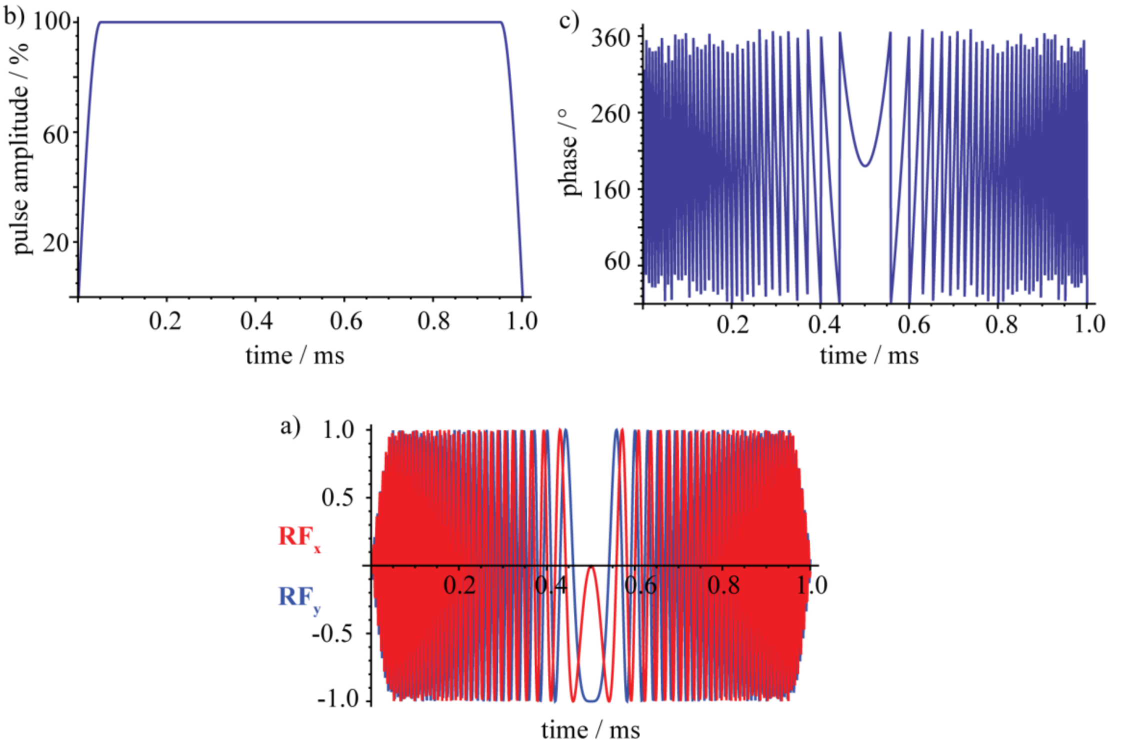

Figure 3.6: a) Chirp pulse, with real (red) and imaginary (blue) parts, using 1000 points, 5% smoothing, adiabaticity factor (*Q*) of 5, a total sweep (ΔF) of 300 kHz and pulse duration of 1 ms; b) and c) amplitude and modulated phase of the chirp pulse respectively.

3.3. Development of New Broadband Sequence

3.3.1. Introduction

For broadband excitation, using a 90° HS or chirp pulse is not so straightforward. Figure 3.7 illustrates the excitation profile of a 90° chirp of pulse duration 2 ms, excited over a 100 kHz bandwidth, where the RF amplitude for a 90° element $\left(\gamma B_1^{90}/2\pi\right)$ is calculated using Bloch sphere simulation, as explained in Section 3.3.2.

Constant signal amplitude is maintained over the full bandwidth even when far off resonance (± 50 kHz), unlike excitation using a 90° hard pulse (Section 3.1.2, Figure 3.3). However, due to the frequency modulation of the chirp (or HS), the excitation produced varies very rapidly in a nonlinear fashion with resonance offset, because of the time-dependent accumulation of phase. If swept-frequency pulses are to be used for broadband excitation, and specifically for qNMR, then the phase variation has to be overcome.

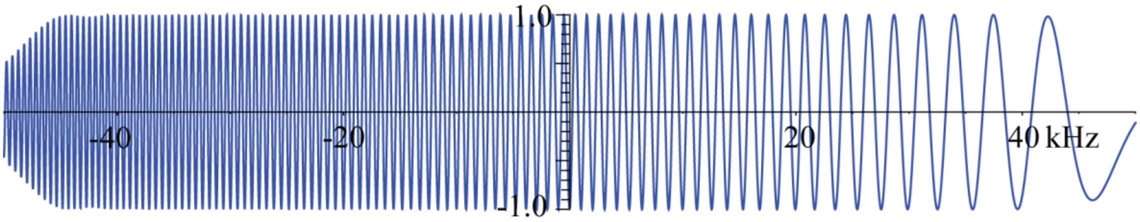

Figure 3.7: Simulated excitation profile of *y*-magnetization using a 90° adiabatic chirp pulse of 2 ms duration, in steps of 20 Hz, over 100 kHz range.

3.3.2. Double Chirp vs Double HS

3.3.2.1. Introduction

For swept-frequency pulses, much of the phase variation can be refocused by combining 90° and 180° pulses of appropriate relative duration and amplitude, as developed by Bodenhausen *et al.*[20] However, the refocusing element, even though adiabatic, cannot refocus all of the phase variation, as is particularly apparent for the double chirp sequence, illustrated in Figure 3.8c (Section 3.3.2.3).

3.3.2.2. Experimental I

The excitation profiles of Figure 3.8c are simulated over a 300 kHz bandwidth using the double chirp (Figure 3.8a), the double HS (Figure 3.8b) and the hard 90° 180° spin echo sequences, where the RF amplitudes of the elements, $\left(\gamma B_1^{180}/2\pi\right)$ and $\left(\gamma B_1^{90}/2\pi\right)$, of the double chirp and double HS sequences were determined as follows:

180° chirp element $\left(\gamma B_1^{180}/2\pi\right)$

For 10000 points, using a sweep width (ΔF) of 300 kHz, for unit pulse duration $\tau = 1$ ms and Q factor of 5, the RF amplitude $\gamma B_1^{180}/2\pi$, as generated by the Bruker software, was 15451 Hz.

180° HS element $\left(\gamma B_1^{180}/2\pi\right)$

For the purposes of consistency, the same RF amplitude of 15451 Hz and 10000 points were used. Using Equation 3.7, for a unit pulse duration $\tau = 1$ ms and k factor of 1.93, as taken from the literature,[25] the sweep width was calculated to be 64.09 kHz, which translates to a Q factor of approximately 3.42, when generated in the Bruker software.

90° chirp element $\left(\gamma B_1^{90}/2\pi\right)$

The RF amplitude for the 90° element $\left(\gamma B_1^{90}/2\pi\right)$ was estimated by Bloch sphere simulation, i.e. by using a 180° pulse shape with a pulse duration, e.g. $\tau_{\pi/2} = 2$ ms, the RF amplitude of the pulse shape was reduced until the optimal conversion of magnetization from longitudinal to transverse excitation was obtained. From this estimated value, the RF amplitude ratio $\left(\gamma B_1^{90}/2\pi : \gamma B_1^{180}/2\pi\right)$ for a Q factor of 5, was optimized by experiment and simulation to give a ratio of 4.75 : 1, therefore $\gamma B_1^{90}/2\pi = 3252.8$ Hz.

90° HS element $\left(\gamma B_1^{90}/2\pi\right)$

$\gamma B_1^{90}/2\pi$ of 3453.1 Hz was calculated using Equation 3.7, using a k factor of 0.61 as taken from the literature[25] and using a sweep width of 64.09 kHz.

For the swept-frequency sequences of Figures 3.8a and 3.8b, it is necessary that the sweep rate of the refocusing pulse be twice that of the excitation pulse, i.e. $(\tau_{180} = \tau_{90}/2)$, with an added delay of τ_{180}. This allows the free precession of the magnetization in the transverse plane, at the lower end of the frequency sweep, which begins at the start of the first pulse, to synchronize with the free precession of the magnetization at the end of the first pulse, at the higher end of the frequency sweep.[20]

3.3.2.3. Results and Discussion I

The double chirp sequence has a wider bandwidth of excitation compared to both the hard and double HS sequences; however, large phase errors build up towards the edges of the frequency range (Figure 3.8c). For the double HS sequence, the phase error is small, with a sharp, well-defined transition zone, which lends itself well to band-selective excitation but not so well to broadband excitation. For the same maximum RF amplitude (15.5 kHz), the double chirp has a clear advantage over the double HS, despite the larger phase errors.

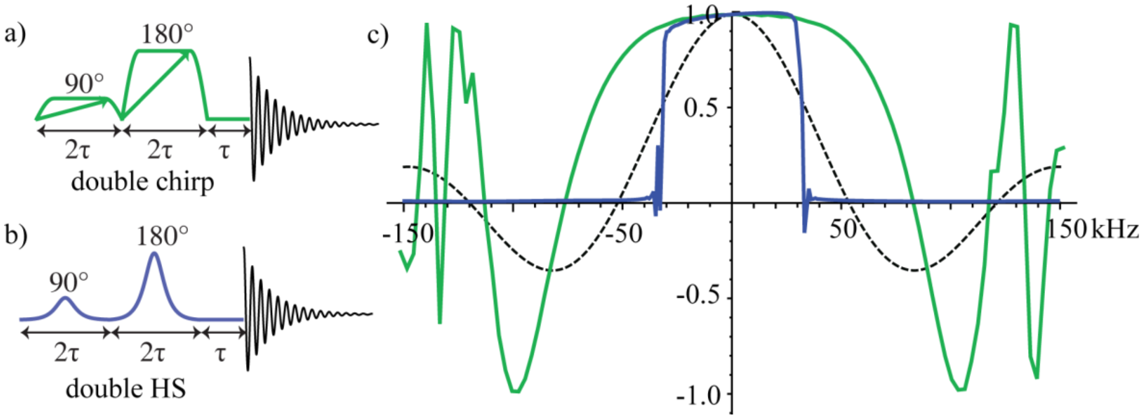

Figure 3.8: c) Simulated excitation profiles of *y*-magnetization over a 300 kHz range for a hard 90° 180° spin echo sequence (black dashes), and for the double chirp (green) and the double HS (blue) sequences of Figures 3.8a and 3.8b respectively. A 4-step phase cycle, EXORCYCLE, was used.

3.3.2.4. Experimental II

To verify the calculations of Figure 3.8c, experimental data for the double chirp and a hard 90° excitation were acquired. The experiments were carried out on a Bruker 500 MHz system using a doped water sample and a hard 90° pulse width of 8.1 μs, with the frequency of the excitation varied in steps of 1 kHz over a 300 kHz range and a 4-step phase cycle, EXORCYCLE.[52] The chirp pulses were generated in Bruker software in the Bruker format with the same parameters for points, smoothing, adiabatic factor (Q), total sweep width (ΔF), pulse durations and RF amplitudes as used for the simulation outlined in Section 3.3.2.2.

3.3.2.5. Results and Discussion II

The experimental data of Figure 3.9b highlight a second limitation (the first being the large phase errors already observed). This is more of a hidden problem, that the signal phase is extremely sensitive to B_1 amplitude, so that B_1 inhomogeneity causes large ($>$ 30%) losses in signal even with modern probes, as shown in the experimental data (red dots).

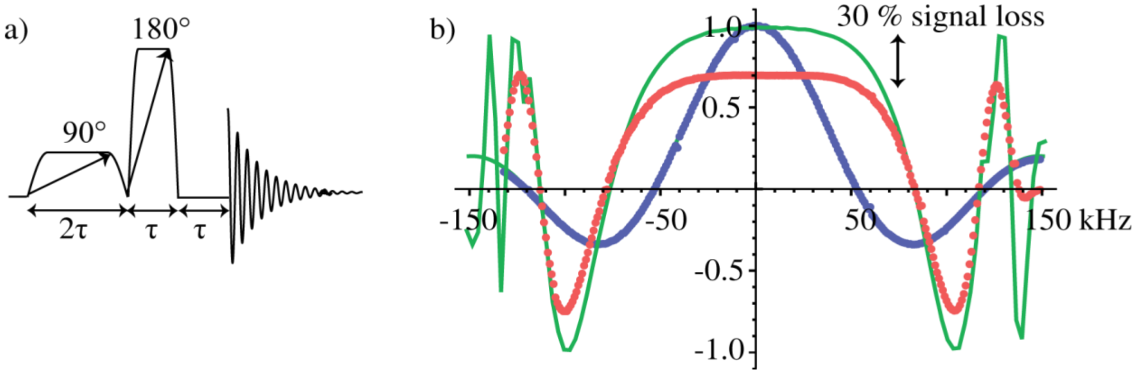

Figure 3.9: a) Double chirp sequence of Bodenhausen *et al*;[45] b) excitation profiles of experimental data (dots) for a doped water sample and simulations (green lines) for a hard pulse (blue) and for the chirp pulse sequence (red) of Figure 3.9a, where for the hard pulse, a 90° pulse width of 8.1 μs was used. The experimental data for the first eighteen experiments were disregarded due to the limited coherence range of the spectrometer synthesiser, which was not able to generate data at the lower end of the frequency range.

Oversensitivity to B_1 inhomogeneity is due to the Bloch-Siegert effect.[68] The effect can be corrected by addition of a second 180° element of duration τ, to form a double echo, where the added 180° pulse is able to refocus the phase dispersion. The double echo for the HS pulse, ABSTRUSE (Adjustable, Sech/Tanh-Rotation Uniform Selective Excitation) sequence was developed by Cano *et al.*[25]

Using the same logic as ABSTRUSE, the double chirp sequence (Figure 3.9a) was adapted by the addition of a 180° pulse, of appropriate amplitude and duration, and a delay τ, to form a B_1 insensitive triple chirp sequence.[26]

3.3.3. Compensation for B_1 Sensitivity

The magnitudes of B_1 sensitivity of the double chirp (Figure 3.10a) and triple chirp (Figure 3.10c) sequences are illustrated in the graphs of Figure 3.10b and Figures 3.10d and 3.10e respectively, where the differential of phase with respect to relative RF amplitude (α) is plotted as a function of α, where α is $B_1 / B_{1\mathrm{opt}}$.

3.3.3.1. Experimental

For Figure 3.10b, using sequence Figure 3.10a and a 4-step phase cycle, EXORCYCLE, the pulses were generated using the same parameters for a 300 kHz range as outlined in Section 3.3.2.2. For Figure 3.10d, using sequence Figure 3.10c and a 16-step phase cycle, the pulses were generated using 5% smoothing and a Q factor of 5, with 2000 points used for pulses one and two, and 1000 points for pulse three. For a sweep width (ΔF) of 300 kHz and for unit pulse duration $\tau = 1$ ms, the RF amplitudes were $\gamma B_1^{90} / 2\pi = 3252.8$ Hz, $\gamma B_1^{180\ \mathrm{first}} / 2\pi = 10925.5$ Hz and $\gamma B_1^{180\ \mathrm{second}} / 2\pi = 15451$ Hz. For Figure 3.10e, the RF amplitude of the first 180° pulse of Figure 3.10c was reduced by 3 % to $\gamma B_1^{180\ \mathrm{first}} / 2\pi = 10597.7$ Hz ; this optimizes the sequence to give zero phase gradient at $\alpha = 1$, with a Q of 4.71 instead of 5.

3.3.3.2. Results and Discussion

As is expected from the large loss in signal in Figure 3.9b, Figure 3.10b shows a large phase dependence on relative RF amplitude (α), which is non-zero at α (1). As can be seen in Figures 3.10d and 3.10e, addition of a second 180° pulse reverses the phase variation with B_1 of the magnetization. The graphs of differential of phase of Figures 3.10d and 3.10e give zero phase gradients at different values of α, where Figure 3.10e is the optimum value of α. The triple chirp sequence is now B_1 insensitive; however, some residual phase error remains, as illustrated in Figures 3.11a and 3.11b (Section 3.3.4).

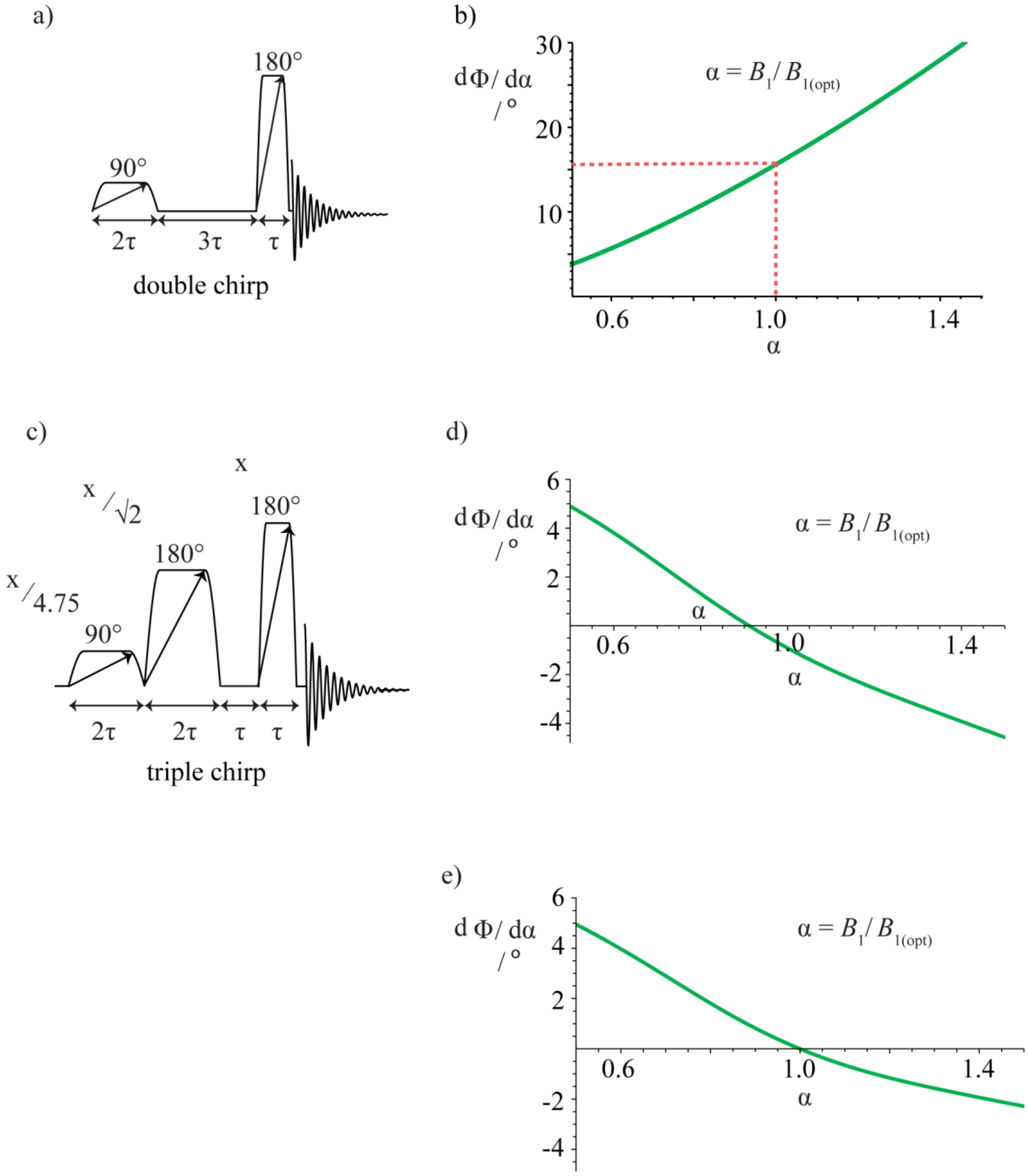

Figure 3.10: b), d) and e) Graphs of differential of phase with respect to relative RF amplitude (α) as a function of α, where α is B_1 / $B_{1\mathrm{opt}}$; α was incremented in steps of 0.01 over an RF ratio range of 0.5 – 1.5. For graph b), sequence a) was used; for graphs d) and e), sequence c) was used, which for graph e) the RF amplitude of the first 180° pulse was reduced by 3 % to obtain zero phase gradient at α = 1. For sequence c), the pulse amplitude ratio is (0.21 : 0.71 : 1); the RF amplitude (x) $\left(\gamma B_{1(\mathrm{max})} / 2\pi\right)$ for the given experimental parameters, is x = 15451 Hz. The simulations were adapted from the work of Dr. M. Foroozandeh.

3.3.4. Correction of Residual Phase Error

Having corrected the B_1 sensitivity, residual phase error remains (Figures 3.11a and 3.11b), which has a nonlinear dependence on excitation frequency. However, since chirp pulses use a linear frequency sweep, there is a one-to-one correspondence between time and frequency in the pulse; therefore, the phase variation as a function of frequency can be corrected by numerical optimization.

For the purposes of analysis, an excitation profile was simulated using the triple chirp pulse sequence of Figure 3.10c, using the same parameters as in Section 3.3.3.1, where a 90° pulse width of 8.1 µs and a 16-step phase cycle were used. To the central portion of the simulation (Figure 3.11b, red dots) a polynomial was fitted, as documented in the supplementary information of Power *et al*;[26] the edges of Figure 3.11b (green dots) were ignored, since they were distorted by the amplitude smoothing at the edges of the chirp pulses. The corresponding time-dependent phase correction $\Delta\emptyset(x)$ (Equation 3.13) was then subtracted from the first and second pulses of the triple chirp. The resulting effect is to achieve constant-phase excitation over approximately 250 kHz (Figure 3.11c).

$$\begin{aligned}\Delta\emptyset(x) = {} & 262.552 + 11.4628\,x - 19.0628\,x^2 + 27.249\,x^3 + 155.681\,x^4 \\ & - 177.911\,x^5 - 429.253\,x^6 + 356.946\,x^7 + 365.884\,x^8 - 245.483\,x^9\end{aligned} \qquad 3.13$$

where $x = (2t - \mathrm{pw}) / 2\mathrm{pw}$, pw is the chirp pulse width, and t is the time from the beginning of the pulse.

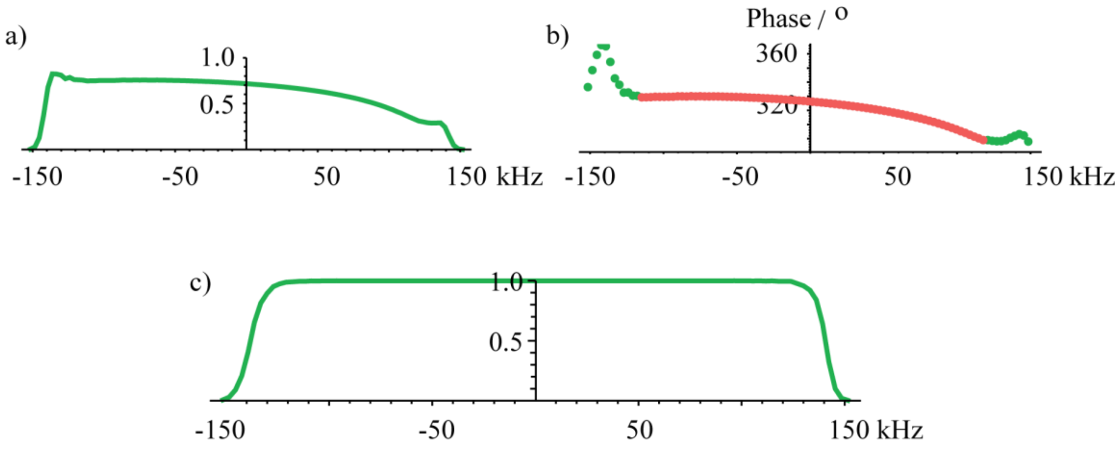

Figure 3.11: a) Excitation profile of *y*-magnetization, using the triple chirp sequence of Figure 3.11c, with the same parameters as Section 3.3.3.1. b) Residual phase error of Figure 3.11a, where the signal phase (dots) is given as a function of frequency; the green dots at the higher and lower ends of the frequency range are the unreliable data due to the pulse amplitude smoothing. c) Uniform excitation profile, where the residual phase error (Figure 3.11b, red dots) has been been corrected by numerical optimization using a polynomial fitting function.

3.3.5. CHORUS

The uniform constant-phase profile of Figure 3.11c is the result of adapting and extending the double chirp sequence (Figure 3.9a), to compensate for sensitivity to B_1 inhomogeneity (Figures 3.10d and 3.10e), and with numerical correction of the remaining phase variation (Figure 3.11b). The resultant triple chirp sequence, CHORUS (**CH**irped, **OR**dered pulses for **U**ltra-broadband **S**pectroscopy), offers a new technique for broadband excitation over very wide frequency ranges.

3.3.5.1. Experimental

To verify the calculations of Figure 3.11c, experimental data were acquired for CHORUS and hard 90° excitation using a heavily doped sample of C_6F_6 in DMSO-d_6, using a hard 90° pulse width of 12.4 μs.

The experiments were performed on a Bruker 500 MHz system, with the frequency of the excitation varied in steps of 6 kHz over a 300 kHz range using a 64-step phase cycle. The chirp pulses used for CHORUS were generated in a Matlab notebook developed by Dr. M. Foorzandeh, as outlined in the supplementary information of Power *et al*,[26] with the time-dependent phase correction $\Delta\emptyset(x)$ subtracted from the first 90° and 180° chirp elements. The parameters for the chirp pulses were as outlined in Section 3.3.3.1.

For the hard 90° excitation, both experiment and simulation use a linear frequency-dependent phase correction, corresponding to a delay of $2\mathrm{pw}/\pi$; for CHORUS no correction is needed.

3.3.5.2. Results and Discussion

CHORUS achieves constant amplitude and constant phase excitation over a 250 kHz bandwidth, as shown in Figure 3.12, with no undue B_1 insensitivity. The maximum RF amplitude of 15.5 kHz, for a unit pulse duration $\tau = 1$ ms and frequency sweep of 300 kHz, is less than that of a hard 90° pulse.

The typical chemcial shift ranges for 3 nuclei, ^{19}F (± 300 ppm at 470 MHz, red), ^{13}C (0-200 ppm at 126 MHz, purple) and ^{1}H (0-10 ppm at 500 MHz, blue), are compared and indicated by the arrows, showing that CHORUS is able to excite almost the full ^{19}F chemical shift range.

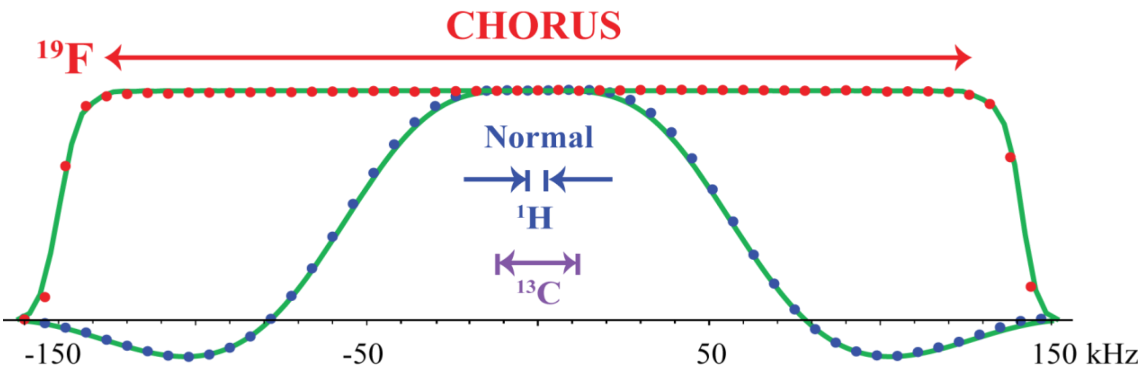

Figure 3.12: Experimental (dots) and calculated (solid lines) ^{19}F excitation profiles for CHORUS (red) and hard 90° pulse excitation (blue) over a 300 kHz bandwidth.

The CHORUS profile shows slight asymmetry. This is due to T_2 relaxation during the pulse sequence of 6 ms total duration, since the sample was heavily doped ($T_2 = 0.05$ s).

From the data of Figure 3.12, it is calculated that for a given RF amplitude and at 98% excitation, CHORUS achieves 5.8 times greater bandwidth than that for a hard 90° pulse of the same peak RF amplitude, and 4.2 times greater than that for ABSTRUSE (Figure 3.13).

3.3.5.3. CHORUS vs ABSTRUSE

Figure 3.13 compares the simulated excitation profiles for ABSTRUSE, using HS pulses, and CHORUS. For ABSTRUSE, the parameters of points and unit pulse duration were the same as for CHORUS, while the RF amplitudes of the former were $\gamma B_1^{90}/2\pi =$ 3453.1 Hz, $\gamma B_1^{180\ \mathrm{first}}/2\pi =$ 10359.4 Hz and $\gamma B_1^{180\ \mathrm{second}}/2\pi$ = 15451 Hz, calculated using Equation 3.7, for k values of 0.61, 1.83 and 1.93 respectively, as taken from the literature.[25] Figure 3.13c shows the in-phase component of magnetization, while Figure 3.13d shows the signal obtained after a linear phase correction is applied to ABSTRUSE (no correction is needed for CHORUS).[26]

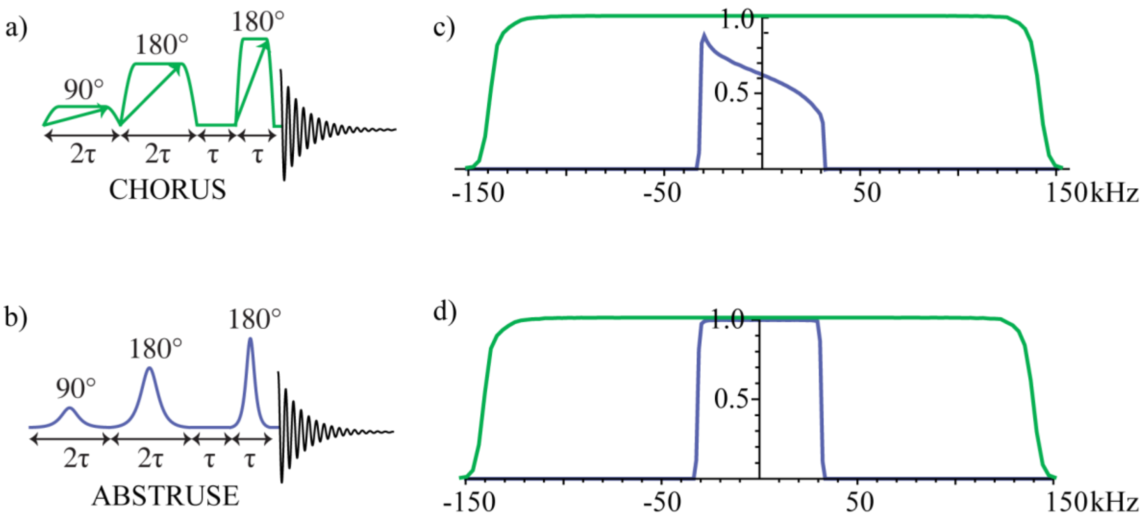

Figure 3.13: a) and b) CHORUS and ABSTRUSE pulse sequences respectively; c) and d) calculated signal c) and phase-corrected signal d) profiles for sequences a) (CHORUS, green) and b) (ABSTRUSE, blue) respectively.

3.3.6. Summary

The excitation profiles of Figure 3.13 show that ABSTRUSE is not suitable for broadband excitation. In contrast, CHORUS, using tailored ultra-broadband swept-frequency chirp pulses, successfully excites very wide bandwidths.

Figure 3.14 compares excitation profiles acquired using hard 90° excitation, taken from Section 3.1.1 (Figure 3.1, blue), and CHORUS (red), where the data were acquired using the same sample of rosuvastatin in DMSO-d_6 and the same experimental conditions (Section 3.1.1). From this figure it is clear that CHORUS successfully overcomes the effects of pulse imperfections (resonance offset effects and B_1 inhomogeneity), refocusing the magnetization as a function of both Larmor frequency and RF field. The spectrum of rosuvastatin, as far off resonance as ± 125 kHz (and beyond), can be easily phased with no observable loss in signal.

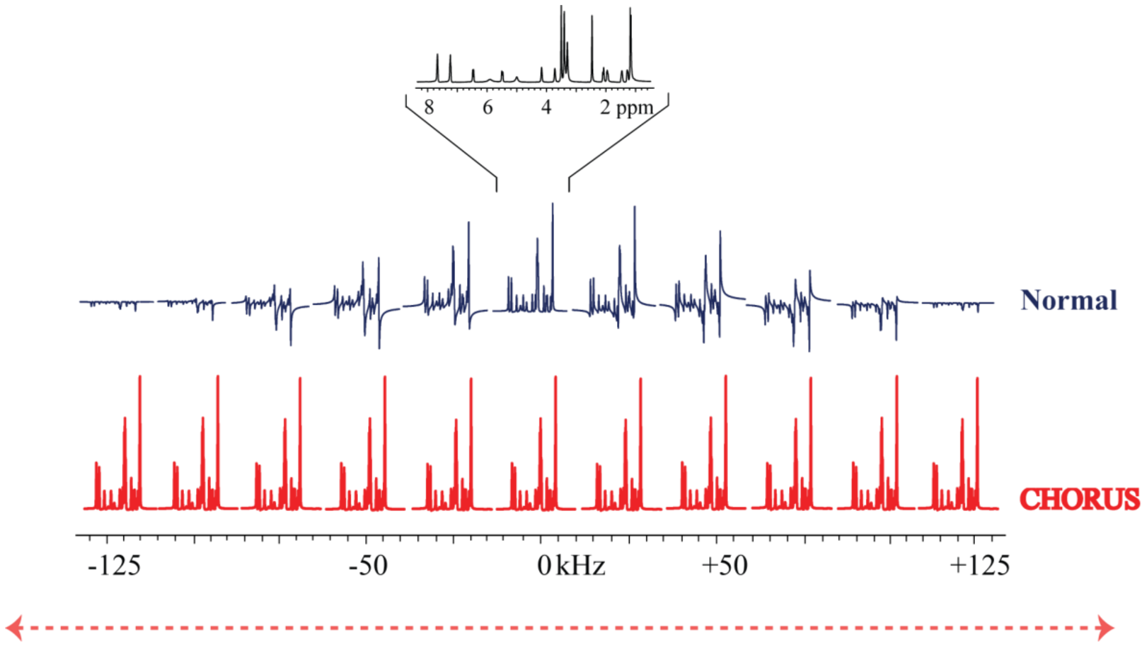

Figure 3.14: ^{1}H excitation profiles of rosuvastatin in DMSO-d_6, using hard 90° excitation (blue) and using CHORUS (red). The profiles are excited over a 250 kHz range in steps of 25 kHz as described in Section 3.1.1.

The next stage in the development of broadband excitation for qNMR is to investigate how robust the new sequence CHORUS is, and to what extent can it deliver quantitative integrals over the required bandwidths.

3.4. CHORUS and Quantification

3.4.1. Introduction

Of particular interest is the application of CHORUS to ^{19}F NMR. The existing method for ^{19}F quantification[13] uses simple 90° excitation. However, as stated in the introduction, limited radiofrequency pulse power means that it is not possible to achieve quantitative excitation of more than a fraction of the observed chemical shift range. At present, it is necessary to use different internal standards for different spectral regions, measuring each region separately. This method is not so easy due to complications of sample instability, insolubility of quantitation standards in the solvent used, and signal overlap between analyte and standard.[26] CHORUS has been developed to provide a more efficient quantification method, so that the constraints on standard choice are minimized and spectra can be analysed as a whole.

Before CHORUS can be validated for qNMR, it must first pass stringent testing for criteria of performance such as repeatability and robustness. The criterion for acceptability for these two indices of performance is ≤ 1% for repeatability of peak areas of drug substances to standard ratio.[15, 27]

Another area of performance that can be tested is linearity;[15] however, the performance of CHORUS should not differ from that of other NMR excitation methods, where for the concentration range of interest, the effect of sample concentration on RF amplitude and phase should be negligible. In addition, factors such as relaxation, digitisation and S/N ratio need to be considered; however, these effects on spectra should be relatively easily calculated, as for other NMR acquisition methods.[12, 27]

3.4.2. Two Measures of Performance

3.4.2.1. Experimental

Experimental data were acquired for both measures of performance using a sample of bicalutamide (65 mM) and 4-fluoroaniline (221 mM) in DMSO-d_6 (Figure 3.15), on a 500 MHz Bruker AVIII spectrometer, with a 5 mm BBO probe and QNP switch, at the University of Manchester. ^{1}H decoupled ^{19}F data were acquired with 16 scans over a spectral width (*sw*) of 234 ppm using a hard 90° pulse width of 12.4 µs. For CHORUS, the chirp pulses were generated using the same parameters as outlined in Section 3.3.3.1, to give RF amplitude pulse ratios (0.21 : 0.71 : 1).

The experimental data were processed by converting Bruker data to VnmrJ format, zero-filling to 524288 real points and using a time-domain weighting function corresponding to a 5 Hz Lorentzian. The phase for the first spectrum in each set was adjusted and integral resets set at 0.25 ppm either side of each peak, and automated polynomial baseline correction and integral determination were then carried out for all spectra. The data were analysed in Mathematica *v*9 by Professor G. A. Morris and J. E. Power.

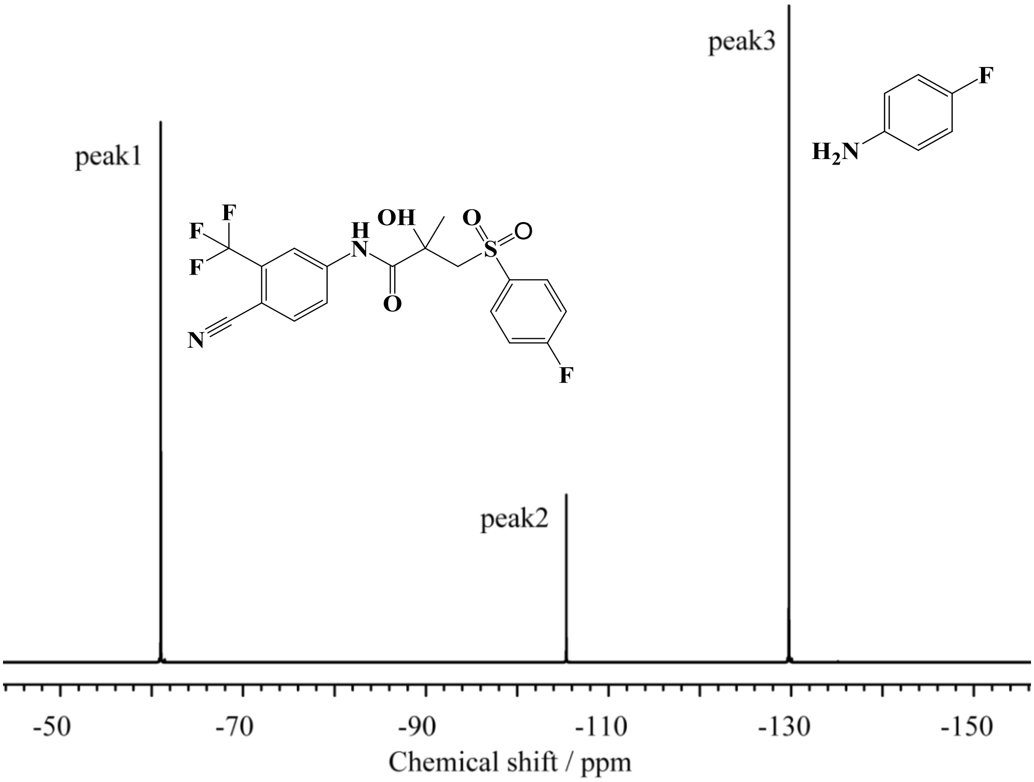

Figure 3.15: ^{1}H decoupled ^{19}F spectrum of a sample of bicalutamide (peaks 1 and 2, at −61.0 ppm and −105.4 ppm, respectively) and reference material 4-fluoroaniline (peak 3 at −129.8 ppm) in DMSO-d_6; the ^{19}F NMR spectrum was acquired using CHORUS and processed with a line broadening (*LB*) of 5 Hz.

The approximate S/N ratios of the three peaks using the hard pulse and CHORUS are shown in Table 3.1a; the theoretical relative integrals of the three peaks (1:2), (1:3) and (2:3), are shown in Table 3.1b.

Approximate S/N ratio

a)	**peak1 (−61.0 ppm)**	**peak2 (−105.4 ppm)**	**peak3 (−129.8 ppm)**
Hard pulse (−100 pm)	16900	5200	17200
CHORUS (−100 ppm)	17600	5400	19200

Theoretical relative integrals

b)	**peaks (1:2)**	**peaks (1:3)**	**peaks (2:3)**
Theoretical relative integral ratios	3.000	0.8817	0.2939

Table 3.1: a) Approximate S/N ratios of the three peaks of Figure 3.16. Spectra were acquired using CHORUS and a 90° pulse. b) Theoretical relative integrals of peaks (1:2), (1:3) and (2:3), as calculated from the mole ratios and the percentage composition by mass of the sample.

3.4.2.2. Repeatability

Repeatability of the method was investigated by comparing individual absolute integrals across 30 spectra of the same sample acquired consecutively. Acquisitions with CHORUS were interleaved with on-resonance hard pulse acquisitions, in order to monitor spectrometer drift, to give 60 acquisitions in total. The spectrometer operating frequency for both pulses was set at −100 ppm. The ratios of relative absolute integrals of peaks (1:2), (2:3) and (1:3) are summarized in Table 3.2a and 3.2b for hard pulse and for CHORUS excitation respectively, with means and relative standard deviations. Graphs of percentage deviations of absolute integrals for the three peaks are shown in Figures 3.16a and 3.16b, for hard pulse and CHORUS respectively. For both CHORUS and 90° excitation, repeatability of peak area ratios was in both cases more than an order of magnitude better than the target criterion of $\leq 1\%$.

Integral ratio summary

		peaks (1:2)	peaks (1:3)	peaks (2:3)
Theoretical relative integral ratios		3.000	0.8817	0.2939
a) Hard Pulse	Mean	2.947	0.8743	0.2966
	% RSD	0.072	0.027	0.072
b) CHORUS	Mean	3.022	0.8798	0.2911
	% RSD	0.076	0.028	0.078

Table 3.2: Means and relative standard deviations for absolute ratios of peak integrals (1:2), (2:3) and (1:3), in a test of repeatability. The data were acquired using interleaved CHORUS and hard pulse acquisitions with the spectrometer operating frequency set at −100 ppm. The theoretical relative integral ratios from Table 3.1 are included as a reference to which experimental data can be compared.

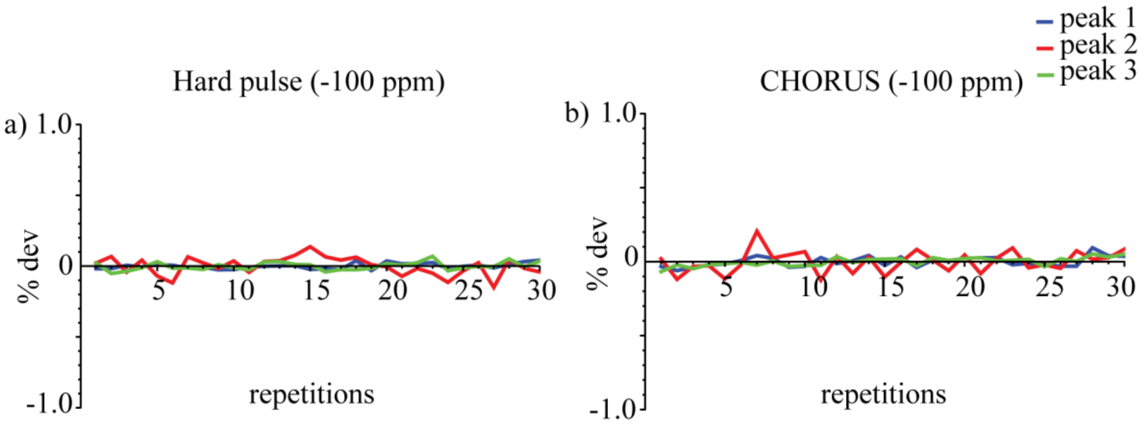

Figure 3.16: a) and b) Percentage deviations of absolute integrals of peaks 1, 2 and 3 for hard pulse and CHORUS, with spectrometer operating frequencies set at −100 ppm.

3.4.2.3. Robustness with Respect to Offset

For quantitative use, CHORUS must show uniform excitation with constant amplitude and constant (or at least linearly varying) phase over the full spectral width. In order to test this measure of performance, CHORUS measurements were, as before, interleaved with measurements using a hard pulse on-resonance (O1p at −100 ppm). For CHORUS, the spectrometer operating frequency (O1p) of −100 ppm was varied from −20 ppm to −165 ppm, in steps of 5 ppm, to give 30 experiments covering an offset range of 145 ppm (68 kHz), with three repetitions. Because the frequencies of the received signals depend on O1p, relative signal amplitudes are affected by the characteristics of the receiver. While such effects are much smaller with modern digital signal processing than they were with the analogue filters used on older spectrometers, they are still significant. This small fixed error shows a quadratic dependence on frequency, for which the CHORUS raw data can be corrected straightforwardly by dividing experimental data by measured filter characteristics (see relevant Section 3.4.2.4). Data for the relative absolute integral ratios of peaks (1:2), (2:3) and (1:3) are summarized in Table 3.3, for the three repeats. For CHORUS and hard pulse, the raw data are shown a) before correction, and b) after correction for the receiver characteristics.

Figures 3.17a, 3.17b and 3.17c show the percentage deviations of absolute integrals for the three peaks as a function of offset, where 3.17a shows the CHORUS raw data, 3.17b the CHORUS raw data after receiver correction, and 3.17c the CHORUS raw data receiver-corrected and after correction for systematic drift using the hard pulse data; the data are normalized by plotting CHORUS to the reference hard pulse data at a given frequency. For all data sets, repeatability of peak area ratios is significantly better than the criterion of ≤ 1%, and similar to the reproducibility data of Table 3.2, implying that any integral variation with respect to offset is around or below the threshold of detection in these experiments.

3.4.2.3.1. Statistical Data for Both Measures of Performance

The average integral ratios for CHORUS (Tables 3.2 and 3.3) show significant differences from the theoretical values (Table 3.1b). This is attributable partly to T_2 relaxation (peaks 1, 2 and 3 have approximate T_2 values of 680 ms, 470 ms and 2.9 s respectively) and partly to low-level impurities present in the sample.

The average integral ratios for hard pulse excitation also shows significant deviations from the ideal; however, this is to be expected because of off-resonance effects. The corrected data for the receiver characteristics are given in Table 3.3.

Integral ratio summary

For three repeats	peaks (1:2)	peaks (1:3)	peaks (2:3)
Theoretical relative integral ratios	3.000	0.8817	0.2939
(a) Hard Pulse			
#1 Mean	2.951	0.8750	0.2966
#2 Mean	2.947	0.8744	0.2967
#3 Mean	2.947	0.8743	0.2966
#1 %RSD	0.051	0.030	0.040
#2 %RSD	0.051	0.024	0.054
#3 %RSD	0.066	0.022	0.060
(b) Hard Pulse (receiver-corrected)			
#1 Mean	2.990	0.8821	0.2950
#2 Mean	2.987	0.8815	0.2951
#3 Mean	2.987	0.8813	0.2950
#1 %RSD	0.051	0.030	0.040
#2 %RSD	0.051	0.024	0.054
#3 %RSD	0.066	0.021	0.060
(a) CHORUS (raw data)			
#1 Mean	3.024	0.8814	0.2914
#2 Mean	3.025	0.8812	0.2913
#3 Mean	3.024	0.8810	0.2913
#1 %RSD	0.14	0.22	0.12
#2 %RSD	0.13	0.23	0.14
#3 %RSD	0.15	0.23	0.12
(b) CHORUS (receiver-corrected)			
#1 Mean	3.024	0.8805	0.2912
#2 Mean	3.024	0.8804	0.2911
#3 Mean	3.023	0.8801	0.2911
#1 %RSD	0.070	0.024	0.065
#2 %RSD	0.080	0.028	0.081
#3 %RSD	0.071	0.037	0.075

Table 3.3: For three repeats, the means and relative standard deviations for absolute ratios of peak integrals (1:2), (2:3) and (1:3) in a test of robustness. The data were acquired using interleaved CHORUS and hard pulse acquisitions, with the latter on resonance (O1p at −100 ppm). The theoretical relative integral ratios from Table 3.1 are included.

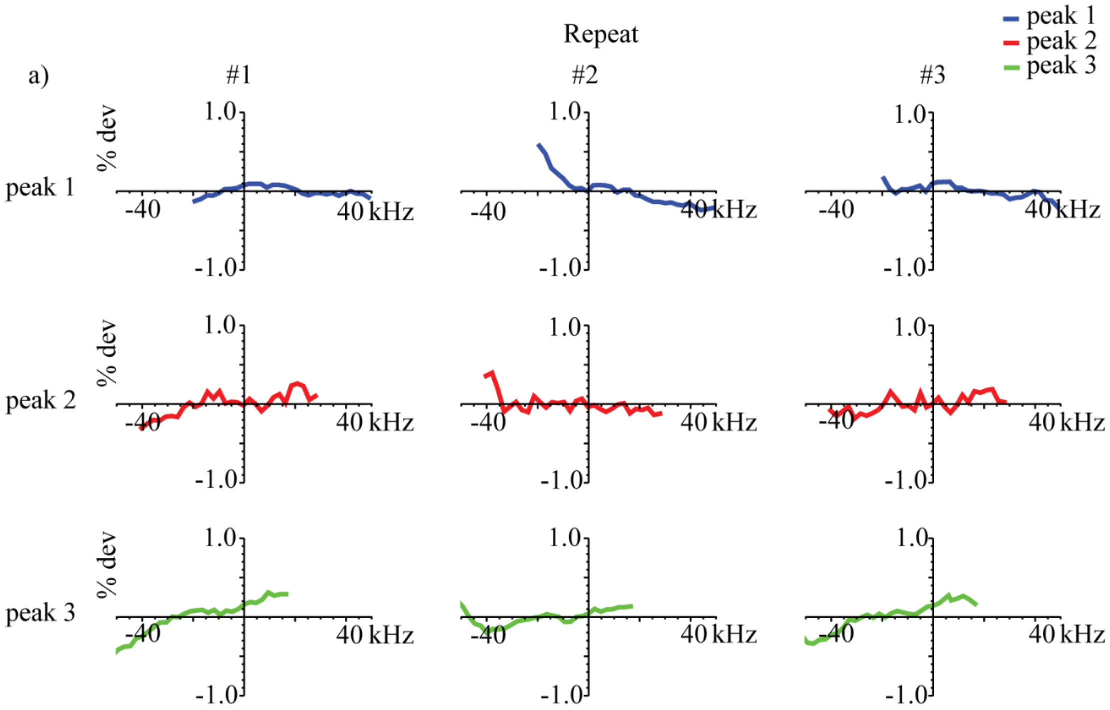
a)
Repeat
#1
#2
#3
peak 1
peak 2
peak 3
% dev
1.0
-1.0
-40
40 kHz

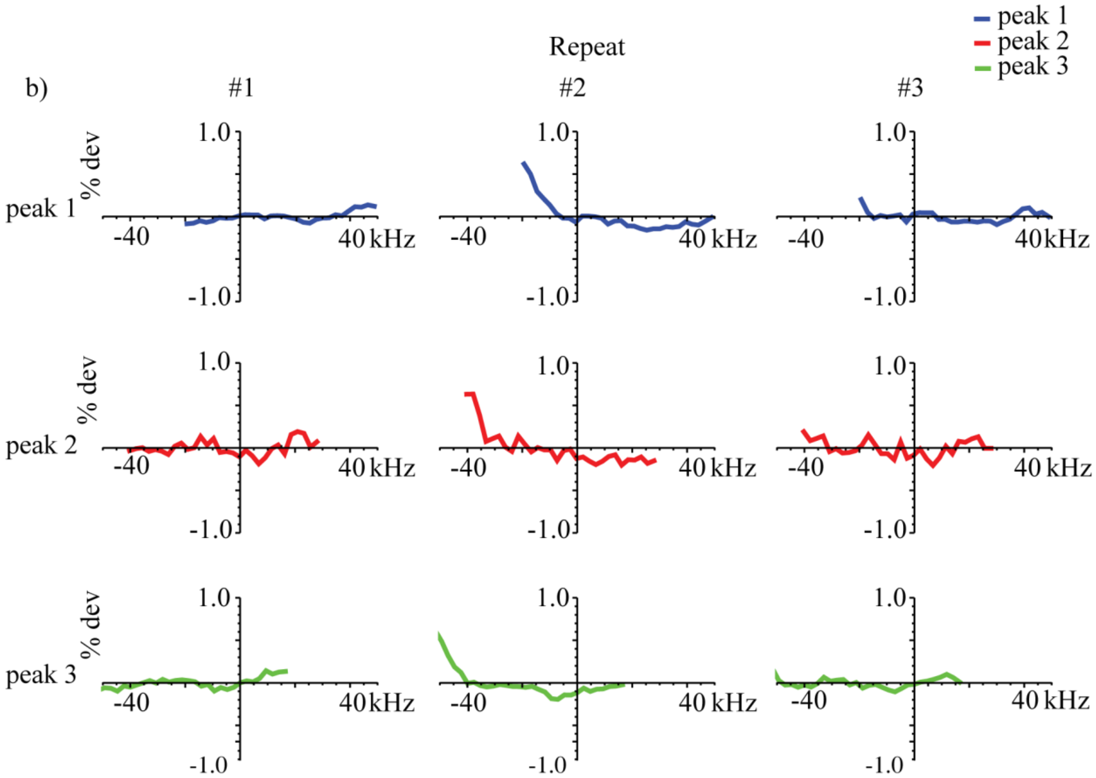
b)
Repeat
#1
#2
#3
peak 1
peak 2
peak 3
% dev
1.0
-1.0
-40
40 kHz

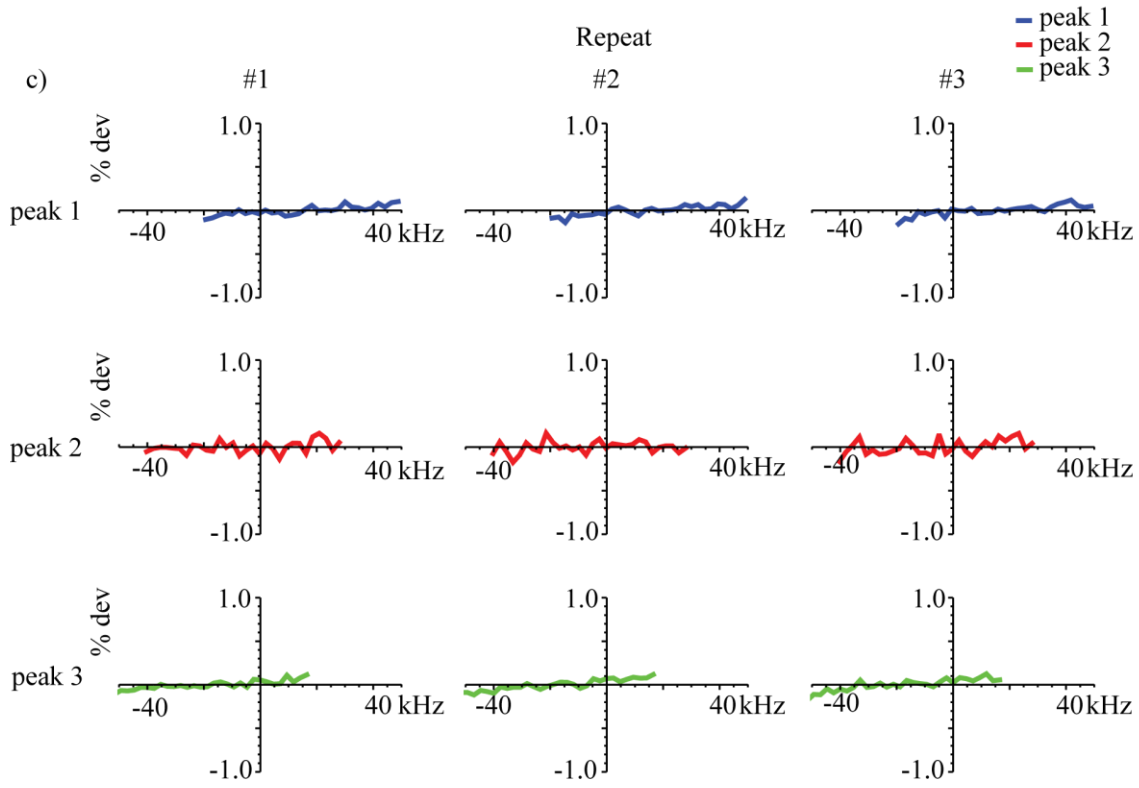

Figure 3.17: a), b) and c) Percentage deviations of absolute integrals of the three peaks, as a function of offset, for three repetitions, where (a) is the CHORUS raw data, (b) the CHORUS data receiver-corrected and (c) the CHORUS data receiver-corrected and after correction for systematic drift by normalisation to the on-resonance hard pulse data.

3.4.2.4. Effects of Receiver Signal Filtration on Signal Amplitude

To show the effects of the analogue and digital receiver filters on signal amplitude, signal profiles were constructed from an experiment using a doped sample of C_6F_6 in DMSO-d_6, on a Bruker 500 MHz system using a 90° pulse width of 12.38 μs and CYCLOPS.[69] A 90° pulse was applied on resonance to excite a constant signal, while the receiver frequency was varied in 1 kHz steps over the spectral width of 300 kHz. To allow correction for any spectrometer drift, measurements with receiver off and on resonance were interleaved. The receiver profile (red) shows an approximately 3% reduction close to the edges of the spectral width (± 150 kHz), while the interleaved on-resonance data (blue) show negligible variation in signal (Figure 3.18a). Fitting the receiver characteristic to a quadratic function (Figure 3.18b) allowed the data for robustness with respect to offset to be corrected for this source of systematic error.

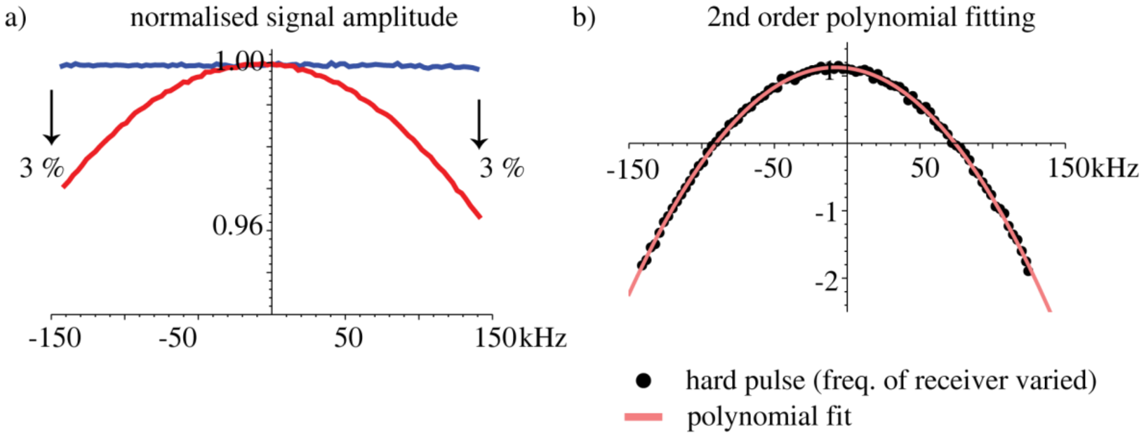

Figure 3.18: Signal profiles constructed from a receiver frequency-arrayed experiment in which alternate 90° pulse acquisitions were performed, with transmitter on resonance (red) and receiver offset varied, and a reference measurement (blue) with both transmitter and receiver on resonance; b) quadratic fitting (pink) of the signal amplitude variation. The experimental data (Figure 3.18b, black dots) is truncated just within the start of the digital cut-off at the edges of the frequency range.

3.4.2.5. CHORUS and *J*-Modulation

Swept-frequency pulses are relatively long, in the order of milliseconds. For CHORUS, which has three chirp elements, for a 300 kHz bandwidth and with a unit pulse duration $\tau = 1$ ms, the total pulse sequence duration is 6 ms (Figure 3.10c). Due to this lengthy duration, the pulse sequence can suffer from *J*-modulation if large homonuclear couplings are present.

To demonstrate the effects of *J*-modulation when using CHORUS, a sample of sodium perfluorooctanoate (NaPFO) in DMSO-d_6 was used, on a Bruker 500 MHz system with 8 scans, over a spectral width (*sw*) of 121 ppm and using a 90° pulse width of 12 µs.

For a signal on resonance, the ^{19}F spectrum showed up to 20 % reduction in integral for CHORUS (red) in comparison to a hard pulse (blue) (Figure 3.19). The surfactant has a relatively long T_2 of 0.4 s, so relaxation is not to blame; rather, the 6 ms duration of CHORUS is long enough for significant evolution under the ^{19}F-^{19}F couplings in the PFO anion. This causes distortion of multiplet shapes and hence reduces net signal integrals.

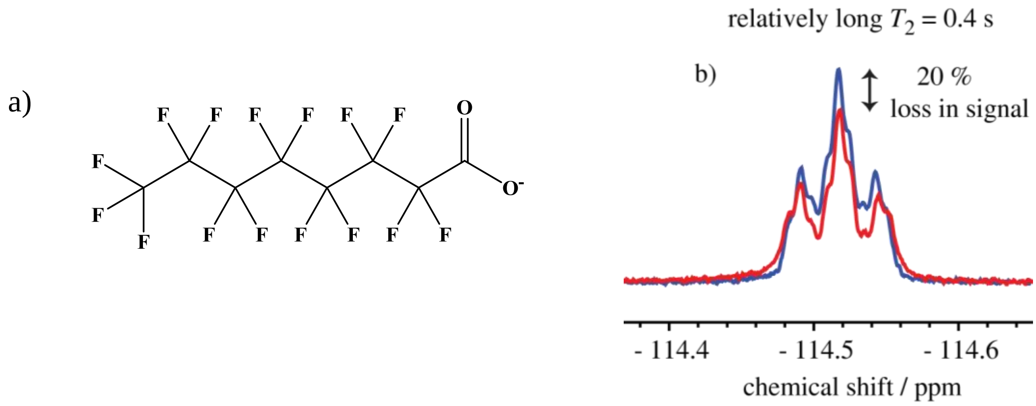

Figure 3.19: Structure of surfactant PFO anion, and b) ^{19}F spectrum of the alpha CF_2 NaPFO signal on resonance for CHORUS (red) and for a 90° hard pulse (blue). For CHORUS, the signal shows approximately 20% loss in integral compared to the hard pulse, due to *J*-modulation.

3.4.3. Implementation of CHORUS at AstraZeneca

3.4.3.1. Introduction

CHORUS has been tested on two spectrometers at AstraZeneca (AZ): 400 MHz Bruker AVIII (5 mm BBFO + probe) and 500 MHz Bruker AVIII (5 mm QCI cryoprobe). A preliminary investigation was performed on the former, for two measures of performance, repeatability over time and robustness with respect to offset. The analysis was performed to verify the accuracy of CHORUS for ^{19}F quantification, prior to validation using an AZ protocol.

3.4.3.1.1. Experimental

Experimental data were acquired for both measures using a sealed sample of SF_6 (peak 1 at 59 ppm), bicalutamide (peaks 2 and 3 at −61.8 ppm and −106.2 ppm, respectively) and C_6F_6 (peak 4 at −163.3 ppm) in DMSO-d_6 (Figure 3.20). The data were acquired with 16 scans with a spectral width (*sw*) of 498 ppm using a 90° pulse width of 11.8 µs. For CHORUS, the chirp pulses were generated with the parameters outlined in Section 3.3.3.1.

The experimental data were processed by converting Bruker data to VnmrJ format as in Section 3.4.2.1; however, for this experiment the integral resets were set at 0.4 ppm either side of each peak instead of 0.25 ppm, due to the close proximity of ^{13}C satellites. The data were analysed in Mathematica *v*9 by Professor G. A. Morris. The approximate S/N ratios of the four peaks using the hard pulse and CHORUS are shown in Table 3.4; these are significantly lower than those of Table 3.1a.

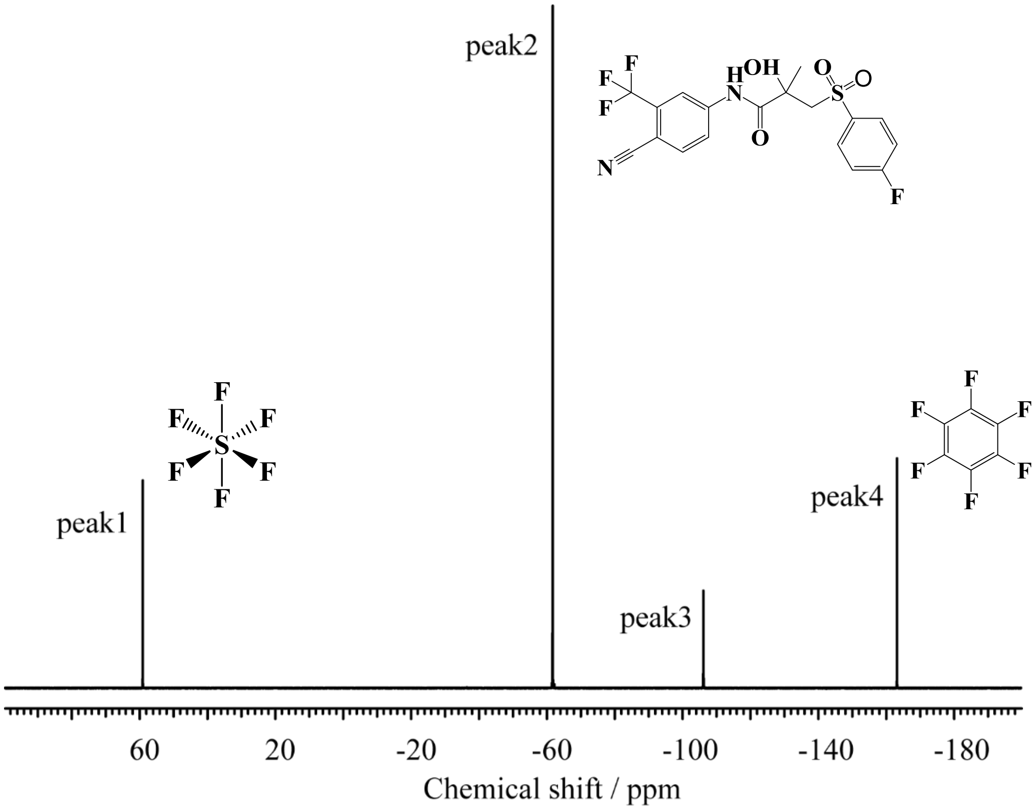

Figure 3.20: ^{19}F NMR spectrum of a sample of SF_6 (peak 1 at 59 ppm), bicalutamide (peaks 2 and 3 at −61.8 ppm and −106.2 ppm, respectively) and C_6F_6 (peak 4 at −163.3 ppm) in DMSO-d_6. The spectrum was acquired using CHORUS and processed with a line broadening (*LB*) of 5 Hz.

Approximate S/N ratio

	peak1 (59 ppm)	**peak2 (−61.8 ppm)**	**peak3 (−106.2 ppm)**	**peak4 (−163.3 ppm)**
Hard pulse	670	3000	400	370
CHORUS	800	3000	400	900

Table 3.4: Approximate S/N ratios of the four peaks of Figure 3.20 using a hard pulse and CHORUS.

3.4.3.2. Repeatability

Repeatability of the method was investigated as in Section 3.4.2.2; however, here the experiments were across 25 spectra of the same sample acquired consecutively to give 50 acquisitions in total, with CHORUS interleaved with on-resonance hard pulse acquisitions. The spectrometer operating frequency (O1p) for both pulses was set at −50 ppm.

The ratios of relative absolute integrals of peaks (2:3), (2:4) and (3:4) are summarized in Tables 3.5a and 3.5b for the hard pulse and CHORUS respectively, with means and relative standard deviations. Peak 1 was not used in the relative ratio analysis, since the material is volatile (SF_6), which may vary in concentration. The graphs of percentage deviations of absolute integrals for the 4 peaks are shown in Figures 3.21a and 3.21b, for the hard pulse and CHORUS respectively.

For both CHORUS and 90° excitation, repeatability of peak area ratios was, in almost all cases, 50% or greater below the target criterion of ≤ 1%.

Integral ratio summary

		peaks (2:3)	**peaks (2:4)**	**peaks (3:4)**
a) Hard Pulse	Mean	3.080	4.336	1.408
	% RSD	0.337	0.548	0.461
b) CHORUS	Mean	3.009	3.417	1.136
	% RSD	0.261	0.478	0.583

Table 3.5: Means and relative standard deviations for absolute ratios of peak integrals (2:3), (2:4) and (3:4), in a test of repeatability; peak 1, volatile (SF_6), has not been analysed. The data were acquired using interleaved CHORUS and hard pulse acquisitions with the spectrometer operating frequency set at −50 ppm.

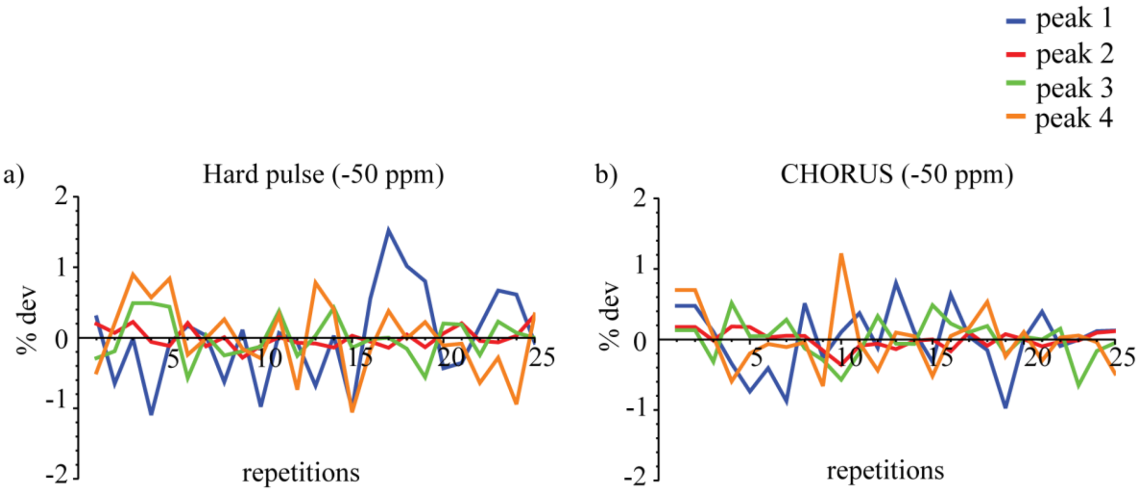

Figure 3.21: a) and b) Percentage deviations of absolute integrals of peaks 1, 2, 3 and 4 for hard pulse and CHORUS, with spectrometer operating frequency (O1p) set at −50 ppm.

3.4.3.3. Robustness with Respect to Offset

Robustness of the method was investigated as in Section 3.4.2.3. For a 400 MHz system with a magnetic field of 9.39 T and a fluorine resonance frequency of 376.5 MHz, it was more convenient to calculate the variation of the spectrometer operating frequency (O1p) (at −50 ppm) in Hz rather than ppm to give integer numbers. O1p was, therefore, varied from 28224 Hz (74.96 ppm) to −47040 Hz (−124.94 ppm), in steps of 4704 Hz (12.49 ppm), to give 17 experiments covering an offset range of 18.816 kHz (49.98 ppm), with 1 repetition.

The ratios of relative absolute integral ratios of peaks (2:3), (2:4) and (3:4) are summarized in Table 3.6a and 3.6b, for the hard pulse and CHORUS respectively, with means and relative standard deviations. The graphs of percentage deviations of absolute integrals for the 4 peaks are shown in Figures 3.22a and 3.22b, for the hard pulse and CHORUS respectively. For CHORUS the data are *not* shown as a function of offset, as in Section 3.4.2.3, since correction for the 400 MHz receiver characteristics and systematic drift was not performed.

For CHORUS, repeatability of peak area ratios was in all cases 60% or greater below the target criterion (≤ 1%), slightly better than the hard pulse results; however, as shown in Figure 3.22b, CHORUS is showing some drift.

Integral ratio summary

		peaks (2:3)	**peaks (2:4)**	**peaks (3:4)**
a) Hard Pulse	Mean	3.086	4.375	1.418
	% RSD	0.311	0.601	0.700
b) CHORUS	Mean	3.015	3.416	1.133
	% RSD	0.421	0.286	0.390

Table 3.6: The means and relative standard deviations for absolute ratios of peak integrals (2:3), (2:4) and (3:4), in a test of robustness. The data were acquired using interleaved CHORUS and hard pulse acquisitions, with the latter on resonance (O1p at −50 ppm).

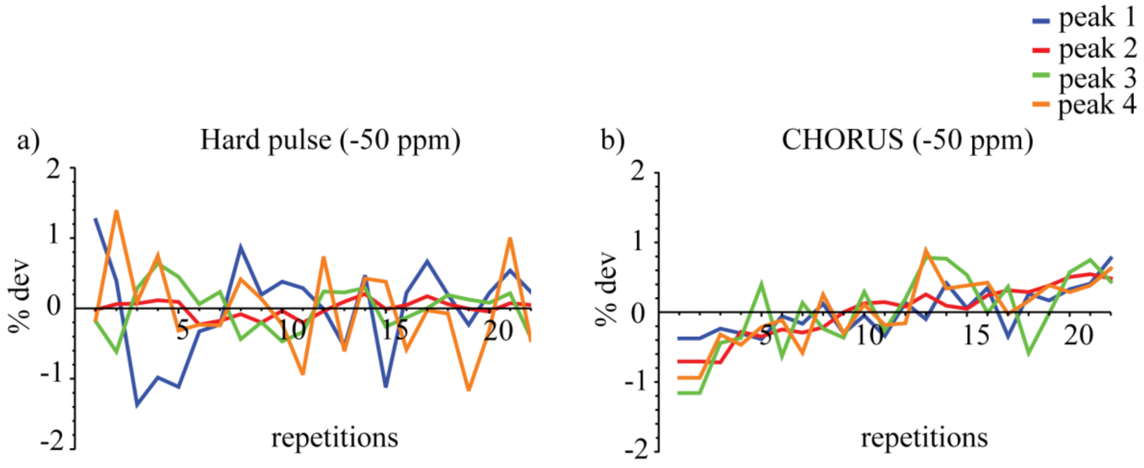

Figure 3.22: a) and b) Percentage deviations of absolute integrals of peaks 1, 2, 3 and 4 for hard pulse and CHORUS, with spectrometer operating frequencies (O1p) set at −50 ppm.

3.4.3.4. Discussion

The relative integral ratio analysis, for repeatability and robustness, of the AZ data at 400 MHz, are not as good as the results obtained at 500 MHz (University of

Manchester) (Sections 3.4.2.2 and 3.4.2.3). However, the CHORUS data (Tables 3.5b and 3.6b) are comparable to the 90° excitation data (Tables 3.5a and 3.6a) and are well within the criterion for acceptability, such that validation can be performed with confidence.

The graphs for repeatability (Figures 3.21a, 3.21b and 3.22a) show similar variation, with most error attributed to random noise; however, for robustness (CHORUS, Figure 3.22b) other factors also must be considered, such as the effects of the receiver characteristics on signal amplitude and spectrometer-related problems, such as systematic drift.

The main problem with the data is the lack of sensitivity of the experiment, as shown by the poor S/N ratio; for the weakest signal at −106 ppm, the S/N ratio is poorer by an approximate factor of 13 than the equivalent signal of Figure 3.15 (Section 3.4). The reasons for the poor S/N ratio are as follows. The sample of bicalutamide was prepared with low concentration (~ 15 mM) to give appropriate peak height compared to the reference material SF_6 (~ 2.6 mM), with two reference materials, SF_6 and C_6F_6, chosen to cover a wide chemical shift range of 221 ppm (83 kHz). In addition, the data were acquired at lower frequency (400 MHz), and not $^{19}F\{^1H\}$ decoupled. The sample was initially designed not for quantification but to illustrate qualitatively the signal attenuation off-resonance for 90° excitation in comparison to CHORUS, as shown in Figure 2 of Power *et al*[26] and in Figure 3.23 below.

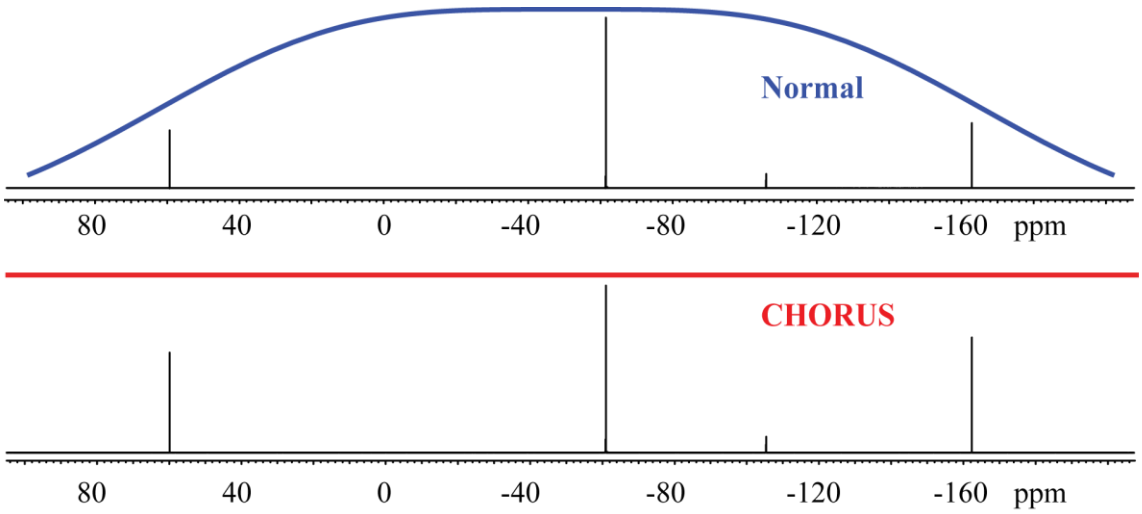

Figure 3.23: 470 MHz ^{19}F NMR spectra of a sample containing bicalutamide, SF_6 and C_6F_6 acquired using 90° excitation and CHORUS, with simulated excitation profiles in blue and red respectively (performed on the 500 MHz system at the University of Manchester). For 90° excitation (simulation and experiment), a linearly frequency-dependent phase correction was applied.

3.4.3.5. CHORUS on a Cryoprobe System

The second spectrometer to be tested at AZ was the 500 MHz Bruker AVIII (5 mm QCI cryoprobe) system.

3.4.3.5.1. Introduction: Cryogenically Cooled Probes

NMR generally has low sensitivity (Section 2.6.2); therefore, in order to maximize the S/N ratio the amount of noise collected during acquisition needs to be minimized. The main source of noise in the spectrum comes from detection of the signal in the coil attached to the probe, which generates thermal noise due to thermal motion of its electrons. The development of cryogenically cooled probes can enhance sensitivity by reducing the temperature of the RF detection coils and the preamplifier, thereby increasing the S/N ratio three to fourfold.[70] Such an improvement in sensitivity allows sample concentrations to be minimized, e.g. when materials are expensive or when solubility is poor; in addition, experiment times can be greatly reduced, as repetition for time averaging to improve SNR is not as important. For pharmaceutical companies such as AZ, using CHORUS would be advantageous; however, preliminary tests showed some issues that first need to be resolved.

3.4.3.5.2. Lineshape distortion

Experimental data were acquired for CHORUS using a doped sample of SF_6, NaPFO and C_6F_6 in DMSO-d_6. NaPFO, though susceptible to *J*-modulation (Section 3.4.2.5), has seven fluorine environments, which potentially can illustrate the good performance of CHORUS with respect to uniformity of phase across a wide spectral width; the sample was doped to increase the relaxation rate. Experiments were performed using a spectral width (*sw*) of 295 ppm (~ 139 kHz) using a 90° hard pulse width of 11.4 µs with 4 scans and EXORCYCLE. The chirp pulse parameters were as detailed in Section 3.3.3.1.

Dips in the lineshape on all signals in the ^{19}F spectrum were observed to different extents (Figure 3.24). Possible issues such as radiation damping [71] were ruled out when the sample was diluted by a factor of six without effect. A possible explanation is a brief warming up of the cryoprobe RF coil, since the triple chirp sequence deposits much greater RF energy in the coil than a simple 90° pulse. This may cause two effects: the offset compensation might degrade slightly, generating phase errors, since the RF field would gradually droop in amplitude over the course of the three pulses; and, due to warming of the coil, the probe *Q* and/or tuning would degrade causing the phase and amplitude of the FID over the first tens of ms to change. As the coil returns to normal operating temperature, the FID amplitude would increase during the early part of the FID; this might be the cause of the dips in the lineshape. To investigate this further, the following two experiments were performed.

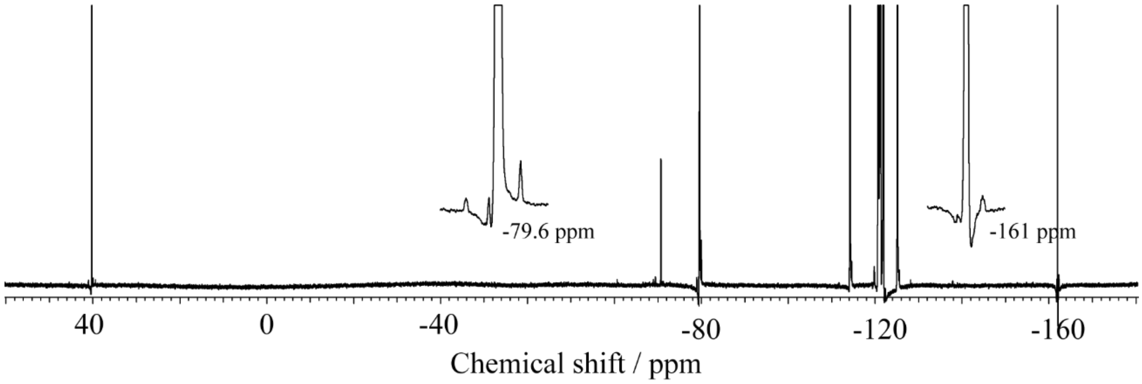

Figure 3.24: ^{19}F spectrum of a doped sample of SF_6, NaPFO and C_6F_6 in DMSO-d_6 using CHORUS. Dips in the lineshape of the signals are observable to different extents; two regions are expanded (−79.6 ppm (NaPFO) and −161 ppm (C_6F_6)) to show the distortions more clearly. The data were processed with a line broadening (*LB*) of 5 Hz and with high vertical scale.

3.4.3.5.3. Rotary Echo Experiment

This experiment was designed to mimic the cryoprobe RF coil heating caused by CHORUS, to see whether this was to blame. The sequence consisted of two rectangular pulses, 180° different in phase, followed by a purge gradient pulse and a 90° read pulse. The shaped pulses were of 1 ms duration with a nominal RF amplitude of −8 dB to match the maximum RF amplitude of the last 180° chirp pulse in the CHORUS sequence; the experiment was also repeated using a read pulse of 20° flip angle. No dips in lineshape were seen with 90° or with 20° read pulses; an experiment that more closely matches the temporal pattern of heat distribution may be more informative.

3.4.3.5.4. Alteration of the Number of Dummy Scans

Increasing the number of dummy scans to four and eight significantly reduced the lineshape distortions; this does suggest that the problem is heating-related, with three main areas of the hardware, the probe coil, preamplifier and transmit/receive switch, being vulnerable to disturbances due to heating effects.

3.4.3.5.5. Summary

The problem of CHORUS on the AZ 500 MHz Bruker AVIII (5 mm QCI cryoprobe) system needs further investigation. There are various systems at the University of Manchester which use cryogenically cooled probes. It would be most advantageous to try CHORUS on one or more of these systems, to see if the problems of lineshape distortion can be reproduced. Further to this, and depending on the outcome, the AZ system can be examined for possible hardware-related problems.

3.4.4. CHORUS and Areas of Further Development

The CHORUS element is an integral part of the new broadband DOSY sequence, CHORUS Oneshot, as described in the following Chapter 4. The same logic used in this sequence can be applied to other 2D sequences such as NOESY and INADEQUATE to make them broadband.

Chapter 4

Very Broadband DOSY Diffusion-Ordered NMR Spectroscopy: ^{19}F DOSY

4. Very Broadband DOSY Diffusion-Ordered NMR Spectroscopy: ^{19}F DOSY

4.1. Introduction

Diffusion-ordered spectroscopy (DOSY), a powerful analytical tool for mixture analysis, exploits the fact that the rate of diffusion of molecules in solution is dependent on molecular properties such as size and shape. 2D DOSY correlates chemical shift with diffusion coefficient such that the NMR signals are dispersed according to the diffusion coefficients of the individual species (Section 2.10.1).[72-74]

^{1}H, with its high sensitivity, is the most commonly used nucleus for DOSY. However, the narrow chemical shift range (0-10 ppm) and large number of hydrogen atoms in most molecules, mean that resolution is poor, with overlapping signals a frequent occurrence, compromising accuracy of diffusion coefficients and obscuring impurities; an example of such a spectrum is the ^{1}H DOSY of Sample 2, Figure 4.9 (Section 4.3.2.2).

To reduce signal overlap, many DOSY experiments have been designed, e.g. pure shift[75, 76] or multidimensional[77-79] methods. For heteronuclear experiments, ^{13}C[80-82] is utilized, which due to a much wider chemical shift range (0-200 ppm), greatly improves resolution; albeit with its low abundance of 1.1%, at very high cost in signal-to-noise ratio.

As commented on in the introduction to Chapter 3, ^{19}F is of particular interest to the chemist, and is particularly suited to DOSY. The ^{19}F chemical shift shows high sensitivity to its local electronic environment, giving a very wide shift range (± 300 ppm). This combined with the smaller number of fluorine atoms in most drugs, offers exceptional resolution in the chemical shift dimension; therefore, in comparison to ^{1}H NMR, signal overlap is much rarer. With respect to sensitivity, it is comparable to ^{1}H

NMR; ^{19}F has high abundance (100%) and high gyromagnetic ratio γ, to give excellent signal-to-noise ratio, while the high γ gives efficient diffusion encoding, as dictated by the Stejskal-Tanner Equation 2.59 (Section 2.10).

However, ^{19}F with its wide shift range, though well suited to DOSY, suffers from resonance-offset effects, as explained in Sections 3.1.1, 3.1.2 and 3.1.3, and existing sequences can only excite a fraction of the ^{19}F chemical shift range at any one time.

Here a new broadband DOSY sequence is developed, extending the frequency range by almost an order of magnitude using ultra-broadband swept-frequency “chirp” pulses. The resultant CHORUS Oneshot pulse sequence allows the full ^{19}F shift range at 470 MHz to be covered in a single acquisition, to give uniform, constant-phase excitation and refocusing at negligible cost in sensitivity.

4.2. Development of CHORUS Oneshot

4.2.1. Introduction

To excite very wide frequency ranges is challenging, due to pulse imperfections such as off-resonance effects (Sections 3.1.1, 3.1.2 and 3.1.3). These effects in DOSY pulse sequences could be dealt with by the use of composite pulse methods (Section 3.2), but at present the bandwidths achievable fall well below those sought here.[16, 17, 59-62]

Linear swept-frequency “chirp” pulses (Section 3.2.5) used in this development allow full signal amplitude to be excited far off-resonance due to rapid “chirping” of the transmitter frequency during the pulse; however, large phase errors are introduced. These are further compounded for DOSY, since the pulse sequence contains a series of spin echoes.[23]

4.2.2. Stages of Development

The Oneshot pulse sequence[28] (Figure 4.1) is widely used for routine DOSY applications. The task of converting this sequence into one suitable for measuring very wide spectra can be divided into two parts, as shown in Figure 4.1: generation of spatially-encoded *z*-magnetization (diffusion encoding), carried out by the first three radiofrequency pulses; and the conversion of that *z*-magnetization into refocused transverse magnetization for measurement (diffusion decoding), carried out by the remaining two pulses.

At each stage of development, the experimental data (dots) were compared to simulations (lines) generated in Mathematica *v*.9 using compiled analytical solutions of the Bloch equations. The excitation profiles of Figures 4.2b, 4.3b and 4.5 were constructed from experiments in which the frequency of the refocusing, or the encoding, was varied in equal steps, but the receiver was kept on resonance to eliminate any bias caused by the receiver characteristics.

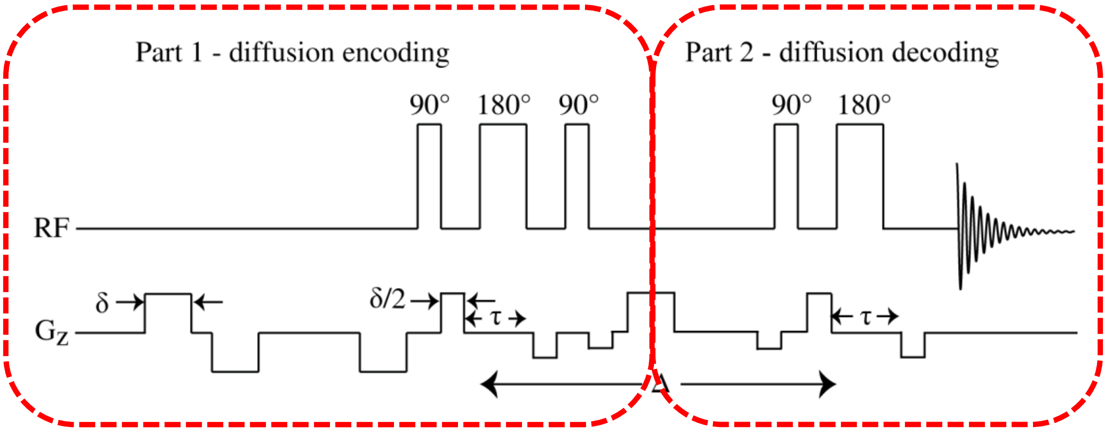

Figure 4.1: The two parts of the Oneshot pulse sequence, diffusion encoding and diffusion decoding.

4.2.2.1. Part 1 - Broadband Diffusion Encoding

4.2.2.1.1. Broadband Refocusing

The first hard 180° pulse of Oneshot was replaced by an adiabatic composite chirp $180^o180^o180^o$ sequence (Figure 4.2a). For refocusing of transverse magnetization, a single adiabatic 180° chirp introduces large phase errors; however, the three-pulse sequence is self-refocusing and without phase distortion.[61] It can be shown that for complete refocusing of spins, the composite pulse must have an odd number of adiabatic full passage (AFP) pulses; also, the parameter R (Equation 4.1), needs to be in the ratio 1:2:1 for the three pulses:[61]

$$R = \mathrm{bw} \times T_\mathrm{p} \qquad 4.1$$

where bw is the chirp range (Hz) and T_p is the pulse duration (s); these conditions are met for sequence Figure 4.2a.

4.2.2.1.1.1. Experimental

To test the performance of sequence Figure 4.2a, experimental data were acquired and an excitation profile constructed from ^{1}H measurements (Figure 4.2b). The excitation 90° hard pulse (pw = 8.1 μs) was kept on resonance, while the frequency of the refocusing was varied in steps of 1 kHz over a 1 MHz range using a 4-step phase cycle, EXORCYCLE. The data were acquired non-spinning on a Bruker 500 MHz system using a doped water sample.

The chirp pulses were generated in Bruker software in the Bruker format, with a sweep width (ΔF) of 1 MHz, 20% smoothing (which was reduce to 5% smoothing further in to the development of the sequence (Sections 3.2.5 and 4.2.2.3)), Q factor of 5 and RF amplitude $\left(\gamma B_1{}^{180}/2\pi\right)$ of 19947 Hz for each of the chirp elements. The total duration of the sequence, for a unit pulse duration τ = 1 ms, was 4 ms, using 3000 points, with the points for the three 180° chirp elements distributed in the ratio 1 : 2 : 1.

4.2.2.1.1.2. Results and Discussion

Figure 4.2b shows the superimposed experimental (red dots) and simulated (green line) result using the sequence of Figure 4.2a. Uniform, constant phase broadband refocusing is achieved over almost 1 MHz with no undue B_1 sensitivity and hence with no loss in sensitivity; this is due to complete phase refocusing, in accordance with the theory.

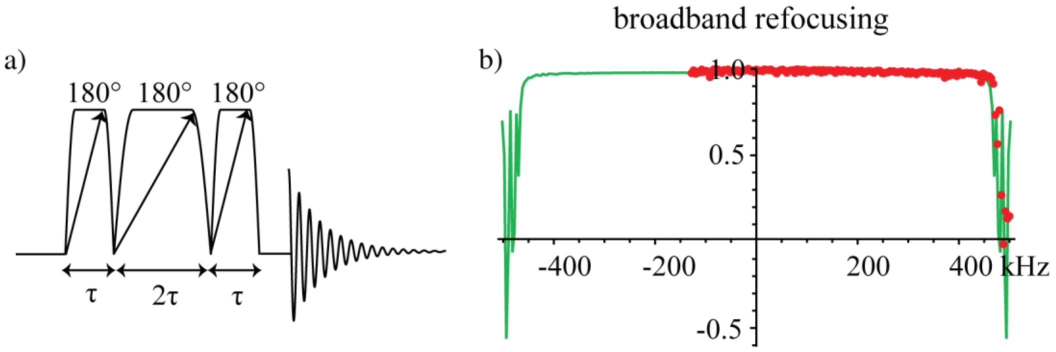

Figure 4.2: a) Adiabatic composite chirp sequence; b) experimental results (dots) using a doped water sample, with simulations (green line), for the chirp pulse sequence of Figure 4.2a. A 1 MHz offset range is covered using ~ 20 kHz RF amplitude for each pulse element, with τ = 1 ms. The experimental data are truncated at – 130 kHz because of the limited coherence range of the spectrometer synthesiser used.

4.2.2.1.2. Broadband Spatially-Encoded *z*-Magnetization

To obtain broadband diffusion encoding, the first and second 90° hard pulses were replaced with 90° chirp pulses, with the sweep direction of the second 90° pulse reversed. As discussed and illustrated in Section 3.3.1 (Figure 3.7), the frequency-modulated 90° chirp is not self-refocusing, with the excitation produced varying very rapidly in a nonlinear fashion with resonance offset, causing phase dispersion of the signals. However, the counter-sweeping 90° chirp pulses exhibit complementary frequency-dependent phase shifts, so when combined with the adiabatic composite chirp sequence (Figure 4.3a), ensure uniform constant-phase encoding over a 250 kHz frequency range (Figure 4.3b).

4.2.2.1.2.1. Experimental

To test the performance of sequence Figure 4.3a, experimental data were acquired using chirp pulses, and the same sequence replaced with conventional hard pulses (90°,180°,90°). Excitation profiles were constructed from ^{1}H measurements (Figure 4.3b), where the frequency of the excitation varied in steps of 1 kHz over a 300 kHz range with a 4-step phase cycle, EXORCYCLE. The data were acquired non-spinning on a Bruker 500 MHz system using a doped water sample and a 90° pulse width of 8.1 μs.

The chirp pulses were generated in Bruker software in the Bruker format, with a sweep width (ΔF) of $(+)$ 300 kHz for each chirp pulse, but with the 2$^{\text{nd}}$ 90° chirp element having a reverse sweep direction $\big((-)$ 300 kHz$\big)$, 20% smoothing and Q factor of 5.

For a unit pulse duration τ = 0.5 ms, the RF amplitudes were $\gamma B_1^{90}/2\pi = 4600$ Hz and $\gamma B_1^{180}/2\pi = 21851$ Hz, using the optimized relative amplitude ratio $\left(\gamma B_1^{90}/2\pi : \gamma B_1^{180}/2\pi\right)$ of 4.75 (for Q = 5) (Section 3.3.2). All chirp pulses were made with 3000 points, with the points for the composite chirp element distributed in the ratio 1 : 2 : 1.

To test this sequence a purge gradient pulse of 1 ms duration, to suppress unwanted coherences, was added, followed by an on-resonance 90° read pulse to bring the *z*-magnetization into the transverse plane (Figure 4.3a).

4.2.2.1.2.2. Results and Discussion

The sequence of Figure 4.3a successfully delivers uniform, constant phase encoding over 250 kHz as illustrated in the experimental data (dots) and simulation (solid lines) of Figure 4.3b, where hard (blue) and chirp (red dots) pulses are compared.

These results, obtained using τ = 0.5 ms, were before it was realised that for a given Q (5) and sweep width (ΔF) (300 kHz), 1 ms gave better results; the bandwidth achieved is therefore slightly less than in the full CHORUS Oneshot sequence (Section 4.2.2.3).

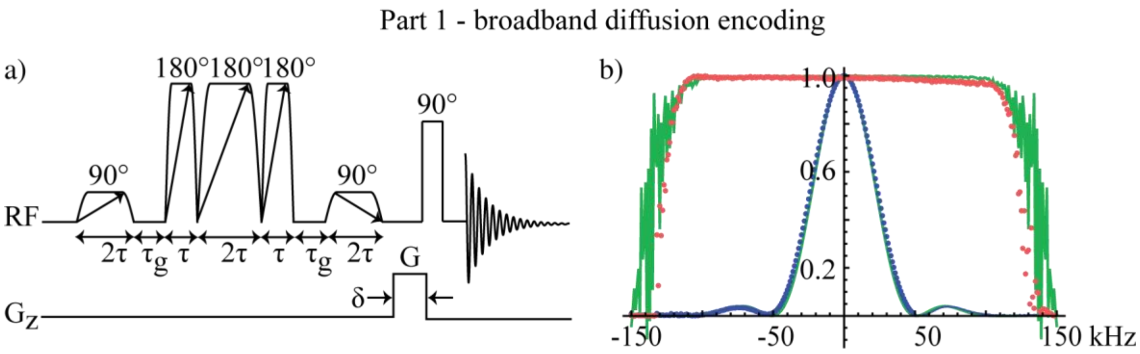

Figure 4.3: a) Broadband diffusion encoding pulse sequence element; b) experimental results (dots) over 300 kHz for a doped water sample, and simulations (green lines) for hard (blue) and chirp pulses (red) using the pulse sequence of Figure 4.3a.

4.2.2.2. Part 2 - Broadband Diffusion Decoding

Part 2 of the development requires converting the broadband encoded *z*-magnetization into observable signal. This is more complicated, since, as discussed in Section 3.3.2, the double chirp combination (90°180°) is extremely sensitive to B_1 amplitude, so that B_1 inhomogeneity causes significant signal loss, and only partially refocuses the frequency dependence of the phase of excitation. In Section 3.3.2.5, and in the recent publication of Power *et al*,[26] a solution to this problem was found, where oversensitivity to B_1 inhomogeneity was overcome by addition of a second 180° chirp pulse to form a triple chirp sequence, CHORUS, which uses the logic of the parent sequence ABSTRUSE (Section 3.3.2.5).[25]

In comparison to ABSTRUSE, the bandwidth of excitation for CHORUS, for the same peak RF amplitude, is 4.2 times greater[26] (Section 3.3.3); however, if uncorrected the frequency-dependent phase errors become much larger. The important proviso when applying the logic of ABSTRUSE[26] is that the residual phase error be corrected for, as outlined in Section 3.3.4.

Thus, CHORUS,[26] using correction for residual phase errors, gives efficient, broadband conversion of longitudinal into transverse magnetization of constant phase. The combination of spatially-encoded *z*-magnetization (Part 1) with the read pulse (CHORUS, Part 2), gives the CHORUS Oneshot pulse sequence of Figure 4.4, where diffusion encoding and decoding field gradient pulses are incorporated into the two halves of the sequence.

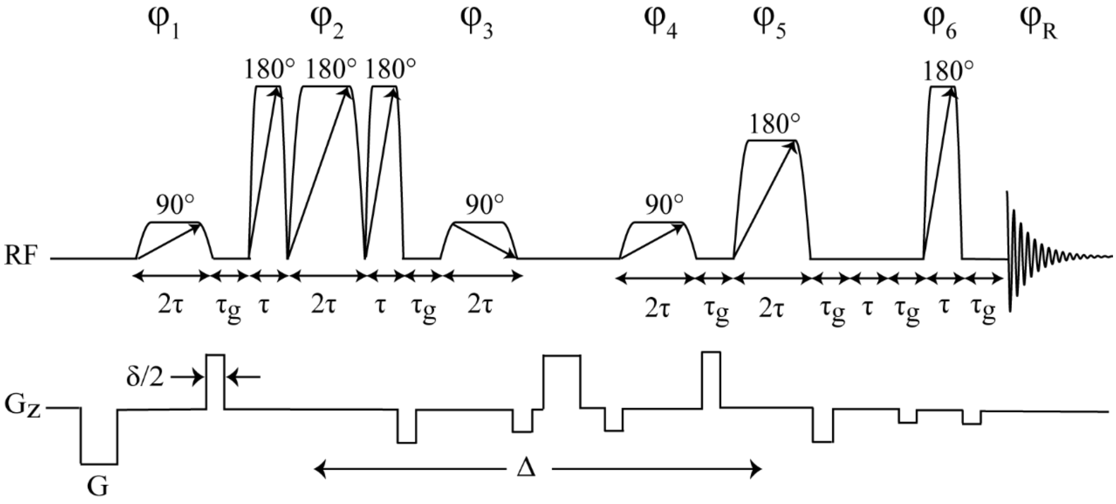

Figure 4.4: CHORUS Oneshot sequence with phases indicated; half-sine shaped gradient pulses were used in practice.

4.2.2.3. CHORUS Oneshot

To test the performance of CHORUS Oneshot, data were acquired and compared to those from the parent Oneshot sequence (using conventional pulses). Excitation profiles were constructed from ^{1}H measurements (Figure 4.5), where the frequency of the excitation varied in steps of 1 kHz over a 300 kHz range. The data for both sets of experiments were acquired non-spinning on a Bruker 500 MHz system using a doped water sample and a 90° pulse width of 8.1 µs. A basic 8-step phase cycle was used (Table 4.1); where more time averaging is needed, the phase cycle can be extended to include EXORCYCLE for all 180° pulses.

Phase of Pulse	8-step Phase Cycle
φ_1	0 0 0 0 0 0 0 0
φ_2	0 0 0 0 1 1 1 1
φ_3	0 0 0 0 0 0 0 0
φ_4	0 0 0 0 0 0 0 0
φ_5	0 0 1 1 0 0 1 1
φ_6	0 1 0 1 0 1 0 1
φ_R	0 2 2 0 2 0 0 2

Table 4.1: Phase cycling used for the excitation profiles of Figure 4.5 using CHORUS Oneshot.

The chirp pulse parameters were as outlined in Section 4.2.2.1.2.1 but with 5% smoothing instead of 20%, where 5% was found to be sufficient to compensate for lack of adiabaticity at the edges for the chirp pulses (Section 3.2.5).

The chirp pulses were generated with 10000 points, where the 10000 points for the composite chirp element were distributed in the ratio 1 : 2 : 1. For a unit pulse duration τ = 1 ms, the RF amplitudes were $\gamma B_1^{90} / 2\pi = 3246$ Hz and $\gamma B_1^{180} / 2\pi = 15451$ Hz, using a relative amplitude ratio $\left(\gamma B_1^{90}/\,2\pi\ :\gamma B_1^{180}/\,2\pi\right)$ of 4.75 (for Q = 5) (Section 3.3.2).

For the CHORUS element of CHORUS Oneshot, the RF amplitude of the first 180° chirp, of pulse duration $\tau = 2$ ms, was 10925.5 Hz, as generated by the Bruker software, where $\gamma B_{1(\max)}\,/\,2\pi/\sqrt{2}$ (Section 3.3.3.2, Figure 3.10c). A time-dependent phase correction was applied to the CHORUS[26] element of CHORUS Oneshot (Section 3.3.4).

4.2.2.3.1. Results and Discussion

The conventional Oneshot sequence gives uniform excitation over less than 10 kHz bandwidth (Figure 4.5); when 50 kHz (or more) from resonance there is negligible excitation. In comparison, CHORUS Oneshot greatly improves this bandwidth to give uniform excitation over more than 250 kHz. This new broadband DOSY sequence covers more than 500 ppm for ^{19}F at 470 MHz, well beyond the width of most ^{19}F spectra.

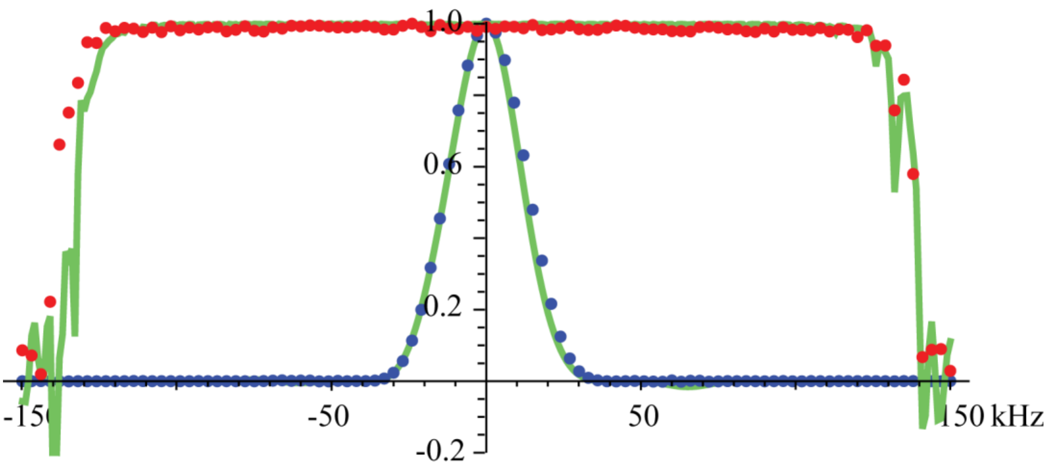

Figure 4.5: Experimental (dots) and calculated (solid lines) ^{1}H excitation profiles for CHORUS Oneshot (red) and conventional Oneshot (blue) for a sample of doped water over a 300 kHz range.

4.3. ^{19}F DOSY

4.3.1. Sample 1

To demonstrate the effectiveness of CHORUS Oneshot, an experiment was performed using a solution containing rosuvastatin (49 mM) and its precursor BEM (46 mM), for which the molecular structures are shown in Figures 4.6 (**1**) and 4.6 (**2**) respectively. Two reference materials were used, C_6F_6 (a common chemical shift reference), and SF_6 (particularly valuable for reference deconvolution).[30] The four fluorine signals in the sample span a chemical shift range of 222 ppm (105 kHz at 470 MHz) (Figure 4.6).

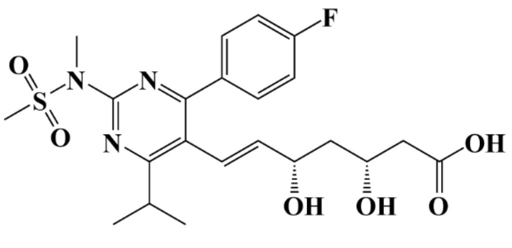

1

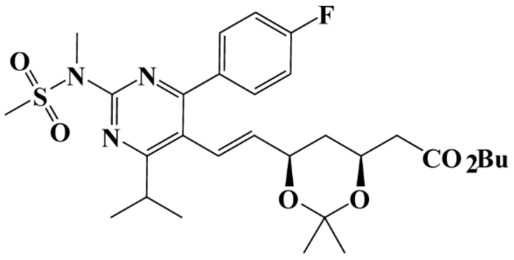

2

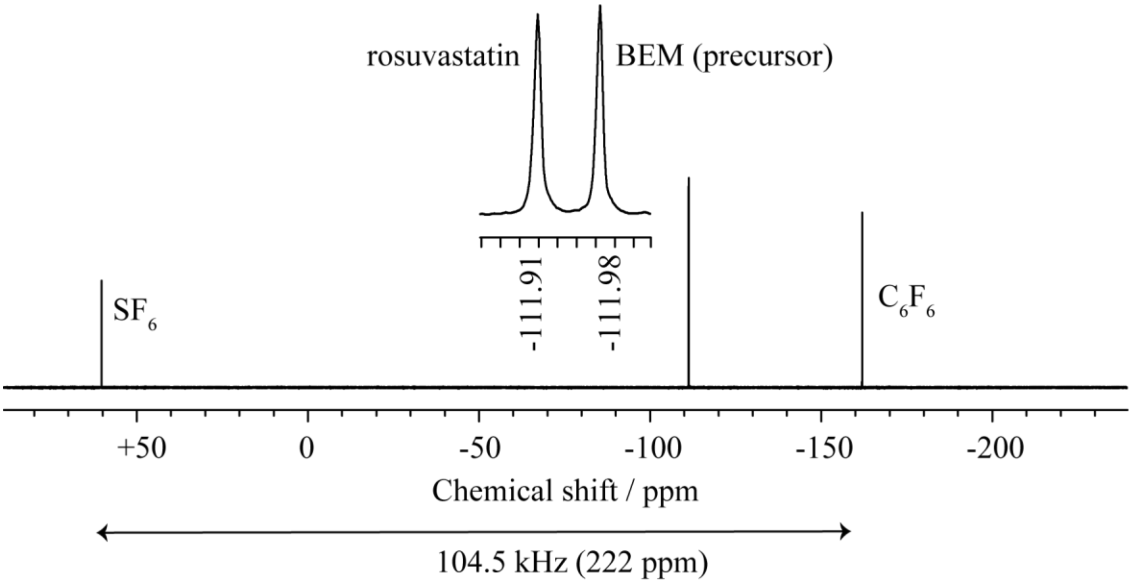

Figure 4.6: ^{19}F spectrum of a solution of rosuvastatin (**1**) and its precursor BEM (**2**) in DMSO-d_6 with SF_6 and C_6F_6 as reference materials. The inset shows an expansion of the area around −111.91 ppm showing the rosuvastatin (left) and BEM (right) signals.

4.3.1.1. Experimental

^{1}H decoupled ^{19}F DOSY spectra were acquired of sample 1 (Figure 4.6) for both Oneshot, using conventional hard pulses (Figure 4.7a), and CHORUS Oneshot (Figure 4.7b). The data were acquired non-spinning on a Bruker 500 MHz system with a 90° pulse width of 15 µs at 298 K.

All data were acquired in 45 min using 16 gradient amplitudes ranging from 2.0 to 24 G cm^{-1} in equal steps of gradient squared, with 16 transients, 262144 complex data points of a total diffusion-encoding gradient pulse duration δ of 2.0 ms and a diffusion time 0.1 s. The chirp pulse parameters for CHORUS Oneshot were as outlined in Section 4.2.2.3.

4.3.1.2. Results and Discussion

Using the conventional Oneshot pulse sequence, only the signals for rosuvastatin (−111.91 ppm) and BEM (−111.98 ppm), are detected (Figure 4.7a). Signals of the two reference materials, at 59.64 ppm (SF_6) and −162.61 ppm (C_6F_6), are absent, as indicted by the empty blue boxes of Figure 4.7a. The transmitter frequency (O1p), set at −111.0 ppm, close to the chemical shifts of drug and precursor, ensures their detection; however, SF_6 and C_6F_6 are too far from resonance to be excited (Section 3.1.3). Thus, using the conventional Oneshot it is impossible to excite the full spectrum at once.

In contrast, CHORUS Oneshot gives full excitation of the complete spectrum, allowing the diffusion coefficients of all four species to be distinguished. The parafluorophenyl signals of rosuvastatin and BEM, a mere 0.07 ppm chemical shift apart, show the exquisite resolving power of ^{19}F NMR.

The chirp pulses of 300 kHz sweep width used in CHORUS Oneshot extend well beyond the chemical shift range of this sample (red arrow of Figure 4.7b). To further demonstrate its use, it was tested on a second sample of even greater chemical shift range.

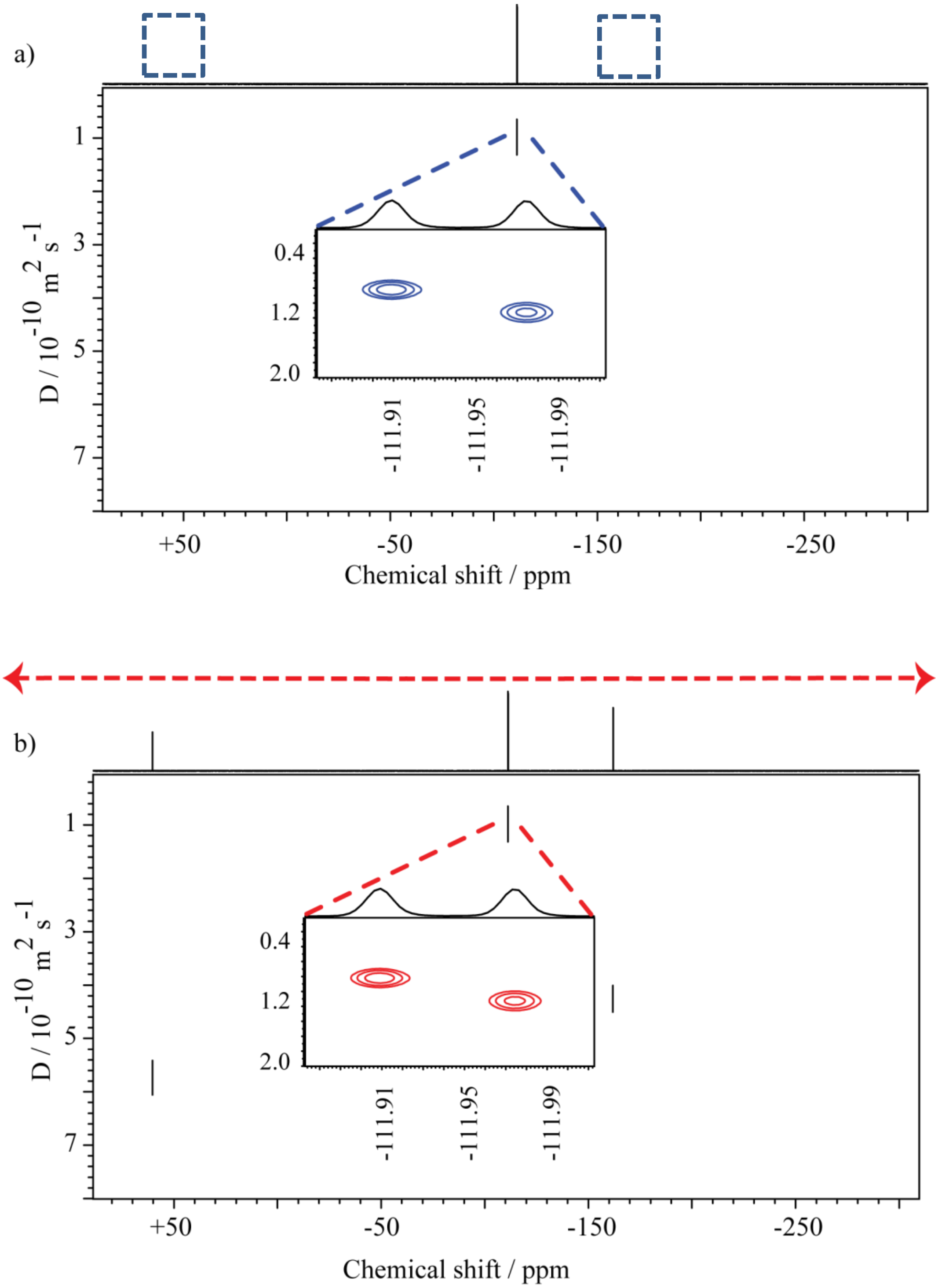

Figure 4.7: a) and b) ^{1}H decoupled ^{19}F DOSY spectrum using Oneshot and CHORUS Oneshot respectively; the data were acquired under the same conditions as outlined in the main text.

4.3.2. Sample 2

For sample 2, the solution contents were as of sample 1 with the addition of the drugs fluconazole and fluticasone propionate, of molecular structures Figures 4.8 (**3**) and (**4**) respectively. This sample had the advantage of a wider chemical shift range of 251 ppm (118 kHz at 470 MHz) containing nine fluorine signals.

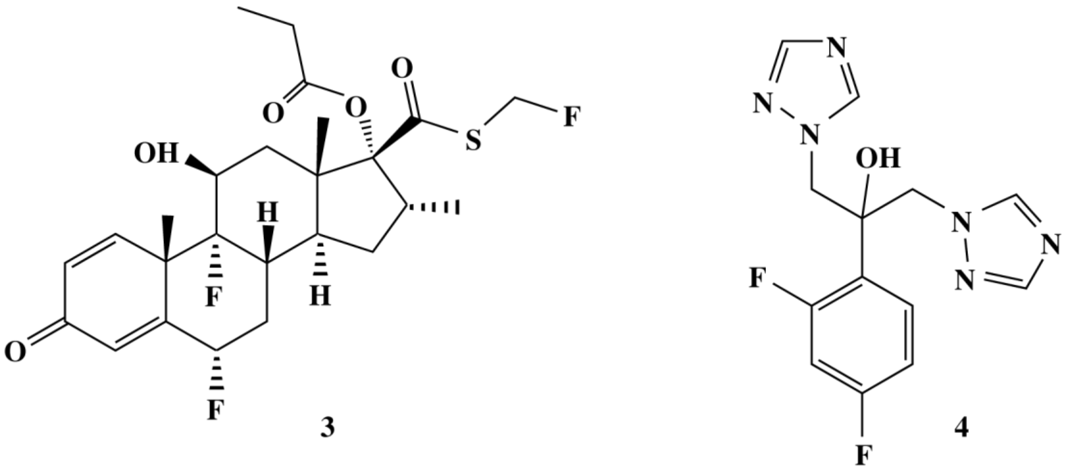

3

4

Figure 4.8: Molecular structures of fluticasone propionate **3** and fluconazole **4** respectively.

4.3.2.1. Experimental

Ms P. Moutzouri and J.E. Power prepared the sample (Table 4.2). The sample was heat treated at 50 °C for three hours to induce the formation of small amounts of impurities, as illustrated in the ^{19}F DOSY spectrum of Figure 4.11b.

Sample 2	Chemical Shift / ppm	Conc. / mM
(1) Rosuvastatin (supplied by AstraZeneca)	−111.91	32
(2) *BEM (supplied by AstraZeneca)	−111.96	33
(3) Fluticasone propionate (Sigma)	−164.19, −186.28, −191.52	13
(4) Fluconazole (extracted from Diflucan formulation)	−107.46, −111.48	26
(5) Hexafluorobenzene (Sigma)	−162.58	7
(6) Sulfur hexafluoride (BOC)	59.64	3
(7) Impurities	−58.22, −111.74, −127.95	1.1, 1.5, 1.3

*tert-butyl-E-(6-[-[4-(4-fluorophenyl)-6-isopropyl-2-[methyl(methylsulfonyl)amino]pyrimidin-5-yl]-vinyl]-((4R,6S)-2,2-dimethyl[1,3]dioxin-4yl) acetic acid).

Table 4.2: Contents, chemical shifts and concentrations of sample 2, prepared in DMSO-d_6. The impurity at −111.74 ppm is named **R2** (see Section 6.2.3.1.2, Chapter 6).

A ^{1}H DOSY spectrum of sample 2 (Figure 4.9) was acquired using Oneshot. The data were acquired non-spinning on a Bruker 500 MHz system with a 90° pulse width of 10 µs at 298 K. For the ^{1}H decoupled ^{19}F DOSY spectra of sample 2, Figure 4.10 and Figures 4.11, data were acquired using Oneshot and CHORUS Oneshot respectively, where Figure 4.11b is the same spectrum as 4.11a but with higher vertical scale. The data were acquired non-spinning on a Bruker 500 MHz system with a 90° pulse width of 12.25 µs at 298 K. All data were acquired in 45 min using 32 gradient amplitudes ranging from 2.7 to 34.5 G cm^{-1} in equal steps of gradient squared, with 8 transients, a total diffusion-encoding gradient pulse duration δ of 2.0 ms and a diffusion time of 0.1 s. For the ^{1}H DOSY and ^{19}F DOSY spectra, 16k and 128k complex data points were used respectively. The chirp pulse parameters for CHORUS Oneshot were as outlined in Section 4.3.1.1.

Experimental data were acquired by Dr. M. Foroozandeh and Ms P. Moutzouri. For the DOSY spectra (Figures 4.9, 4.10 and 4.11), the top trace is the first spectrum and the side, a projection onto the diffusion axis.

4.3.2.2. Results and Discussion

The ^{1}H DOSY spectrum of sample 2 (Figure 4.9) shows many more proton environments then the nine fluorine environments in the ^{19}F DOSY spectrum of Figures 4.11. This exemplifies the advantage of tuning to fluorine instead of proton (once the limitation on excitable bandwidth is overcome). The ^{1}H DOSY spectrum has poor resolution in both dimensions, with signal overlap of the mixture's components prevalent, resulting in compromised accuracy of diffusion coefficients. In addition, impurity signals, such as those observed in the ^{1}H decoupled ^{19}F DOSY of Figure 4.11b, are at best difficult to identify or are partially/completely obscured.

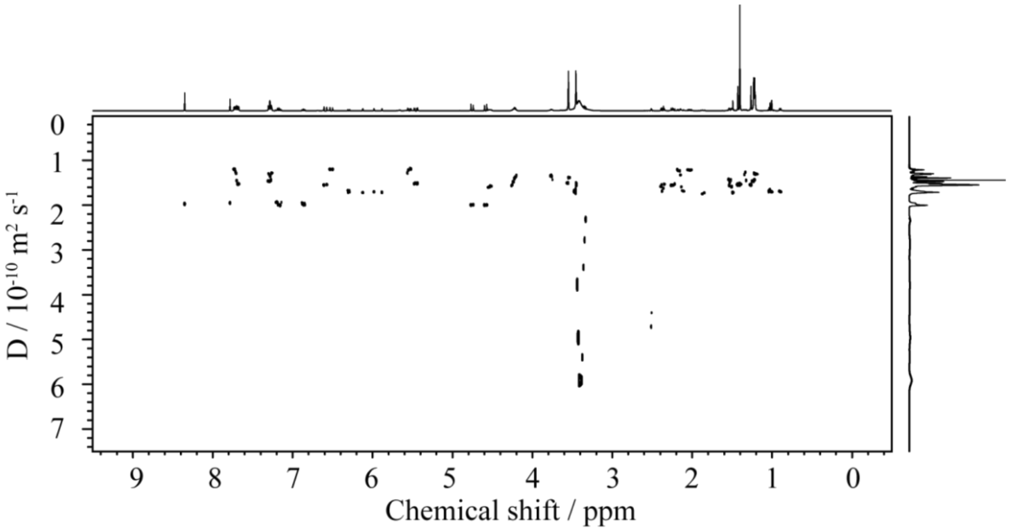

Figure 4.9: 500 MHz ^{1}H Oneshot spectrum of sample 2. Analysis of diffusion coefficients is made difficult due to close proximity and overlapping signals. The broad water signal at approximately 3.4 ppm causes overlapping signals to show an array of compromise apparent diffusion coefficients.

Figure 4.10, the ^{1}H decoupled Oneshot ^{19}F DOSY spectrum of sample 2, shows few, and very low intensity, signals. As concluded in Section 4.3.1.2 for sample 1, due to resonance-offset effects, conventional Oneshot is not able to excite the full spectrum at once. In this sample, the transmitter frequency O1p was set at − 65 ppm (approximately 47 ppm from rosuvastatin). As the excitation profile of Figure 4.5 (Section 4.2.2.3.1) shows, and is evident from this spectrum, signals 50 kHz (or more) from resonance are not excited.

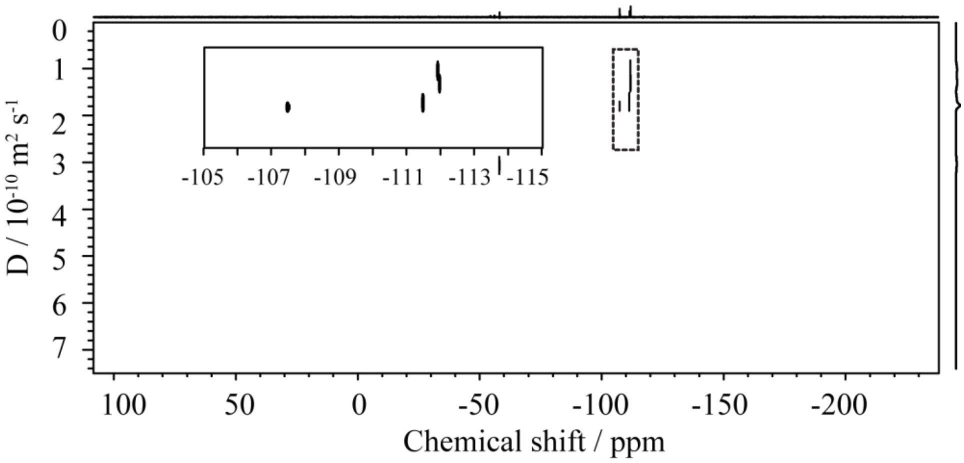

Figure 4.10: 470 MHz ^{1}H decoupled Oneshot ^{19}F DOSY spectrum of sample 2. To make the signals of the top trace visible, the vertical scale was expanded by a factor of 2.3 compared to Figure 4.11.

The ^{1}H decoupled CHORUS Oneshot ^{19}F DOSY spectra of sample 2 (Figures 4.11a and 4.11b), as with sample 1 (Section 4.3.1.2), show full excitation of the complete spectrum. The exquisite resolving power of ^{19}F NMR is once again illustrated in both dimensions of the 2D experiment, where all nine fluorine signals are clearly resolved giving distinguishable diffusion coefficients from signals as far apart as 251 ppm and as close together as 0.05 ppm apart.

As mentioned in the experimental Section 4.3.2.1, the sample was heat treated at 50 °C for three hours. Increasing the vertical scale of Figure 4.11a reveals three impurity signals (red arrows), one adjacent to the rosuvastatin and BEM signals, with a similar diffusion coefficient to BEM, and two at a diffusion coefficient of about 3.6×10^{-10} m^2 s^{-1}, consistent either with a small molecule containing two fluorine atoms, or two species of similar size each containing one fluorine. The concentrations of impurity fluorine at −58.22 ppm, −111.74 ppm and −127.95 ppm are calculated from absolute integrals and the concentrations of known materials (Table 4.2). The impurity at −111.74 ppm (**R2**) is also detected in a (different) degraded sample of rosuvastatin (Section 6.2.3.1.2, Chapter 6).

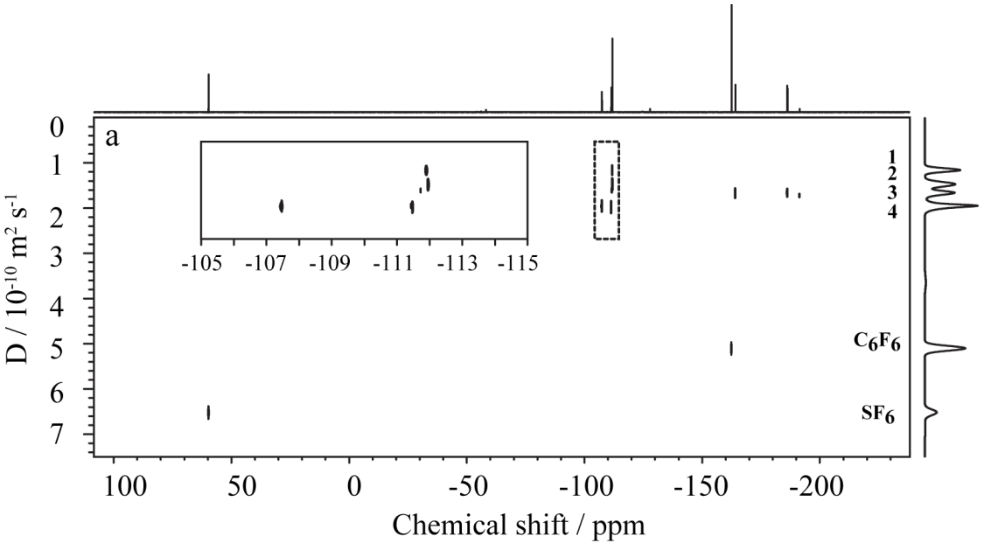

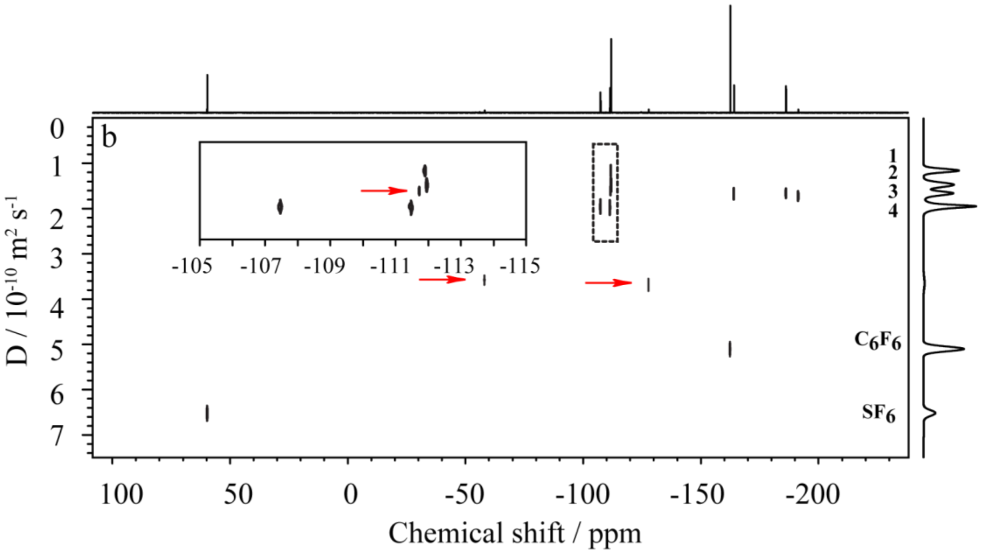

Figure 4.11: a) and b) 470 MHz ^{1}H decoupled CHORUS Oneshot ^{19}F DOSY spectra of sample 2. Spectrum b) is plotted at a higher vertical scale to reveal three impurities, indicated by the red arrows. The inset in a) and b) shows an expansion of the signals 1, 2 and 4.

4.3.3. Conclusion

CHORUS (Section 3) and CHORUS Oneshot by overcoming the limited bandwidth of a simple conventional hard pulses, exploit the exquisite sensitivity of the ^{19}F chemical shift to its local environment, giving excellent resolution. The sequences are not just applicable to fluorine, as shown in this work, but can be applied to other nuclei of wide chemical shift range.

Furthermore, CHORUS sequences offer a valuable tool for impurity analysis (as demonstrated in Chapter 6); the method is able to detect species in a sample, which would be unlikely to be detected by ^{1}H NMR. For example using conventional hard pulses tuned to proton, there is a high probability impurities would be obscured by signal overlap; alternatively, tuned to fluorine, detection, albeit using a well-resolved ^{19}F NMR spectrum, would be left to chance, since it would be dependent on the positioning of the transmitter frequency relative to the unknown species. In practice, this can be overcome by performing a systematic search, using a range of offsets.

Despite the clear advantages of the CHORUS sequences, it is important to address their susceptibility to *J*-modulation (Section 2.8.1). As mentioned for CHORUS (Section 3.4.2.5), swept-frequency pulses last of the order of magnitude of milliseconds; if large homonuclear couplings are present in a sample, then significant evolution can occur under the couplings, so that phase modulation within multiplets causes distortion. Most pharmaceutical drugs have only a few fluorine atoms, so ^{19}F-^{19}F couplings are not an issue; however, multiplet structure in perfluorinated species can be extensive. A potential way to minimize *J*-modulation is to adapt CHORUS sequences by reducing their durations. This can be achieved by adjusting the relative amplitudes and durations of the chirp pulses; however, this can be at the expense of the excitation bandwidth, as was demonstrated in Section 4.2.2.1.2.2 (Figure 4.3b), where for a given Q (5) and sweep width (ΔF) (300 kHz), a unit pulse duration $\tau = 0.5$ ms was used instead of 1 ms. For CHORUS Oneshot, in addition to reducing the pulse duration, modification using a hard 45° pulse centred at the echo maximum, as with the Oneshot45 sequence,[83] can potentially reduce the effects of *J*-modulation by removing unwanted anti-phase terms.

Finally, the two halves of the CHORUS Oneshot sequence, which incorporate diffusion encoding and diffusion decoding field gradients, provide building blocks that may be adapted for a wide range of other uses, for example NOESY, INADEQUATE and INEPT.

Chapter 5

SF_6: A suitable Reference Material for ^{19}F NMR

5. A Suitable Reference Material for ^{19}F NMR

5.1. Introduction

To investigate new and improve existing tools for impurity analysis it was necessary to find a suitable drug, containing low-level impurities, on which the studies could be based. A preliminary investigation, using AZ drug rosuvastatin, showed low-level impurities in the ^{19}F NMR spectra of Figures 6.2 and 6.3 (Section 6.2.2). Before an in-depth analysis of the impurities could be performed such as characterization, a suitable reference material for ^{19}F NMR needed to be found.

5.2. Investigation of Reference Materials

5.2.1. Introduction

A reference material is required to standardize the experiment so that (a) spectra from different spectrometers can be directly compared, (b) to reference the chemical shift scale, and (c) to be used for reference deconvolution (Section 2.6.4).[29-31] The latter is of particular importance when examining low-level impurities, since impurities may be hidden beneath low-level disturbances caused by instrumental imperfections.

For most types of reference deconvolution, the bandshape of the signal must be known, and preferably be a singlet. If the signal is of a complex shape due, e.g. to multiplicity, then reconstruction of the ideal bandshape becomes difficult, leading to inaccuracies in the method. To find a suitable reference material, the bandshapes of the fluorine signals in the ^{19}F spectra of the common ^{19}F reference materials trichlorofluoromethane ($CFCl_3$) and hexafluorobenzene (C_6F_6) and of sulfur hexafluoride (SF_6) were analysed in terms of lineshape and multiplicity.

5.2.2. ^{19}F spectra of $CFCl_3$ and C_6F_6

5.2.2.1. Experimental

$CFCl_3$ (~ 318 mM) and C_6F_6 (~ 53 mM) were dissolved in DMSO-d_6. An NMR tube with a screw lid cap, which is gas tight with a PTFE/silicone septum, was used in order to reduce evaporation of the $CFCl_3$. ^{19}F NMR measurements were carried out, non-spinning, on a Varian VNMRS 500 MHz spectrometer at 298 K. The data were recorded using 524288 complex data points with a relaxation delay of 4.6 s between scans and a total experiment time of 13 h 11 min in order to obtain experimentally high SNR.

5.2.2.2. Results and Discussion

Chlorine is a quadrupolar nucleus with nuclear spin quantum number $I = 3/2$. Chlorine has two NMR active species, ^{35}Cl and ^{37}Cl, with natural abundances of 75.5 % and 24.5% respectively. The fluorine signal in the ^{19}F spectrum of $CFCl_3$ exhibits a multiplet structure of four peaks (Figure 5.1a), where the splitting is due to the ^{37}Cl / ^{35}Cl secondary isotope effects on the ^{19}F chemical shift.[84] The relative intensities of the four peaks (1 : 0.958 : 0.306 : 0.0325) are calculated from the natural abundances of ^{35}Cl and ^{37}Cl using Equation 5.1:

$$x^3 : 3x^2(1-x) : 3x(1-x)^2 : (1-x)^3 \tag{5.1}$$

The ^{19}F spectrum of C_6F_6 has a single resonance of approximately 95 % signal intensity; the remainder is distributed across in the multiplet structure of its ^{13}C satellites, due to ^{13}C-^{19}F coupling and ^{19}F-^{19}F couplings of the magnetically non-equivalent fluorine atoms on the benzene ring (Figure 5.1b). The one-bond ^{13}C satellites are either side of the main signal and at approximately 0.55% of the main signal intensity; the lack of symmetry about the main signal arises from a secondary isotope shift. This is due to the change in reduced mass from ^{12}C to ^{13}C affecting the vibrational frequency of the F-C bond, and hence its zero point energy and the average electron density at fluorine, causing a small difference in ^{19}F chemical shift.

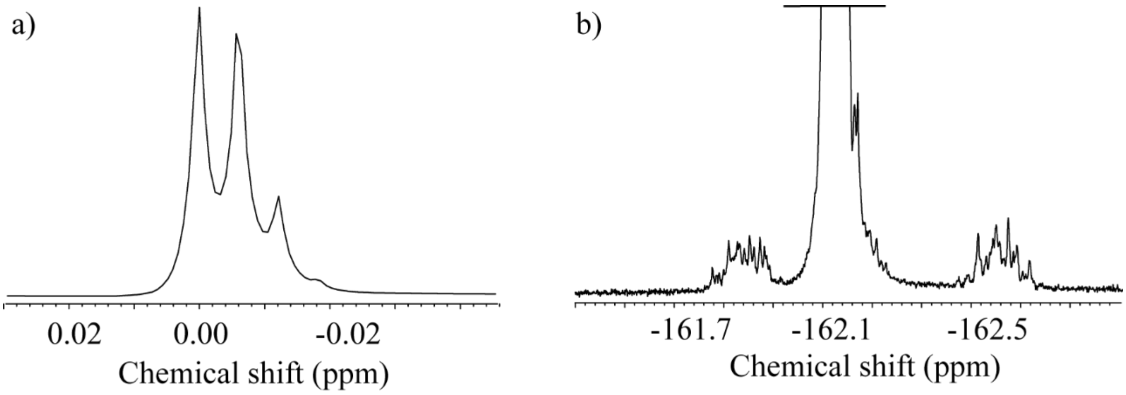

Figure 5.1: a) ^{19}F spectrum of $CFCl_3$ showing the fluorine signal split into a multiplet of four peaks due to the ^{37}Cl / ^{35}Cl isotope effects on the ^{19}F chemical shift; poor digitization is apparent (see also Figure 5.2a). b) The ^{19}F spectrum of C_6F_6, with a high vertical scale, showing the complex multiplet structure of its ^{13}C satellites.

In terms of suitability for reference deconvolution, the bandshapes of the fluorine signals for $CFCl_3$ and C_6F_6, Figures 5.1a and 5.1b respectively, are far from ideal. The former, being the less complex, was used for reference deconvolution. The method was performed in the Vnmr software using the command fiddle('satellites','$CFCl_3$'). A theoretical satellites file was created containing information on coupling constants (set to zero), relative peak intensities (1 : 0.958 : 0.306 : 0.0325), and measured frequency shifts (secondary isotope shifts) (Table 5.1), where the one-bond ^{13}C satellites were excluded, since they were of sufficient distance from the fluorine signal.

relative peak intensities	secondary isotope shifts / ppm
1.000	0.000
0.9580	0.006
0.3060	0.012
0.0325	0.018

Table 5.1: Theoretical $CFCl_3$ satellites file based on published abundances of ^{35}Cl and ^{37}Cl, showing relative intensities calculated using Equation 5.1 and measured frequency shifts (0.006 ppm / 2.8 Hz) between each peak, where the coupling constants were set at zero.

Figure 5.2a shows the ^{19}F spectrum of $CFCl_3$ (upper) aligned with the reference deconvoluted spectrum of $CFCl_3$ (lower) using the theoretical satellites file (Table 5.1); poor digitization is apparent. In order to improve the accuracy of the reference deconvolution, and to improve the bandshapes, it is recommended to double the zero filling (Section 2.6.1) with respect to the number of complex data points. With these data this was not possible, since the maximum number of complex data points had been used in the acquisition of a ^{19}F spectrum of wide spectral width. Reference deconvolution of $CFCl_3$ enhances the resolution of the four peaks, which is a Lorentz-to-Gauss transform (Section 2.6.3) but results in a decrease in SNR.

Figure 5.2b shows the ^{19}F spectrum of C_6F_6, before (upper) and after (lower), reference deconvolution using the $CFCl_3$ satellites file (Table 5.2), where the theoretical satellites file (Table 5.1) was partially optimised using manual iteration. Imperfect estimates of relative intensities and secondary isotope shifts in the satellites file, lead to artefacts close to the parent signal of C_6F_6.

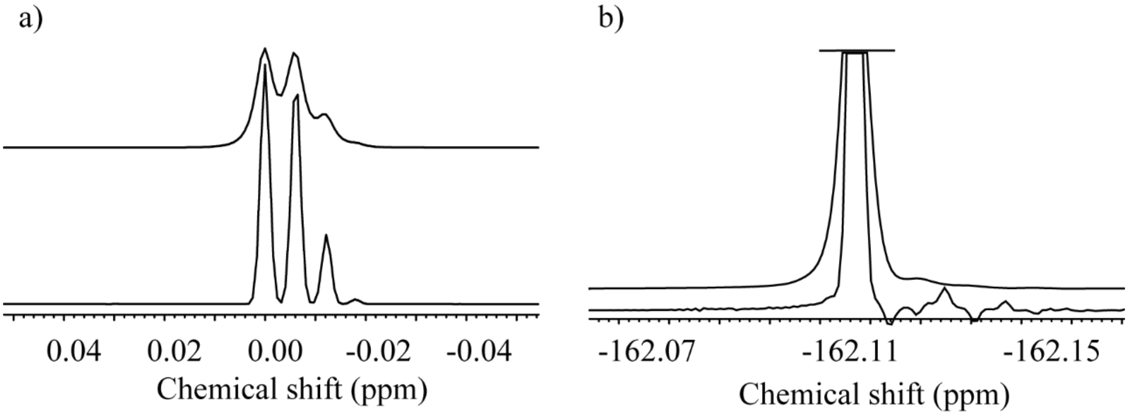

Figure 5.2: a) The ^{19}F spectrum of $CFCl_3$ (upper) aligned and superimposed onto the reference deconvoluted spectrum of $CFCl_3$ (lower). b) The ^{19}F spectrum of C_6F_6 with increased vertical scale, before (upper) and after (lower) reference deconvolution using the partially optimized $CFCl_3$ satellites file of Table 5.2 with estimated 2° isotope shifts.

relative peak intensities	**secondary isotope shifts / ppm**
1.000	0.00000
0.9440	0.00611
0.2840	0.01220
0.0326	0.01800

Table 5.2: Partially optimized $CFCl_3$ satellites file using manual iteration of the theoretical satellites file (Table 5.1) to give the results of Figure 5.2b, where the coupling constants were set at zero.

Figure 5.3 shows the spectrum of C_6F_6 reference deconvoluted using the optimized $CFCl_3$ satellites file (Table 5.3), where the frequency shifts and amplitudes in Table 5.2 were further adjusted by manual iteration, to minimize the artefacts in the C_6F_6 spectrum (A, B, C and D) (Figure 5.2). The artefacts are reduced to a level of 0.3 % with respect to the parent signal.

The isotope distribution of the optimized satellites file (Table 5.3) is slightly different from the statistical (Table 5.1), suggesting presence of isotope effects in the synthesis of $CFCl_3$.

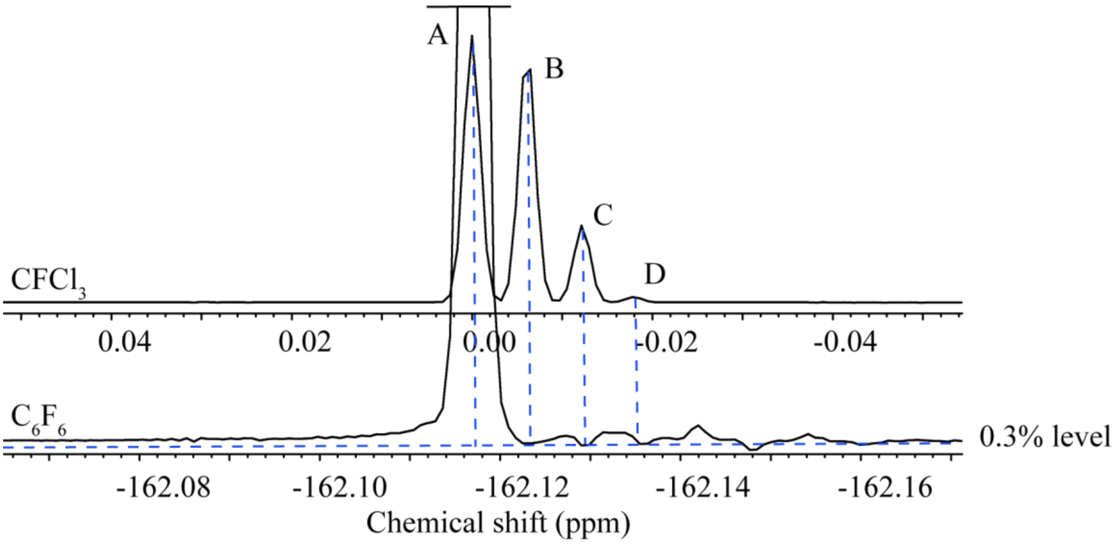

Figure 5.3: The ^{19}F spectrum of C_6F_6 (lower spectrum) reference deconvoluted using $CFCl_3$ (upper spectrum), with an empirically optimized satellites file (Table 5.3). The frequency shifts of C_6F_6, compared to $CFCl_3$, are closely matched (A, B, C and D), similarly are the amplitudes resulting in a near flat, cleaner baseline, with less phase and frequency shift errors; the effects of the artefacts are reduced to 0.3 % of the parent signal.

relative peak intensities	secondary isotope shifts / ppm
1.000	0.00000
0.950	0.00612
0.290	0.01225
0.020	0.01800

Table 5.3: Optimized $CFCl_3$ satellites file using manual iteration of Table 5.2 to give the results of Figure 5.3, where the coupling constants were set at zero.

Using $CFCl_3$ for reference deconvolution, though not ideal with its four signals, can correct the spectrum of C_6F_6 (Figure 5.3) to a useful extent. As an alternative to $CFCl_3$, the bandshape of the fluorine signal of SF_6 was investigated in the hope of obtaining even cleaner results.

5.2.3. SF_6 as a Reference Material

5.2.3.1. Introduction

SF_6 is not generally considered (or widely used) as a reference material for ^{19}F NMR; however, in terms of its physical properties, it lends itself very nicely to this use. It is a colourless, highly non-flammable, non-toxic gas at room temperature; an extremely stable molecule that can be heated up to 500 ºC without decomposition. Its stability arises from its structure; it is a non-polar, hypervalent molecule, octahedral in shape, with strong S-F covalent bonds, and the central sulfur atom well shielded.[85]

To consider its use as a reference material for ^{19}F NMR, first it was important to examine the NMR properties of sulfur isotopes and the solubility of SF_6 in polar and non-polar solvents.

5.2.3.2. NMR Properties of Sulfur Isotopes

Sulfur has four isotopes, only one of which is NMR active (^{33}S) with low natural abundance of 0.76 % (Table 5.4), $I = 3/2$, and, in comparison to proton ($\gamma = 267.51 \times 10^6$ rad $s^{-1}T^{-1}$), low gyromagnetic ratio $\gamma = 20.55 \times 10^6$ rad $s^{-1}T^{-1}$.

Isotopes of Sulfur	Natural Abundance (atom %)	Nuclear Spin (I)
^{32}S	94.93	0
^{33}S	0.76	3/2
^{34}S	4.29	0
^{36}S	0.02	0

Table 5.4: Four isotopes of sulfur with their corresponding nuclear spin quantum numbers and their natural abundances.

5.2.3.2.1. ^{19}F spectra of SF_6

SF_6 dissolves sufficiently in deuterated chloroform ($CDCl_3$) (Section 5.2.3.3.4) to show a strong singlet, a weaker singlet, and a quartet splitting pattern 1:1:1:1 (Figure 5.4). The splitting pattern is due to coupling of fluorine to the isotope ^{33}S. The peak heights, approximately 0.14 % that of the parent peak, are slightly lower than the expected value of 0.19 %; this may be due to line broadening caused by quadrupolar relaxation (Section 2.4.2.1).

The inset in Figure 5.4 shows an expansion of the signals at approximately 60.2 ppm. The extra signal observed is approximately 4% of the parent peak and is caused by a secondary isotope shift, since there is a change in reduced mass from ^{32}S to ^{34}S (Section 5.2.2.2).

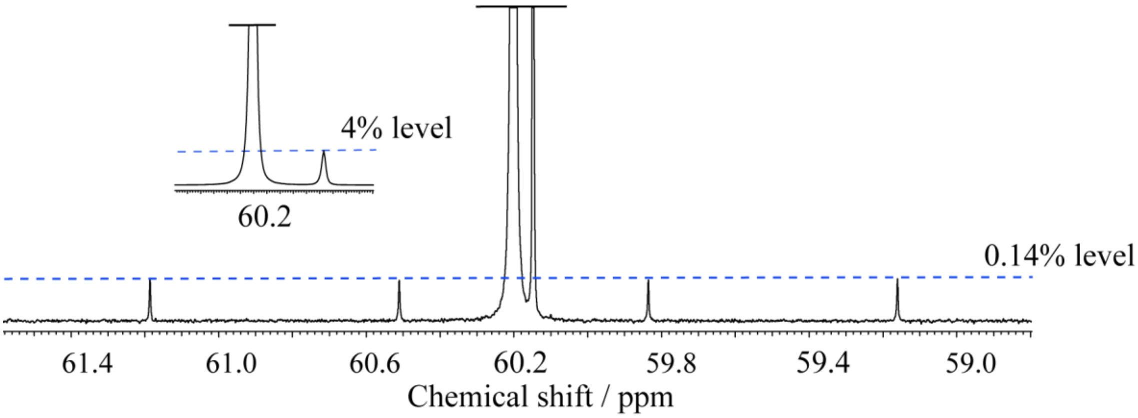

Figure 5.4: ^{19}F spectrum of SF_6 in DMSO-d_6; the extra signal next to the parent peak is due to a ^{34}S secondary isotope shift, the quartet to comply to ^{33}S.

The fluorine signal and satellites in the ^{19}F spectrum of SF_6 (Figure 5.4) do not have complex multiplet structures, as was observed in the ^{19}F spectra of $CFCl_3$ and C_6F_6 (Figures 5.1a and 5.1b). As a reference material for reference deconvolution, SF_6 would be far more suitable, providing it is sufficiently soluble in the solvent of choice, which in the analysis of rosuvastatin, was DMSO-d_6.

5.2.3.3. Solubility and Polarity of SF_6

5.2.3.3.1. Introduction

In order to investigate the solubility of SF_6 a series of experiments was carried out to find (a) the minimum bubbling time required to saturate the solvent, so as to maximize concentrations levels in experiments, (b) the most efficient NMR tube in preventing evaporation of gas over long time periods, using standard capped, screw capped and J-Young NMR tubes, and (c) the solubility in deuterated solvents of increasing polarities.

Before commencing experiments, a brief literature comparison was made of the solubility of SF_6 in hexane, isobutanol and dimethyl carbonate (DMC) (Table 5.5). These solvents were chosen because the literature on solubility of SF_6 in DMSO-d_6 is limited. SF_6 is a non-polar gas; therefore, as expected, solubility of SF_6 decreases with increasing polarity of solvent. It is only slightly soluble (0.24 mM) in water, which is a polar protic solvent (Table 5.5). DMSO-d_6, even though polar, is aprotic with a lower dielectric constant than water, therefore, in comparison, SF_6 is expected to be more soluble.

Solvent	**Mole Fraction Solubility's ($10^4 x_2$)**	**Molarity (mM)**
Hexane[86]	107.7	82
Isobutanol[87]	34.04	37
Dimethyl carbonate[88]	30.56	36
water (slightly soluble)[89]	0.0439	0.24

Table 5.5: Solubility of SF_6 gas in solvents of increasing polarity: hexane at 298.15 K, isobutanol at 293.15 K, dimethyl carbonate at 288.15 K and water at 298.15 K.

5.2.3.3.2. Solvent Saturation

In order to ascertain the time taken to saturate a solution of DMSO-d_6, SF_6 was bubbled directly into prepared standard capped NMR tubes for different times. An AstraZeneca reference standard, 4-fluorobenzoic acid (4FBA), was used for quantitation. In addition, a screw capped tube was used to see how efficiently it could retain the gas, over a period of eight days, in comparison to the standard capped NMR tubes.

5.2.3.3.2.1. Experimental

A sample of 4FBA (44 mM) in DMSO-d_6 was prepared and placed in equal amounts into six different standard capped NMR tubes and one screw capped tube; the tubes were maintained at constant temperature of 298 K. SF_6 gas was bubbled into the tubes for times of 0.5 min, 1 min, 2 min, 4 min, 8 min and 16 min; the bubbling time for the screw capped tube was 16 min. For the 16 min bubbling time, the tubes were stored at room temperature away from direct light and analysis was repeated after eight days.

^{19}F NMR measurements were carried out immediately after bubbling, non-spinning, on a Varian VNMRS 400 MHz spectrometer at room temperature; to test reproducibility, the measurements were repeated three times. The analysis was kept at a lower temperature than the bubbling temperature to prevent bubble formation during analysis. The data were recorded using 262144 complex data points with a relaxation delay of 5.5 s between scans and a total experiment time of 1 min 17 s. The relaxation time constants T_1 for 4FBA and SF_6, were 3.4 s and 0.9 s respectively.

5.2.3.3.2.2. Results

Figure 5.5 shows the normalized averaged absolute integrals of the fluorine signal of SF_6 as a function of time. DMSO-d_6 was saturated with SF_6 in less than 2 min bubbling time. After a period of 8 days, the standard (orange) and screw capped (green) tubes lost over 50 % of the gas.

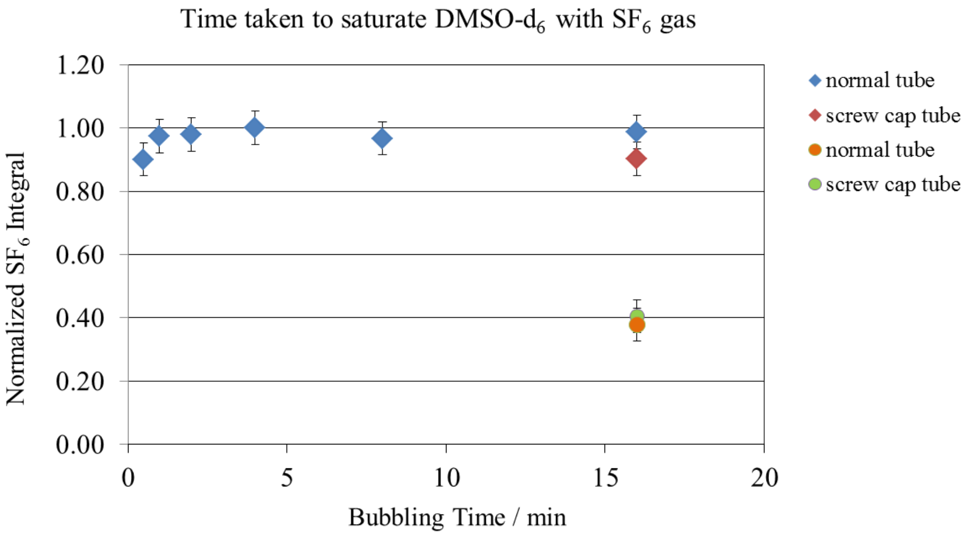

Figure 5.5: Graph of normalized averaged absolute integral of the fluorine signal of SF_6 as a function of time. DMSO-d_6 became saturated within less than 2 min bubbling time.

5.2.3.3.3. Retention of SF_6 in a J-Young NMR Tube

The retention of SF_6 in standard capped and screw capped NMR tubes is poor. To see if retention of gas in the tube could be improved, the experiment was repeated using a J-Young tube over a longer time-period. A J-Young tube has a valve system sealed by a pair of rubber O-rings, which in comparison to a screw capped NMR tube, has a PTFE/silicone septum under the lid.

5.2.3.3.3.1. Experimental

A sample of 4FBA (22.72 mM) in DMSO-d_6 was prepared in a J-Young tube. The sample was saturated with SF_6 gas at 298 K (Section 5.2.3.3.2). ^{19}F NMR measurements were carried out immediately after saturation, non-spinning, on a Varian VNMRS 400 MHz spectrometer at room temperature; to test reproducibility, the measurements were repeated three times.

The data were recorded using 524288 complex data points with a relaxation delay of 25 s between scans and a total experiment time of 7 min 7s. The analysis was repeated after intervals of 6 days, 13 days, 20 days and 40 days; the tubes were stored at room temperature away from direct light.

The transmitter offset was arrayed to put the fluorine signal of 4FBA and SF_6 on resonance at the centre of the spectral window, alternately. This was to increase accuracy of the integrals by eliminating any loss of signal due to off-resonance effects (Section 3.1.3) and to remove any bias caused by the receiver characteristics towards the edges of the spectral window (Section 3.4.2.4).

5.2.3.3.3.2. Results

Table 5.6 shows the average concentration of SF_6 in a saturated solution of DMSO-d_6. The concentrations were calculated from the known concentration of 4FBA and the averaged absolute integrals of the fluorine signals of SF_6.

Time (days)	Average SF_6 concentration / mM
0	2.45
6	2.42
13	2.41
20	2.39
40	2.38

Table 5.6: The average concentration of SF_6 in a saturated solution of DMSO-d_6 in a J-Young NMR tube over a 40-day time-period.

5.2.3.3.3.3. Comment

The J-young tube greatly reduces evaporation of gas, and after a total of 40 days there was only a 3 % loss; therefore, it is recommended for use.

5.2.3.3.4. Solubility in Deuterated Solvents

The solubility of SF_6 was tested in five different deuterated solvents of increasing polarity, chloroform ($CDCl_3$), acetone (CD_3COCD_3), methanol (CD_3OD), dimethyl sulfoxide (DMSO-d_6) and water (D_2O).

In the analysis of $CDCl_3$ and CD_3OD, the reference material 4FBA was used; for D_2O and CD_3COCD_3, sodium trifluoromethanesulfonate (NaTrif) was used since 4FBA was not sufficiently soluble.

5.2.3.3.4.1. Experimental

Samples of 4FBA and NaTrif (Aldrich CAS: 367907-56) were prepared in duplicate in deuterated solvents $CDCl_3$, CD_3COCD_3, CD_3OD, DMSO-d_6 and D_2O; the solvents were saturated with SF_6 at 298 K in standard capped NMR tubes.

^{19}F NMR measurements were carried out as outlined in Section 5.2.3.3.3.1. The relaxation time constants T_1 for 4FBA and SF_6 are given in Section 5.2.3.3.2.1, for NaTrif, $T_1 = 3.3$ s.

5.2.3.3.4.2. Results

Table 5.7 shows the average concentrations of SF_6 in saturated solutions for five deuterated solvents. To check experimental accuracy over the six experiments for each solvent, the ratio of absolute integral of reference material to its concentration was calculated, from which were calculated percentage deviations (Table 5.7).

Deuterated Solvents	**Average Concentration of SF_6 gas / mM**	**STDEV / %**
$CDCl_3$	35.4	0.2
CD_3COCD_3	28.7	0.7
CD_3OD	20.4	0.3
DMSO-d_6	2.4	0.8
D_2O	0.3	0.2

Table 5.7: The average concentrations of SF_6, and percentage standard deviations, in saturated solutions of five deuterated solvents, using standard capped NMR tubes.

5.2.3.3.4.3. Comment

As is to be expected, the solubility of SF_6 decreases with increasing polarity of solvent. The solubility of SF_6 at room temperature in DMSO-d_6, though relatively low at 2.4 mM, in comparison to less polar solvents, is sufficient for it to be used as a reference material in the analysis of low-level impurities.

Chapter 6

Low-Level Impurity Analysis of Rosuvastatin

6. Low-Level Impurity Analysis of Rosuvastatin

6.1. Introduction

A preliminary investigation of rosuvastatin (Figure 6.1a) shows multiplet structure of the main fluorine signal and complex splitting patterns for its ^{13}C satellites, Figures 6.1b and 6.1c respectively. To study low-level impurities effectively, this multiplicity needs to be removed by decoupling, since impurities may be hidden beneath the multiplets.

To address this, ^{19}F{^{1}H} decoupling was performed on a Bruker 500 MHz spectrometer, to reveal low-level impurities in the ^{1}H decoupled ^{19}F NMR and ^{19}F DOSY spectra of rosuvastatin, Figures 6.2 and 6.3 respectively. Ideally, a triple resonance experiment should be performed to decouple ^{19}F{^{13}C} and ^{19}F{^{1}H} couplings simultaneously. This was not possible on the Bruker system due to hardware limitations of the probe used; as an alternative approach, a Varian VNMRS 500 MHz spectrometer was used with a triple resonance HCN triple axis gradient 5 mm probe. This probe presented a different technical problem to the former, which was overcome, such that a triple resonance experiment could be performed to reveal a third impurity (Figures 6.6, 6.7 and 6.8). For all experiments, SF_6 was used as a reference material.

6.1.1. ^{19}F spectra of Rosuvastatin

Figure 6.1b shows the ^{19}F spectrum of rosuvastatin, showing the effect of the scalar coupling of the fluorine atom to the nearby hydrogen atoms in the ortho (H_{17}/H_{21}) and meta (H_{18}/H_{20}) positions on the benzene ring, to give a ^{1}H-^{19}F spin system of type $AA^{'}BB^{'}X$. Figure 6.1c shows the fluorine signals coupled to ^{13}C. The one-bond ^{13}C satellites, of spin system type $AA^{'}BB^{'}MX$, are either side of the main signal and at approximately 0.55% of the main signal intensity; the lack of symmetry about the main signal arises from a secondary isotope shift (Section 5.2.2.2). The complex multiplet structures of the satellites are due to C-F couplings ($^{1}J_{\mathrm{C19F22}}$) and F-H couplings (J_{HF}), where the aromatic ^{1}H's bonded to ^{13}C are not magnetically equivalent. Also observed are long-range ^{13}C satellites ($^{2}J_{\mathrm{CF}}$) to the right of the main fluorine signal.

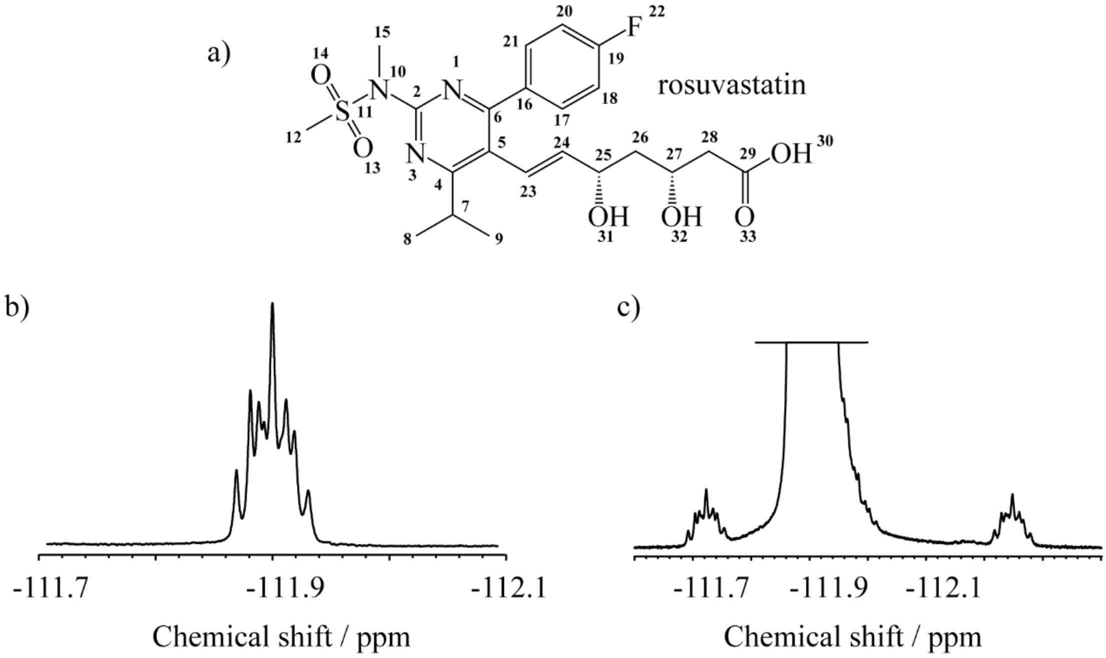

Figure 6.1: a) Molecular structure of rosuvastatin, b) ^{19}F spectrum of rosuvastatin showing the effect of the scalar coupling of the fluorine atom to the nearby hydrogen atoms on the benzene ring, and c) vertically expanded ^{19}F spectrum of rosuvastatin, showing the ^{13}C satellites either side of and just to the right of the main signal.

6.2. $^{19}\mathrm{F}\{^{1}\mathrm{H}\}$ Decoupling of Rosuvastatin (Bruker System)

^{1}H decoupled 1D and DOSY ^{19}F NMR spectra of rosuvastatin were acquired using the CHORUS[26] (Section 3.3.5) and CHORUS Oneshot (Section 4.2.2.3) pulse sequences, Figures 6.2 and 6.3 respectively. The CHORUS sequences are of particular use for impurity analysis in accommodating the wide chemical shift range between drug (rosuvastatin at −111.91 ppm) and reference material (SF_6 at 59.69 ppm) of approximately 172 ppm.

6.2.1. Experimental

Rosuvastatin (25 mM) was dissolved in DMSO-d_6. The sample, prepared in a standard capped NMR tube, was saturated with SF_6 gas at 298 K (Section 5.2.3.3.2). ^1H decoupled ^{19}F NMR measurements were carried out immediately after saturation, non-spinning, on a Bruker 500 MHz system with a 90° pulse width of 12.25 µs. For CHORUS, the chirp pulse parameters were as outlined in Section 3.3.3.1. The data were recorded using 262144 complex data points with a relaxation delay of 6 s between scans and a total experiment time of 1 h 1 min 33 s. ^1H decoupled ^{19}F DOSY measurements on the same sample were acquired, non-spinning, on a Bruker 500 MHz system at 298 K using CHORUS Oneshot (Section 4.2.2.3). Data were acquired with an array of 32 gradient amplitudes ranging from 2.7 G cm^{-1} to 32.1 G cm^{-1}, using 128 transients, 262144 complex data points, a total diffusion-encoding gradient pulse duration δ of 2 ms, and a diffusion time 0.1 s. The chirp pulse parameters for CHORUS Oneshot were as outlined in Section 4.3.1.1.

6.2.2. Results and Discussion

The two impurity signals **R1** and **R3** of Figure 6.2 were revealed by applying a heavy Gaussian weighting function in the time domain, to enhance sensitivity, allowing the vertical scale to be greatly increased. The relative intensities of different signals are listed in Table 6.1. An expansion of the crowded region at approximately −111.91 ppm shows the impurity signal **R3** more clearly. Low-level disturbances **d** can be seen at approximately 0.05% intensity of the parent peak; they are broad and irregular, and attributed to vibrations during the experiment.

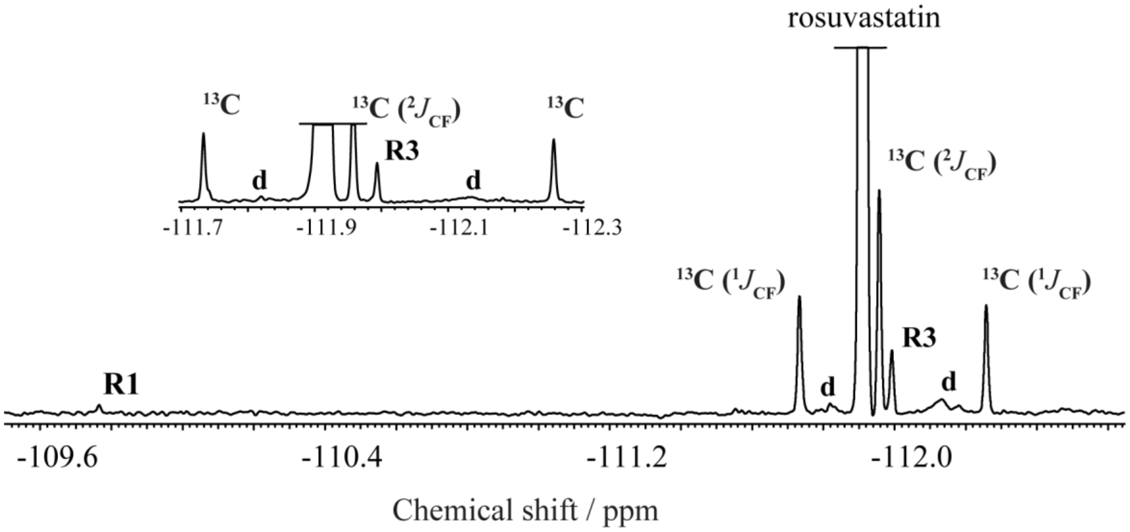

Figure 6.2: ^{1}H decoupled CHORUS ^{19}F NMR spectrum of rosuvastatin, with an expansion of the region around −111.91 ppm. Two impurity signals are revealed, **R1** and **R3**, and low-level disturbances **d**, which are broad and irregular. ^{1}H decoupling was performed using WALTZ16[90] with an RF amplitude of 3125 Hz.

The ^{1}H decoupled ^{19}F DOSY spectrum (Figure 6.3) shows the apparent diffusion coefficients of rosuvastatin, impurity **R3** and the ^{13}C satellites; the signal of impurities **R1** might be revealed with more time averaging (Section 2.6.2). There is no significant difference in diffusion coefficient between impurity and rosuvastatin (and its ^{13}C satellites), suggesting that the species is of a similar molecular size to rosuvastatin.

Figures 6.2 and 6.3 show high dynamic range between drug (25 mM) and impurity signals (≤ 0.07 mM) (Table 6.1). As noted for Figure 4.11 (Section 4.3.2.2), the ^{19}F DOSY spectrum offers excellent resolution with distinguishable diffusion coefficients.

The impurity signals of Figure 6.2 and 6.3 are *not* seen in the spectrum of a fresh sample (Section 6.2.3.1.1, Figure 6.8b). They presumably arise from degradation of the rosuvastatin sample, which was prepared 3-4 months prior to use, despite it being stored in a refrigerator.

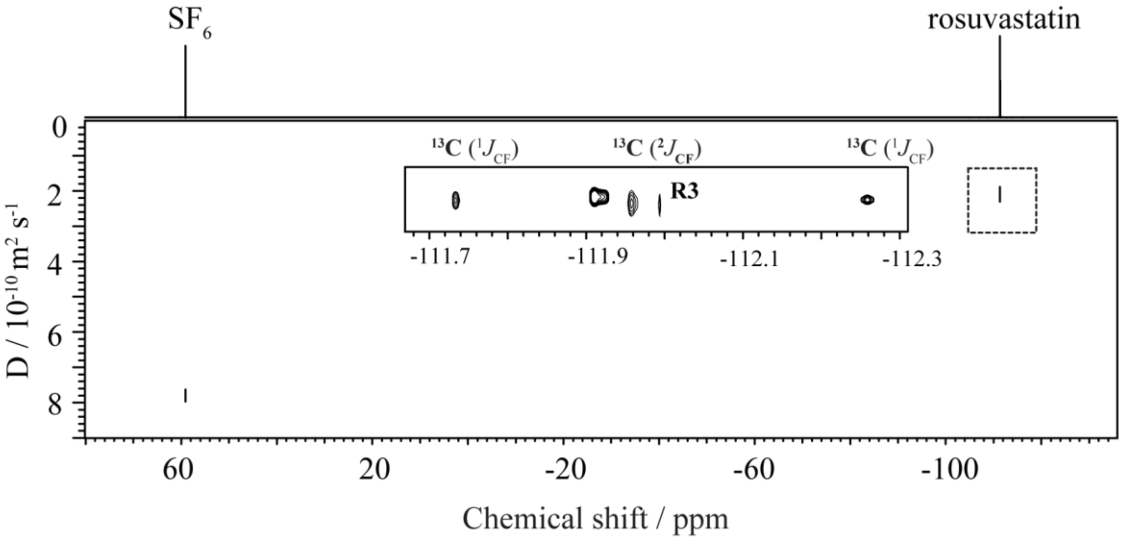

Figure 6.3: ^{1}H decoupled ^{19}F DOSY spectrum of rosuvastatin, using CHORUS Oneshot, with an expansion of the region around −111.91 ppm. ^{1}H decoupling was performed using WALTZ16[90] with an RF amplitude of 3125 Hz.

Known Species	**Chemical Shift / ppm**	**^{19}F conc. / mM**	**% intensity**
Rosuvastatin	–111.91	25.0	100.00
SF_6	59.69	2.54	10.2
^{13}C satellites ($^{1}J_{CF}$)	–111.73, –112.26	0.15, 0.13	0.59, 0.50
^{13}C satellite ($^{2}J_{CF}$)	–111.96	0.26	1.05

Impurities	**Chemical Shift / ppm**	**^{19}F conc. / mM**	**% intensity**
R1	–109.77	0.01	0.05
R3	–111.99	0.07	0.28

Table 6.1: a) and b) Known species and low-level impurities in the ^{19}F spectra of Figures 6.2 and 6.3, with chemical shifts and concentrations calculated from the known concentration of rosuvastatin; percentage intensities relative to the main signal are also shown.

As stated in Section 4.3.3, and demonstrated in Figures 6.2 and 6.3, the CHORUS sequences offer a valuable tool for impurity analysis, revealing low-level impurities.

^{13}C decoupling of ^{19}F can also be performed. Figure 6.4b shows a simple 90° excitation spectrum with ^{13}C decoupling acquired on a Varian VNMRS 500 MHz system at 298 K. ^{13}C was decoupled during the acquisition time using adiabatic inversion WURST2[91, 92] pulses of duration 2 ms and bandwidth of 10 kHz, with the default supercycle[93, 94] [t5, m4].

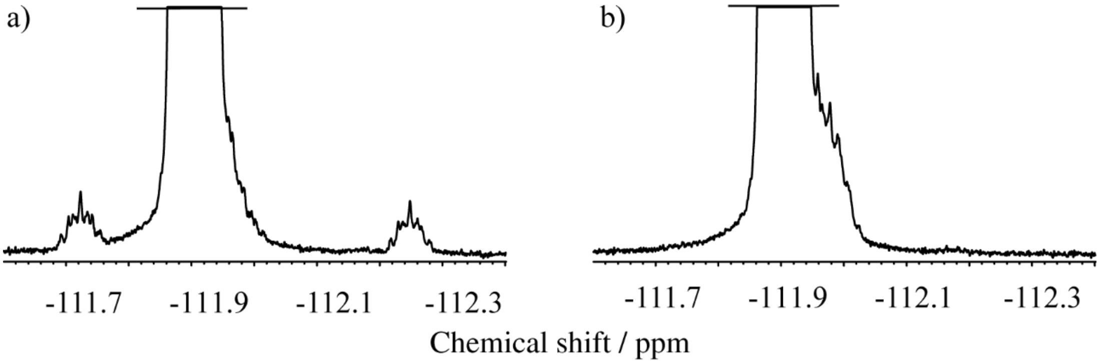

Figure 6.4: a) ^{19}F spectrum of rosuvastatin, showing the ^{13}C satellites either side of the main signal (see also Figure 6.1c). b) ^{13}C decoupled ^{19}F NMR spectrum of rosuvastatin. The data were processed with Gaussian weighting (Section 2.6.3) to give a linewidth at half-height of 3.3 Hz.

The resolution enhanced ^{13}C decoupled ^{19}F spectrum of Figure 6.4b shows the multiplet structure of the ^{13}C isotopomer signals to the right of the main peak. The ^{1}H-^{19}F multiplet structure can be supressed using simultaneous ^{1}H and ^{13}C decoupling.

6.2.3. Triple Resonance Experiment

Low-level impurity detection would best be achieved by performing $^{19}F\{^{1}H\}$ and $^{19}F\{^{13}C\}$ decoupling (Section 6.2.2) simultaneously; however, to do this most effectively and efficiently requires appropriate hardware. The data for the ^{1}H decoupled 1D and DOSY ^{19}F NMR spectra of Figures 6.2 and 6.3 were acquired using a Bruker

AVIII spectrometer, with a 5 mm BBO probe and QNP switch. This probe has only two frequency channels, where ^{1}H and ^{19}F use different channels but use the same amplifier for high-band frequency, i.e. the QNP switch allows switching between the two nuclei depending on the experimental setup. ^{19}F and ^{13}C, however, share the same channel (X channel) but have different amplifiers. Using this system does not allow for simultaneous doubly decoupling. As an alternative approach, a Varian system was used.

6.2.3.1. ^{19}F{^{1}H} Decoupling of Rosuvatsatin (Varian System)

For ^{19}F{^{1}H} double resonance using a triple resonance HCN triple axis gradient 5 mm probe, as used on the Varian VNMRS 500 MHz spectrometer, is problematic, since the probe has a single high frequency channel, which is shared by ^{19}F and ^{1}H nuclei. For the purpose of ^{19}F{^{1}H} decoupling, when the probe is tuned to ^{19}F, the spectrometer cannot produce sufficient RF amplitude (B_2) for full broadband ^{1}H decoupling. Figure 6.5 shows a schematic diagram of the high and low frequency channels, connected to the probe, in the Varian spectrometer, which allows the sharing of the high frequency channel between ^{1}H and ^{19}F.

Here it is shown that, using this probe, simultaneous ^{1}H irradiation and ^{19}F acquisition for decoupling was made possible by manipulation of the Varian software. The probeConnect parameter in the Varian software was changed from ‘H1 C13 N15’ to ‘F19 H1 C13’ and preAmpConfig from ‘hln’ to ‘hhn’, where ‘h’ represents high field, ‘l’ low field and ‘n’ not used. This allowed for time-sharing of the two nuclei, such that the transmitter and receiver of ^{1}H and ^{19}F were alternated, synchronized with acquisition of data points; the technique of time-sharing was first applied to homonuclear decoupling by Jesson and Meakin.[32]

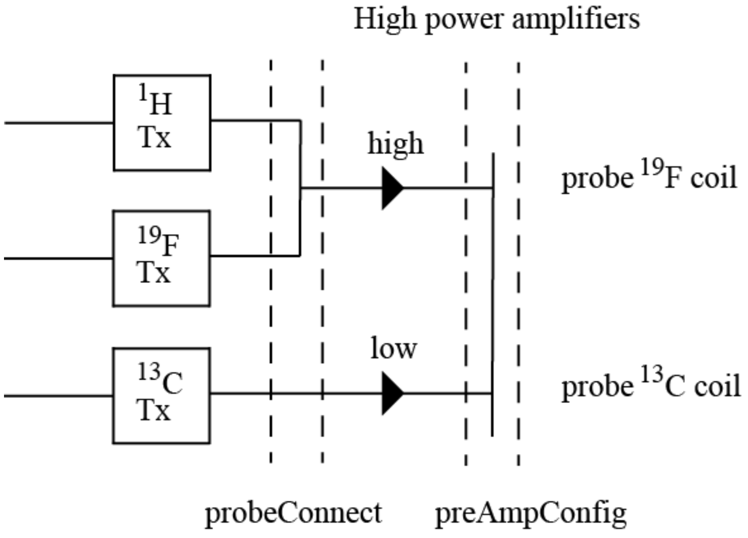

Figure 6.5: Schematic diagram of the high and low frequency channel connections for the transmitter nuclei ^{1}H, ^{19}F and ^{13}C to the NMR probe in the Varian VNMRS 500 MHz spectrometer, where ^{1}H and ^{19}F are both high frequency using the same channel and ^{13}C is low-frequency. The preAmpConfig parameter in the Varian software is changed to allow time-sharing of the nuclei such that the transmitter and receiver of ^{1}H and ^{19}F are alternated synchronized with acquisition of data points.

With the establishment of simultaneous ^{1}H irradiation and ^{19}F acquisition, a continuous sine-modulated waveform for ^{1}H decoupling was used. The advantage of a sine modulated waveform to decouple ^{19}F{^{1}H} is that less power can be used, since multiplication of a coherent decoupler output with a single frequency f_o by $\sin(2\pi f_1 t)$, decouples at two frequencies $f_o \pm f_1$, where the trigonometric identity Equation 6.1 applies. Therefore, the two aromatic protons coupled to the main fluorine signal of rosuvastatin (Figure 6.1a), can be simultaneously decoupled.

$$\sin(2\pi f_1 t) \times \sin(2\pi f_0 t) = \frac{1}{2}\left[\cos\left(2\pi(f_0 - f_1)t - \cos\left(2\pi(f_0 + f_1)t\right]\right.\right. \tag{6.1}$$

The modulation frequency f_1 required is different from the chemical shift difference $\Delta\nu$ because of the Bloch-Siegert[38] effect (Section 2.1). The two RF fields applied affect the nearby resonances such that they experience an increased effective field, with the resonances shifting away from the two decoupler frequencies.[38] With the successful $^{19}F\{^{1}H\}$ decoupling, a triple resonance experiment was performed.

6.2.3.1.1. Experimental

Two samples of rosuvastatin (4.3% w/w in DMSO-d_6) were prepared; one sample was fresh, the other prepared 3-4 months prior to use and stored in the refrigerator. ^{1}H and ^{19}F measurements were carried out, spinning, on a Varian VNMRS 500 MHz spectrometer at 298 K using simple 90° excitation, with 90° pulse widths of 11.8 µs and 14.3 µs respectively. The data were recorded using 16384 complex data points with a relaxation delay of 3.0 s between scans and a total experiment time of 15 s.

^{1}H was decoupled during acquisition using a continuous sine modulated waveform of modulation frequency 155 Hz, greater than the expected value of 109 Hz, which is half of the chemical shift difference in Hz, of the two proton resonances to be decoupled on the benzene ring, where the empirically optimized value is higher due to the Bloch Siegert effect.

^{13}C was decoupled during acquisition using adiabatic inversion WURST40 pulses,[33] of duration 1.4 ms and bandwidth of 25.137 kHz with the default supercycle[93, 94] (t5, m4). Inadvertently, incorrect parameters were chosen for the adiabatic decoupling. This had the effect of reducing decoupling to simple coherent decoupling; however, the results (Figures 6.7 and 6.8) still proved very satisfactory.

The transmitter offset was set on resonance for the fluorine signal (−111.91 ppm). The decoupler offset for ^{1}H was set at 7.47 ppm, midway between the two proton resonances on the benzene ring, H_{17} / H_{21} (7.703 ppm) and H_{18} / H_{20} (7.267 ppm). The decoupler offset for ^{13}C was set at 165.66 ppm, i.e. position C_{19} on the benzene ring.

6.2.3.1.2. Results and Discussion

Figure 6.6 shows the doubly decoupled ^{19}F spectrum of rosuvastatin, with both ^{1}H and ^{13}C decoupled from the main fluorine signal. The data were processed using a high vertical scale and Lorentz-to-Gauss transformation to enhance sensitivity and lineshape, giving a linewidth at half-height of 2.2 Hz. The relative intensities of different signals are listed in Table 6.2. An expansion of the crowded region at approximately −111.91 ppm shows the one-bond ^{13}C satellites ($^{1}J_{CF}$), which are unsymmetrical about the ^{19}F signal, collapse to form fluorine signal **A** at the mid-point of the satellites, at 0.9 % intensity of the parent peak (Table 6.2). Fluorine signal **B** is of intensity 2.3 % relative to the parent peak (Table 6.2), and is attributable to the collapse of long-range C-F couplings ($^{2}J_{CF}$), where the carbon coupling is assumed to be to the ortho position on the benzene ring.

In the expanded region of Figure 6.6, impurities **R2** and **R3** can be seen at approximately 0.2 % of the main signal intensity (Table 6.2); with increased vertical scale, impurity **R1** is revealed at 0.01% of the main signal intensity (Figure 6.6, Table 6.3).

Impurity **R2** was not detected in the ^{1}H decoupled 1D and DOSY ^{19}F NMR spectra of rosuvastatin, Figures 6.2 and 6.3 respectively (Section 6.2); the **R2** impurity is very close to the ^{13}C satellite at −111.73 ppm and maybe obscured from detection (assuming its concentration is lower than that of the ^{13}C satellites).

Impurity **R2** was detected in the ^{1}H decoupled CHORUS Oneshot ^{19}F DOSY spectra of sample 2 (Section 4.3.2.1, Figure 4.11b, Table 4.2), where the sample, containing rosuvastatin, was heat treated at 50 °C for three hours.

The impurity signals **R1**, **R2** and **R3** are *not* seen in the freshly prepared sample of Figure 6.8b; therefore, they presumably arise from degradation of rosuvastatin.

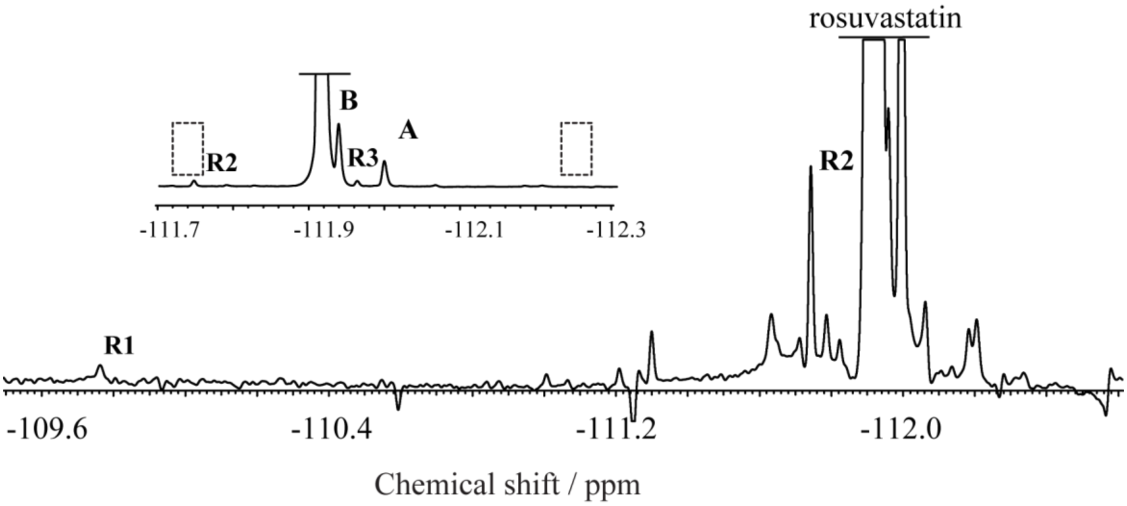

Figure 6.6: The doubly decoupled ^{19}F spectrum of rosuvastatin, with an expansion of the region around −111.91 ppm. The data were processed using a high vertical scale. The ^{13}C satellites ($^{1}J_{\mathrm{CF}}$) collapse (shown by empty dashed boxes) to form a fluorine signal **A** at the mid-point of the satellites. Fluorine signal **B** is attributed to the collapse of long-range C-F couplings ($^{2}J_{\mathrm{CF}}$), where the carbon atoms are assumed to be in the ortho position, on the benzene ring. In total three impurity signals are detected, **R1**, **R2** and **R3**.

Known Species	**Chemical Shift / ppm**	**% intensity**
Rosuvastatin	−111.91	100
A	−112.00	0.92
B	−111.94	2.28

Impurities	**Chemical Shift / ppm**	**% intensity**
R1	−109.76	0.01
R2	−111.74	0.21
R3	−111.96	0.19

Table 6.2: Known species and low-level impurities, **R1, R2** and **R3**, in the ^{19}F spectra of Figure 6.6, with chemical shifts and percentage intensities relative to the main signal.

6.2.3.1.3. Viewing Artefacts and Impurities Below the 0.1% Level

Figures 6.7 and 6.8 show the doubly decoupled spectra of rosuvastatin, with the same high vertical scale and weighting as that used for Figure 6.6. This allows the artefacts and impurities below the 0.1 % level to be seen more clearly, so that they can be analysed to see which of the signals may be real and which are artefactual.

Periodic decoupling waveforms can result in modulation sidebands, or artefacts, due to periodic changes of the signal amplitude (AM), frequency (FM) or phase (PM). Figures 6.7 and 6.8 show modulation artefacts in the spectra, where Figures 6.7a and 6.8a are the same.

Analysis of the artefacts show that DD′ (Figures 6.7a and 6.8a), which are symmetrical about the parent peak, are proton modulated, since the artefacts are separated by a frequency of 310 Hz, a sub-multiple of the ^{1}H decoupler modulation frequency (dmf = 15.5 kHz).

Artefacts EE′ (Figures 6.7a and 6.8a) and FF′ (Figure 6.8b), centred at the fluorine signal (A), which is at the mid-point of the one-bond ^{13}C satellites ($^{1}J_{CF}$), are ^{13}C modulated, since the artefacts are separated by frequencies of 328 Hz and 132 Hz respectively and are approximate sub-multiples of the ^{13}C decoupler modulation frequency (dmf = 30 kHz). Artefacts other than DD′, EE′ and FF′ can be seen in Figures 6.7a and 6.8a, however these are not present in Figures 6.7b and 6.8b, therefore are not real signals.

To confirm the artefacts assignments the parameter dmf was reduced by 3 % and 6 % for ^{1}H and ^{13}C respectively (Figure 6.7b). The artefacts DD′, EE′ and FF′ shift and no longer align with the artefacts in Figure 6.7a, confirming that these are artefacts.

To ascertain if the sample had degraded, data were acquired using the freshly made sample (Figure 6.8b). Impurities in Figure 6.7a, 6.7b and 6.8a are not present in Figure 6.8b. This suggests rosuvastatin has degraded over time.

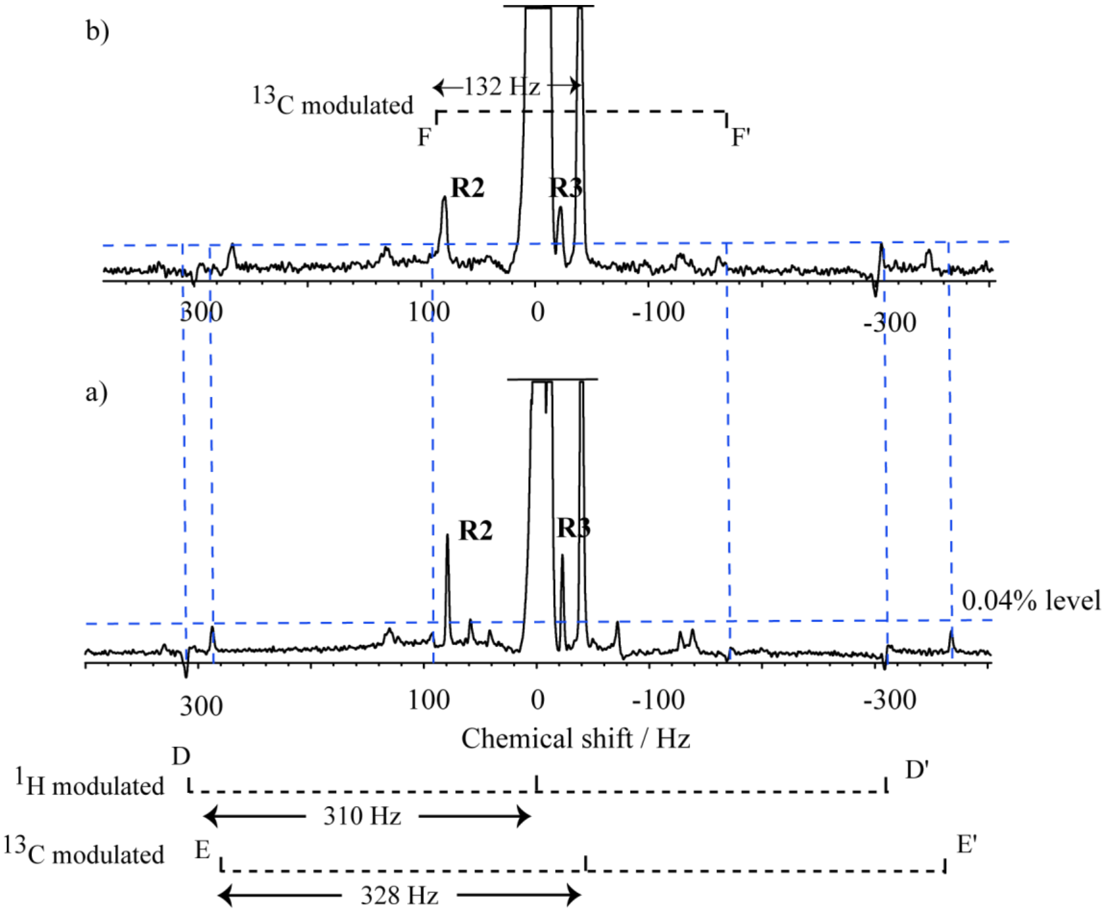

Figure 6.7: a) The doubly decoupled ^{19}F spectrum with high vertical scale and heavy weighting to show proton DD′ and carbon modulation artefacts EE′ and FF′; b) the doubly decoupled ^{19}F spectrum of rosuvastatin with dmf values reduced by 3 % and 6 % for ^{1}H and ^{13}C respectively; when comparing to a), frequency shifts in the artefacts DD′, EE′ and FF′ are observed.

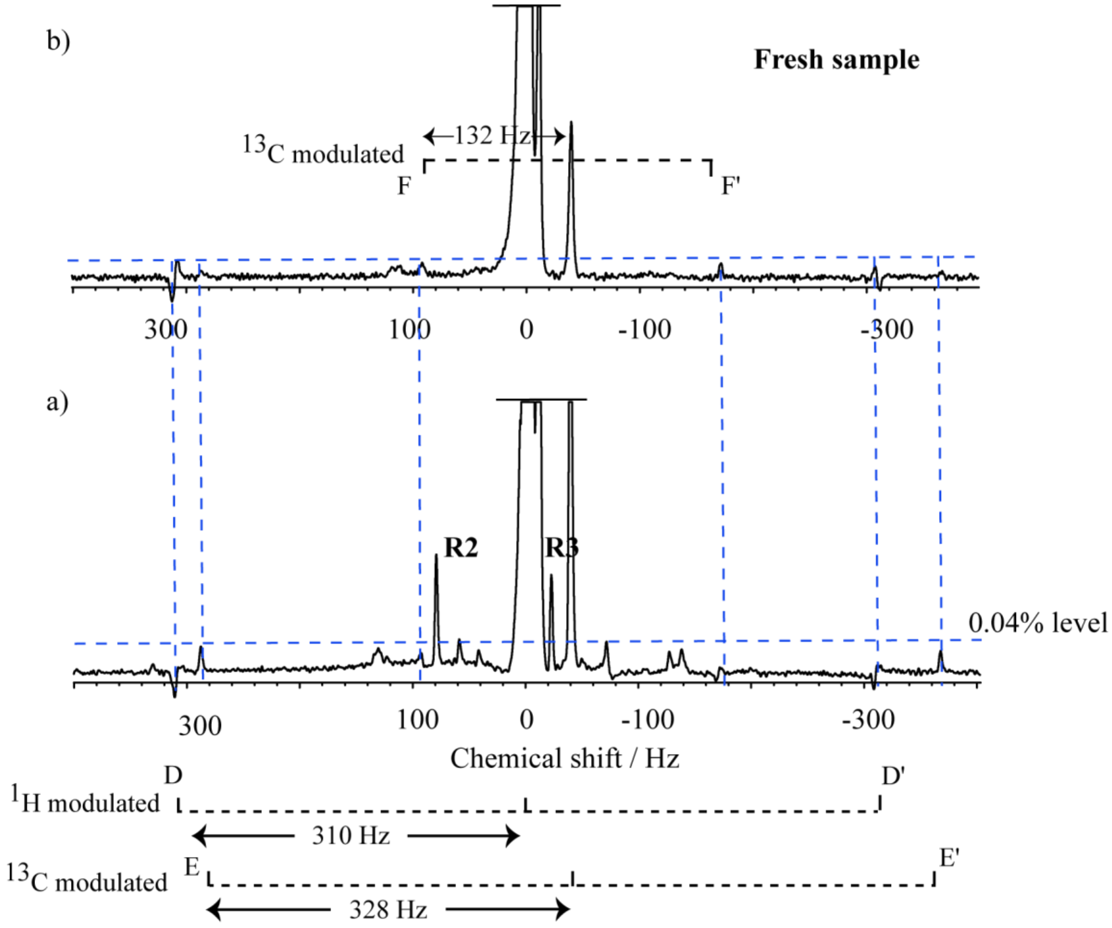

Figure 6.8: a) The doubly decoupled ^{19}F spectrum of rosuvastatin with a higher vertical scale to show proton and carbon modulation artefacts at DD′ and EE′ respectively; b) the doubly decoupled ^{19}F spectrum of rosuvastatin showing a carbon modulation artefact at FF′. For b) a fresh sample was used.

6.2.3.1.4. Conclusion

Double resonance and triple resonance experiments were performed on Bruker and Varian systems respectively. The ^{19}F{^{1}H} decoupling of rosuvastatin on the Bruker system, together with the newly developed CHORUS sequences (Sections 3 and 4), revealed two impurities **R1** and **R3** and low-level disturbances **d** (Figures 6.2 and 6.3, Table 6.1).

The doubly decoupled ^{19}F spectrum of rosuvastatin on the Varian system, using simple 90° excitation and a continuous sine modulated and adiabatic WURST40 decoupling waveforms for ^{1}H and ^{13}C respectively, revealed, in addition to **R1** and **R3**, a third impurity **R2**. This impurity, close to the chemical shift of the ^{13}C satellite (−111.73 ppm), may be obscured from detection in the double resonance experiments of Figures 6.2 and 6.3. **R2** was also detected in the heat-treated sample containing rosuvastatin of Figure 4.11b (Section 4.3.2.1, Table 4.2).

In addition to low-level impurity detection, the triple resonance experiments show modulation artefacts, which are shown to arise because of proton and carbon decoupling, at sub-multiples of the decoupler modulation frequencies (dmfs) (Figures 6.7 and 6.8).

The experiment was not easy to perform; since the probe was not resonant for ^{1}H, the low RF amplitude (B_2) was insufficient to decouple doubly ^{1}H fully. Hardware permitting, using a more suitable probe to allow simultaneous resonant irradiation of ^{1}H and ^{13}C, while tuned to ^{19}F, would allow a more reliable and efficient experiment to be performed. Such an experiment, combined with reference deconvolution (using SF_6 as a reference material, Section 5.2.3.3.4.3), should improve low-level impurity detection.

Chapter 7

References

7. References

1. Levitt, M.H., *Spin Dynamics: Basics of Nuclear Magnetic Resonance*. John Wiley & Sons, Chichester, West Sussex. 2001, pp.7-8.
2. Friedrich, B. and D. Herschbach, *Space quantization: Otto Stern's Lucky Star*. Daedalus, 1998, **127**, pp. 165-191.
3. Herschbach, D., *Molecular beams entwined with quantum theory: A bouquet for Max Planck.* Annalen der Physik (Leipzig), 2001, **10 (1-2)**, pp. 163-176.
4. Batelaan, H., T.J. Gay and J.J. Schwendiman, *Stern-Gerlach Effect for Electron Beams.* Physical Review Letters, 1997, **79(23)**, pp. 4517-4521.
5. Bloch, F., *Nuclear Induction.* Physical Review, 1946, **70 (7-8)**, pp. 460-474.
6. Purcell, E.M., H.C. Torrey and R.V. Pound, *Resonance absorption by nuclear magnetic moments in a solid.* Physical Review, 1946, **69 (1-2)**, pp. 37-38.
7. Levine, S.G., *A Short History of the Chemical Shift.* Journal of Chemical Education, 2001, **78**, p. 133.
8. Claridge, T.D.W., *High-Resolution NMR Techniques in Organic Chemistry*. 2nd Ed., 2009, **vol. 27**, pp. 1-2.
9. Keeler, J., *Understanding NMR Spectroscopy*. John Wiley & Sons, Chichester, West Sussex. 2nd Ed., 2010, p. 77.
10. Morris, G.A., *Diffusion-Ordered Spectroscopy* in *Encyclopedia of Nuclear Magnetic Resonance*. John Wiley & Sons Ltd., Chichester, 2009, pp. 515-524. DOI: 10.1002/9780470034590.emrstm0119.pub2.
11. Aue, W.P., E. Bartholdi and R.R. Ernst, *Two-dimensional spectroscopy. Application to nuclear magnetic resonance.* The Journal of Chemical Physics, 1976, **64 (5)**, pp. 2229-2246.

12. Szántay, C., *High-field NMR spectroscopy as an analytical tool for quantitative determinations: pitfalls, limitations and possible solutions.* Trends in Analytical Chemistry, 1992, **11(9)**, pp. 332-344.

13. Holzgrabe, U., *Quantitative NMR Spectroscopy in Pharmaceutical R&D* eMagRes, 2015, **4**, pp. 45-56.

14. Malz, F. and H. Jancke, *Validation of quantitative NMR.* Journal of Pharmaceutical and Biomedical Analysis, 2005, **38**, pp. 813-823.

15. Maniara, G., K. Rajamoorthi, S. Rajan and G.W. Stockton, *Method Performance and Validation for Quantitative Analysis by ^{1}H and ^{31}P NMR Spectroscopy. Applications to Analytical Standards and Agricultural Chemicals.* Analytical Chemistry, 1998, **70**, pp. 4921-4928.

16. Tannús, A. and M. Garwood, *Adiabatic pulses.* Nmr in Biomedicine, 1997, **10**, pp. 423-434.

17. Kupče, E. and R. Freeman, *Wideband Excitation with Polychromatic Pulses.* Journal of Magnetic Resonance 1994, **108**, pp. 268-273.

18. Kupče, E. and R. Freeman, *Stretched Adiabatic Pulses for Broadband Spin Inversion.* Journal of Magnetic Resonance, 1995, **117**, pp. 246-256.

19. Garwood, M. and L. DelaBarre, *The Return of the Frequency Sweep: Designing Adiabatic Pulses for Contemporary NMR.* Journal of Magnetic Resonance, 2001, **153**, pp. 155-177.

20. Böhlen, J.M., M. Rey and G. Bodenhausen, *Refocusing with chirped pulses for broadband excitation without phase dispersion.* Journal of Magnetic Resonance 1989, **84**, pp. 191-197.

21. Böhlen, J.M., I. Burghardt, R. Martial and G. Bodenhausen, *Frequency-modulated "Chirp" pulses for broadband inversion recovery in magnetic resonance.* Journal of Magnetic Resonance 1990, **90**, pp. 183-191.

22. Böhlen, M.J. and G. Bodenhausen, *Experimental Aspects of Chirp NMR Spectroscopy.* Journal of Magnetic Resonance, 1993, **102**, pp. 293-301.

23. Ermakov, V.L., J.M. Böhlen and G. Bodenhausen, *Improved Schemes for Refocusing with Frequency-Modulated Chirp Pulses.* Journal of Magnetic Resonance, 1993, **103**, pp. 226-229.

24. Ermakov, V. and G. Bodenhausen, *Broadband excitation in magnetic resonance by self-refocusing doubly frequency-modulated pulses.* Chemical Physics Letters, 1993, **204**, pp. 375-380.

25. Cano, K.E., M.A. Smith and A.J. Shaka, *Adjustable, Broadband, Selective Excitation with Uniform Phase.* Journal of Magnetic Resonance, 2002, **155**, pp. 131-139.

26. Power, J.E., M. Foroozandeh, R.W. Adams, M. Nilsson, S.R.Coombes, A.R. Phillips and G.A. Morris, *Increasing the quantitative bandwidth of NMR measurements.* Chemical Communications, 2016, pp. 2916-2919.

27. Evilia, R., *Quantitative NMR Spectroscopy.* Analytical Letters, 2001, **43(13)**, pp. 2227-2236.

28. Pelta, M.D., G.A. Morris, M.J. Stchedroff and S.J. Hammond, *A one-shot sequence for high-resolution diffusion-ordered spectroscopy.* Magnetic Resonance in Chemistry, 2002, **40**, pp. S147-S152.

29. Morris, G.A., *Compensation of instrumental imperfections by deconvolution using an internal reference signal.* Journal of Magnetic Resonance, 1988, **80 (3)**, pp. 547-552.

30. Morris, G.A., H. Barjat and T.J. Horne, *Reference deconvolution methods.* Progress in Nuclear Magnetic Resonance Spectroscopy, 1997, **31**, pp. 197-257.

31. Morris, G.A., *Reference Deconvolution* in *Encyclopedia of Nuclear Magnetic Resonance*. ed. D.M. Grant and R.K. Harris, John Wiley & Sons Ltd., Chichester, 2002, **9**, pp. 125-131. DOI: 10.1002/9780470034590.emrstm0449.

32. Jesson, J.P. and P. Meakin, *Homonuclear Decoupling and Peak Elimination in Fourier Transform Nuclear Magnetic Resonance.* Journal of Magnetic Resonance, 1972, **6**, p. 670.

33. Kupče, E. and R. Freeman, *Adiabatic Pulses for Wideband Inversion and Braodband Decoupling.* Journal of Magnetic Resonance Series A, 1995, **115**, pp. 273-276.

34. Friebolin, H., *Basic One - and Two - Dimensional NMR Spectroscopy.* Wiley VCH, 4th Ed., 2008, pp. 1-6.

35. Levitt, M.H., *Spin Dynamics: Basics of Nuclear Magnetic Resonance.* John Wiley & Sons, Chichester, West Sussex. 2001, pp. 9-24.

36. Keeler, J., *Understanding NMR Spectroscopy.* John Wiley & Sons, Chichester, West Sussex. 2nd Ed., 2010, pp. 47-57.

37. Keeler, J., *Understanding NMR Spectroscopy.* John Wiley & Sons, Chichester, West Sussex. 2nd Ed., 2010, pp. 489-490.

38. Bloch, F. and A. Siegert, *Magnetic Resonance for Nonrotating Fields.* Physical Review, 1940, **57 (6)**, pp. 522-527.

39. Hore, P.J., *Nuclear Magnetic Resonance*. Oxford University Press. 1995, pp. 8-10.

40. Levitt, M.H., *Spin Dynamics: Basics of Nuclear Magnetic Resonance.* John Wiley & Sons, Chichester, West Sussex. 2001, pp. 203-204.

41. Keeler, J., *Understanding NMR Spectroscopy.* John Wiley & Sons, Chichester, West Sussex. 2nd Ed., 2010, pp. 242-317.

42. Friebolin, H., *Basic One - and Two - Dimensional NMR Spectroscopy.* Wiley VCH, 4th Ed., 2008, pp. 171-178.

43. Hore, P.J., *Nuclear Magnetic Resonance.* Oxford University Press. 1995, p. 27 & pp. 65-66.

44. Hahn, E.L., *Spin Echoes.* Physical Review 1950, **80(4)**, 850-594.

45. Meiboom, S. and D. Gill, *Modified Spin-Echo Method for Measuring Nuclear Relaxation Times.* Review of Scientific Instruments, 1958, **29**, pp. 688-691.

46. Keeler, J., *Understanding NMR Spectroscopy.* John Wiley & Sons, Chichester, West Sussex. 2nd Ed., 2010, pp. 83-101.

47. Claridge, T.D.W., *High-Resolution NMR Techniques in Organic Chemistry.* 2nd Ed., 2009, **vol. 27**, pp. 40-44.

48. Keeler, J., *Understanding NMR Spectroscopy.* John Wiley & Sons, Chichester, West Sussex. 2nd Ed., 2010, pp.5-46.

49. Keeler, J., *Understanding NMR Spectroscopy.* John Wiley & Sons, Chichester, West Sussex. 2nd Ed., 2010, pp. 105-187.

50. Sørensen, O.W., G.W. Eich, M. H. Levitt, G. Bodenhausen and R.R. Ernst, *Product Operator-Formalism for the Description of NMR Pulse Experiments.* Progress in Nuclear Magnetic Resonance Spectroscopy, 1983, **16**, pp. 163-192.

51. Keeler, J., *Understanding NMR Spectroscopy*. John Wiley & Sons, Chichester, West Sussex. 2nd Ed., 2010, pp. 381-439.

52. Bodenhausen, G., R. Freeman and D.L. Turner, *Suppression of Artifacts in 2-Dimensional J Spectroscopy.* Journal of Magnetic Resonance, 1977, **27**, pp. 511-514.

53. Connell, M.A., P.J. Bowyer, P.A. Bone, A.L. Davis, A.G. Swanson, M. Nilsson and G.A. Morris, *Improving the accuracy of pulsed field gradient NMR diffusion*

experiments: Correction for gradient non-uniformity. Journal of Magnetic Resonance, 2009, **198**, pp. 121-131.

54. Einstein, A., *Investigations on the Theory of the Brownian Movement*. ed. R. Furth, Dover Publications, Inc., Mineola, N.Y., 1956, pp. 1-25.

55. Price, W.S., *Pulsed-Field Gradient Nuclear Magnetic Resonance as a Tool for Studying Translational Diffusion: Part 1. Basic Theory.* Concepts in Magnetic Resonance, 1997, **9**, pp. 299-336.

56. Stejskal, E.O. and J.E. Tanner, *Spin Diffusion Measurements: Spin Echoes in the Presence of a Time-Dependent Field Gradient.* The Journal of Chemical Physics, 1965, **42**, pp. 288-292.

57. Pelta, M.D., H. Barjat, G.A. Morris, A.L. Davis and S.J. Hammond, *Pulse sequences for high-resolution diffusion-ordered spectroscopy (HR-DOSY).* Magnetic Resonance in Chemistry, 1998, **36**, pp. 706-714.

58. Tanner, J.E., *Use of the Stimulated Echo in NMR Diffusion Studies.* The Journal of Chemical Physics, 1970, **52**, pp. 2523-2526.

59. Tycko, R., H.M. Cho, E. Schneider and A. Pines., *Composite pulses without phase distortion.* Journal of Magnetic Resonance 1985, **61**, pp. 90-101.

60. Freeman, R., S.P. Kempsell, and M.H. Levitt, *Radiofrequency Pulse Sequences Which Compensate Their Own Imperfections.* Journal of Magnetic Resonance, 1980, **38**, pp. 453-479.

61. Hwang, T.L., P. C. M. van Zijl and M. Garwood, *Broadband Adiabatic Refocusing without Phase Distortion.* Journal of Magnetic Resonance, 1997, **124**, pp. 250-254.

62. Odedra, S. and S. Wimperis, *Use of composite refocusing pulses to form spin echoes.* Journal of Magnetic Resonance, 2012, **214**, pp. 68-75.

63. Hardy, C.J., W.A. Edelstein and D. Vatis, *Efficient Adiabatic Fast Passage for NMR Population Inversion in the Presence of Radiofrequency Field Inhomogeneity and Frequency offsets.* Journal of Magnetic Resonance, 1986, **66**, pp. 470-482.

64. Baum, J., R. Tycko and A. Pines, *Broadband and adiabatic inversion of a two-level system by phase-modulated pulses.* Physical Review A, 1985, **32(6)**, pp. 3435-3446.

65. Norris, G., *Adiabatic Radiofrequency Pulse Forms in Biomedical Nuclear Magnetic Resonance.* Concepts in Magnetic Resonance, 2002, **14(2)**, pp. 89-101.

66. Silver, M. and R.I. Joseph, *Selective spin inversion in nuclear magnetic resonance and coherent optics through an exact solution of the Bloch-Riccati equation.* Physical Review A, 1985, **31(4)**, pp. 2753-2755.

67. Baum, J., R. Tycko and A. Pines, *Broadband population inversion by phase modulated pulses.* The Journal of Chemical Physics, 1983, **79**, pp. 4643-4644.

68. Emsley, L. and G. Bodenhausen, *Phase Shifts Induced by Transient Bloch-Siegert Effects in NMR.* Chemical Physics Letters, 1990, **168**, pp. 297-303.

69. Keeler, J., *Understanding NMR Spectroscopy*. John Wiley & Sons, Chichester, West Sussex. 2nd Ed., 2010, pp. 403-407.

70. Kovacs, H., D. Moskau and M. Spraul, *Cryogenically cooled probes - a leap in NMR technology.* Progress in Nuclear Magnetic Resonance Spectroscopy, 2005, **46**, pp. 131-155.

71. Krishnan, V.V. and N. Murali, *Radiation damping in modern NMR experiments: Progress and challenges.* Progress in Nuclear Magnetic Resonance Spectroscopy, 2013, **68**, pp. 41-57.

72. Johnson, C.S., *Diffusion ordered nuclear magnetic resonance spectroscopy: principles and applications.* Progress in Nuclear Magnetic Resonance Spectroscopy, 1998, **34**, pp. 203-256.

73. Antalek, B., *Using Pulsed Gradient Spin Echo NMR for Chemical Mixture Analysis: How to Obtain Optimum Results.* Concepts in Magnetic Resonance, 2002, **14**, pp. 225-258.

74. Morris, G.A., *Diffusion-Ordered Spectroscopy* in *Encyclopedia of Nuclear Magnetic Resonance. eMagRes*, ed. D.M. Grant and R.K. Harris, John Wiley & Sons Ltd., Chichester, 2009. DOI: 10.1002/9780470034590.emrstm0119.pub2.

75. Nilsson, M. and G.A. Morris, *Pure shift proton DOSY: diffusion-ordered* ^{1}*H spectra without multiplet structure.* Chemical Communications, 2007, pp. 933-935.

76. Aguilar, J.A., S. Faulkner, M. Nilsson and G.A. Morris, *Pure Shift* ^{1}*H NMR: A Resolution of the Resolution problem.* Angewandte Chemie, 2010, **49**, pp. 3901-3903.

77. Barjat, H., G.A. Morris and A.G. Swanson, *A Three-Dimensional DOSY-HMQC Experiment for the High-Resolution Analysis of Complex Mixtures.* Journal of Magnetic Resonance, 1998, **131**, pp. 131-138.

78. Nilsson, M., A.M. Gil, I. Delgadillo and G.A. Morris, *Improving Pulse Sequences for 3D Diffusion-Ordered NMR Spectroscopy: 2DJ-IDOSY.* Analytical Chemistry, 2004, **76**, pp. 5418-5422.

79. Newman, J.M. and A. Jerschow, *Improvements in Complex Mixture Analysis by NMR: DQF-COSY iDOSY.* Analytical Chemistry, 2007, **79**, pp. 2957-2960.

80. Wu, D., A. Chen and C.S. Johnson, *Heteronuclear-Detected Diffusion-Ordered NMR Spectroscopy through Coherence Transfer.* Journal of Magnetic Resonance, 1996, **123**, pp. 215-218.

81. Li, D., R. Hopson, W. Li, J. Liu and P.G. Willard, *^{13}C INEPT Diffusion-Ordered NMR Spectroscopy (DOSY) with Internal References.* Organic Letters, 2008, **10**, pp. 909-911.

82. Botana, A., P.W.A. Howe, V. Caër, G.A. Morris and M. Nilsson, *High Resolution ^{13}C DOSY: The DEPTSE experiment.* Journal of Magnetic Resonance, 2011, **211**, pp. 25-29.

83. Botana, A., J.A. Aguilar, M. Nilsson and G.A. Morris, *J-modulation effects in DOSY experiments and their suppression: The Oneshot45 experiment.* Journal of Magnetic Resonance, 2011, **208**, pp. 270-278.

84. Anet, F.A.L. and M. Kopelevich, *Ultrahigh Resolution in Proton NMR Spectra at 500 MHz: Two-Bond Intrinsic Chlorine and Silicon Isotope Effects.* Journal of the American Chemical Society, 1987, **109**, pp. 5870-5871.

85. Kumar, P. and B. Imam, *Footprints of air pollution and changing environment on the sustainability of built infrastructure.* Science of the Total Environment, 2013, **444**, pp. 85-101.

86. Hesse, P.J., R. Battino, P. Scharlin and E. Wilhelm, *Solubility of Gases in Liquids. 20. Solubility of He, Ne, Ar, Kr, N_2, O_2, CH_4 and SF_6 in n-Alkanes n-C_lH_{2l+2} ($6 \leq l \leq 16$) at 298.15 k.* Journal of Chemical and Engineering Data, 1996, **41**, pp. 195-201.

87. Pardo, J., M.C. López, J. Santafé, F.M. Royo and J.S. Urieta, *Solubility of gases in butanols II. Solubilities of nonpolar gases in 2-methyl-1-propanol from 263.15 to 303.15 K at 101.33 kPa partial pressure of gas.* Fluid Phase Equilibria, 1996, **119**, pp. 165-173.

88. Terrado, E.M., J.I. Pardo, J.S. Urieta and A.M. Mainar, *Solubilities of Nonpolar Gases in Dimethyl Carbonate and Diethyl Carbonate.* Journal of Chemical and Engineering Data, 2005, **50**, pp. 512-516.

89. Wilhelm, E., R. Battino and R.J. Wilcock, *Low-pressure Solubility of Gases in Liquid Water.* Chemical Reviews, 1977, **77(2)**, pp. 219-262.

90. Shaka, A.J., J. Keeler, T. Frenkiel and R. Freeman, *An Improved Sequence for Broadband Decoupling: WALTZ-16.* Journal of Magnetic Resonance, 1983, **52**, pp. 335-338.

91. Kupče, E. and G. Wagner, *Wideband Homonuclear Decoupling in Protein Spectra.* Journal of Magnetic Resonance, 1995, **109**, 329-333.

92. Kupče, E. and R. Freeman, *Optimized Adiabatic Pulses for Wideband Spin Inversion.* Journal of Magnetic Resonance, 1996, **118**, pp. 299-303.

93. Tycko, R., A. Pines and J. Guckenheimer, *Fixed point theory of iterative excitation schemes in NMR.* The Journal of Chemical Physics, 1985, **83**, pp. 2775-2802.

94. Levitt, M.H. and R. Freeman, *Composite Pulse Decoupling.* Journal of Magnetic Resonance, 1981, **43**, pp. 502-507.

Chapter 8

Appendices

8. Appendices

Appendix A: Increasing the quantitative bandwidth of NMR measurements (published paper)

J. E. Power, M. Foroozandeh, R. A. Adams, M. Nilsson, S. R. Coombes, A. R. Phillips and G. A. Morris. *Chem. Commun.*, 2016, **52**, pp. 2916-2919

DOI: 10.1039/c5cc10206e

ChemComm

COMMUNICATION

Cite this: *Chem. Commun.*, 2016, **52**, 2916

Received 11th December 2015, Accepted 14th January 2016

DOI: 10.1039/c5cc10206e

www.rsc.org/chemcomm

Increasing the quantitative bandwidth of NMR measurements†

J. E. Power,[a] M. Foroozandeh,[a] R. W. Adams,[a] M. Nilsson,[a] S. R. Coombes,[b] A. R. Phillips[b] and G. A. Morris*[a]

The frequency range of quantitative NMR is increased from tens to hundreds of kHz by a new pulse sequence, CHORUS. It uses chirp pulses to excite uniformly over very large bandwidths, yielding accurate integrals even for nuclei such as ^{19}F that have very wide spectra.

^{19}F NMR is widely used by chemists in the analysis of fluorinated drugs and their impurities. Typical drugs have only one or two fluorine atoms, but many protons. Thus in comparison to ^{1}H NMR, ^{19}F NMR offers spectra of greatly reduced complexity, simplifying interpretation while retaining high sensitivity. Quantitative analysis using ^{19}F, and other nuclei such as ^{13}C that have wide chemical shift ranges, requires constant amplitude and constant phase (more strictly, phase with a linear offset dependence) broadband excitation over the full spectral width. This is problematic, since due to the limited radiofrequency power available for pulsed excitation, resonance offset effects distort both signal intensities and signal phases and seriously degrade the accuracy of signal integration.

The scale of the problem can be seen by comparison of the loss in signal intensity towards the edges of the frequency range for narrow bandwidth quantitative experiments (^{1}H, ±5 ppm) and for much wider bandwidths (^{19}F, ±300 ppm). On a 500 MHz spectrometer using a 12.5 μs 90° pulse width, the losses are respectively negligible, and almost total (98%). Accurate (±1–2%) quantification with a 90° pulse is restricted to a relatively narrow range of frequencies, about 20 kHz.

In order to circumvent resonance offset effects, current practice in quantifying ^{19}F spectra[1] is to make a separate measurement for each different region of a spectrum, using a different quantitation standard with an appropriate chemical shift in each case. This is cumbersome, and it can be difficult to find appropriate standards due to problems such as sample instability, insolubility of quantitation standards in the solvent used, and signal overlap between analyte and standard. It would be greatly preferable to find a way to achieve quantitative excitation over the full chemical shift range.

To overcome pulse imperfections and improve the bandwidth of excitation, a variety of composite pulse methods have been developed.[2–7] However even the best of these methods fall well short of the bandwidths required. Pulse sequences generated by optimal control algorithms give more effective results, with small phase errors ($<2^\circ$) over ±20 kHz, *e.g.* BEBOP[8,9] and the calibration-free phase modulated sequence PM-BEBOP;[10] however, these methods have yet to be applied to the much wider spectral widths encountered here.

A much larger improvement in excitation bandwidth can be obtained through the use of swept-frequency pulses.[5,11–19] In such pulses the transmitter frequency is rapidly swept over a wide range during the pulse, allowing full signal amplitude to be excited far off resonance even with modest radiofrequency (RF) power. The big disadvantage of such pulses is that the phase of the excitation they produce varies very rapidly, and in a nonlinear fashion, with resonance offset. Much of this phase variation can be refocused by combining 90° and 180° swept-frequency pulses of appropriate relative duration and amplitude[14,17,19] (see ESI,† Fig. S2a), but the remaining signal phase error still varies in a nonlinear fashion with frequency so that less than half of the excitation range is usable (see ESI,† Fig. S2b). Using a nonlinear frequency sweep can improve the phase performance,[17] but there is a further, and less obvious, problem with such double swept-frequency pulse excitation sequences, which is that the signal phase is extremely sensitive to B_1 amplitude.[19] As a result, B_1 inhomogeneity causes large ($>30\%$) losses in signal even with modern probes (see ESI,† Fig. S2b).

In a notably elegant analysis,[19] Cano *et al.* have shown that the problem of the B_1 sensitivity of the double swept-frequency pulse sequence can be solved by the interpolation of a further 180° element, with a duration equal to that of the 90° pulse, to

---

[a] *School of Chemistry, University of Manchester, Oxford Road, Manchester M13 9PL, UK. E-mail: g.a.morris@manchester.ac.uk*

[b] *Pharmaceutical Development, AstraZeneca, Silk Road Business Park, Macclesfield, SK10 2NA, UK*

† Electronic supplementary information (ESI) available. See DOI: 10.1039/c5cc10206e

give the double echo ABSTRUSE (Adjustable, Broadband, Sech/Tanh-Rotation Uniform Selective Excitation) sequence. The ABSTRUSE sequence was derived with the aim of providing a rectangular excitation spectrum, with uniform signal phase and a rapid drop in excitation outside the passband. As the name implies, it is based on hyperbolic secant ("HS" or "sech/tanh") swept-frequency pulses.[20] These have the desirable property of giving close to uniform phase excitation "out of the box" in the double echo, with small phase errors that can be cancelled by co-adding the results of experiments with opposite frequency sweep directions.

The attractive features of the hyperbolic secant pulse for band-selective excitation – a rapid transition between full and zero excitation, and approximate phase uniformity – are not compatible with the aim of exciting very wide bandwidths quantitatively. This requires the best possible phase properties and the widest possible excitation for a given limit on peak radiofrequency power. However, the ABSTRUSE logic can be applied, with one important proviso, to any swept-frequency pulse shape. Where maximum bandwidth for a given duration is the overriding aim, a logical choice of pulse shape is the simple chirp pulse of Bodenhausen *et al.*,[14–18] leading to a pulse sequence of the form of Fig. 1a. The chirp pulse has uniform RF amplitude, except for smoothed ends, and therefore spreads RF power uniformly over almost the full frequency range. The important proviso is that a basic chirp pulse does not share the benign phase characteristics of the hyperbolic secant pulse, and it is therefore necessary to correct the residual nonlinear dependence of signal phase on excitation frequency.

This problem of phase variation with frequency can be dealt with by exploiting the one-to-one correspondence between time and frequency in a chirp pulse, which means that a small change in the phase of the pulse at a given time translates to an equal change in phase at the corresponding frequency. Thus calculating the residual phase error as a function of excitation frequency, fitting to a polynomial, and applying the equivalent time-dependent phase correction to the first and second pulses of Fig. 1a (see ESI,† Section S3), leads to a final sequence that achieves constant-phase excitation over a very wide bandwidth, as shown in Fig. 1b. For this CHORUS (CHirped, ORdered pulses for Ultra-broadband Spectroscopy; Fig. 1b) variant on the ABSTRUSE sequence, the experimental data (red dots) shows a very small but discernible asymmetry. This is due to T_2 relaxation, since a heavily doped sample of C_6F_6 of a short T_2 of 0.05 s was used. The size of this error is an artefact of the measurement method; for practical analytes (Fig. 2), the effect is much smaller, and can be reduced further by alternating the sweep direction of the chirp pulses during time averaging.[19]

The triple chirp pulse sequence, CHORUS, achieves constant amplitude excitation with constant phase over a 250 kHz bandwidth using a maximum RF amplitude of only 15 kHz, less than that of a typical hard 90° pulse, and shows no undue B_1 sensitivity. For a given RF amplitude, the frequency range over which CHORUS achieves 98% excitation is 5.8 times greater than that for a hard 90° pulse of the same peak RF amplitude, and 4.2 times greater than that for ABSTRUSE (see ESI,† Fig. S4c and d), in both cases after applying the necessary phase correction.

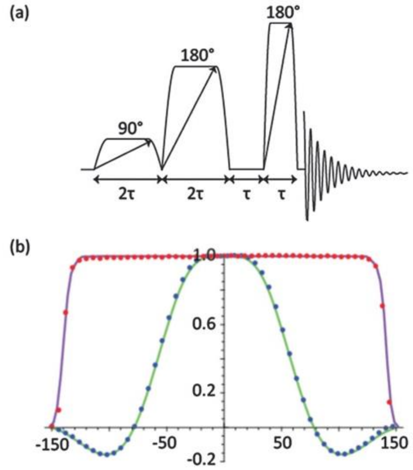

Fig. 1 (a) Pulse sequence for CHORUS (CHirped, ORdered pulses for Ultra-broadband Spectroscopy), for B_1-insensitive, broadband, constant-phase excitation. Pulse amplitudes are in the ratio 1 : 0.71 : 0.21, and for best results a 16-step phase cycle (see ESI,† Section S7) should be used. (b) Experimental and calculated ^{19}F excitation profiles for CHORUS (red dots) and simple 90° excitation (blue dots) using a sample of heavily doped C_6F_6 at 470 MHz with a 90° pulse width of 12.4 μs, corresponding to an RF amplitude of 20.2 kHz. The slight asymmetry (red dots) is caused by the very rapid relaxation (T_2 = 0.05 s). For CHORUS the unit pulse duration τ was 1 ms, chirp frequency range 300 kHz, and RF amplitude 15 kHz; a 64 step phase cycle was used. The frequency of excitation was varied in 6 kHz steps over 300 kHz; the receiver was kept on resonance to eliminate bias caused by the receiver filters. Simulations for CHORUS (purple line) and 90° pulse (green line) were carried out in Mathematica v.9 using compiled analytical solutions of the Bloch equations. For 90° excitation, both experiment and simulation used linearly frequency-dependent phase correction; no correction was needed for CHORUS. Full raw experimental data, pulse sequence code, pulse shape files and analysis software can be downloaded from DOI: 10.15127/1.276417 and DOI: 10.15127/1.276419.

To assess the utility of CHORUS for quantification, tests of repeatability over time and robustness with respect to offset from resonance were made using a sample containing bicalutamide, which has two signals with very different chemical shifts, and the reference material 4-fluoroaniline in DMSO-d_6. $^{19}F\{^1H\}$ data were acquired with 16 scans over a spectral width of 234 ppm (see ESI,† Fig. S5). To test repeatability, two series of thirty spectra of the same sample were acquired consecutively with the spectrometer operating frequency fixed at −100 ppm (see ESI,† Tables S1, S2 and Fig. S6a, b). To test robustness, the spectrometer operating frequency was varied from −20 ppm to −165 ppm, in steps of 5 ppm, to give thirty experiments, with three repetitions (see ESI,† Table S3a–c, and Fig. S7a–c). The percentage relative standard deviations (% RSDs) of the ratios of the integrals of the three peaks in the two tests are shown in Table 1. The repeatability test was carried out on resonance, so is unaffected by any systematic bias introduced by analogue

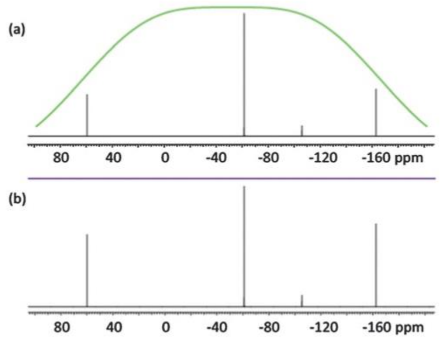

Fig. 2 470 MHz ^{19}F NMR spectra of a sample containing bicalutamide, SF_6 and C_6F_6 acquired using (a) simple 90° excitation and (b) CHORUS, with simulated excitation profiles in green and purple respectively. For simple 90° excitation, simulation and experiment used a linearly frequency-dependent phase correction. The difference in frequency between the most and least shielded resonances is 104 kHz.

Table 1 Percentage relative standard deviations (% RSDs) for the ratios of the integrals of peaks (1 : 2), (1 : 3) and (2 : 3), for a sample of bicalutamide (peaks 1 and 2, at −61.0 ppm and −105.4 ppm, respectively) and reference material 4-fluoroaniline (peak 3 at −129.8 ppm) in DMSO-d_6 (see ESI, Fig. S5). The results for repeatability shown here are for the spectrometer operating frequency set at −100 ppm, and for robustness, the first of the three repetitions. For robustness, the data are shown with and without correction for the effects of the analogue and digital receiver filters on signal amplitude

	Peaks (1 : 2) (%)	Peaks (1 : 3) (%)	Peaks (2 : 3) (%)
Repeatability	0.076	0.028	0.078
Robustness	0.14	0.22	0.12
Robustness (receiver-corrected)	0.070	0.024	0.065

and digital filtration of the signal received, but the robustness test varied the frequencies of the signals measured and hence is affected by the receiver characteristic. Correcting this small fixed error, which shows a quadratic dependence on offset (see ESI,† Fig. S9a and b) leads to a small improvement in the robustness RSD.

A common criterion for the acceptability of an analytical method in the pharmaceutical industry is an RSD ≤ 1%. The % RSDs for both measures of performance obtained with CHORUS are more than an order of magnitude better than this; the very small variations in signal integral that are seen include contributions from noise (lower in the case of the ratio of the two strongest signals, 1 and 3) and from systematic errors caused by environmental factors such as air conditioning. The results show that any contribution from resonance offset effects over the range tested is below the detection limit for these experiments: in other words, well over 99.8% excitation was achieved over the 145 ppm range of offsets used. The linearity of the method was not tested, but the performance of CHORUS should be no different in this respect from that of other NMR excitation methods, since the effect of sample concentration on RF amplitude and phase should be negligible over the concentration range of interest. The influence of such factors such as signal digitisation and signal-to-noise ratio is already well characterised and again their effect on CHORUS spectra should be identical to that on other NMR quantitation methods.

Fig. 2 compares hard pulse and CHORUS ^{19}F spectra of a sample of bicalutamide (15 mM) in DMSO-d_6, with two reference materials, SF_6 and C_6F_6, giving a wide chemical shift range of 221 ppm (104 kHz). Simulated excitation profiles are superimposed, to show the signal attenuation off resonance that results when a 90° hard pulse is used. The narrow quantitative range for simple 90° excitation is evident, with large losses in signal amplitude seen towards the edges of the frequency range. CHORUS, however, has a much wider usable range, of more than 500 ppm, which extends well beyond the spectral width shown here.

One important limitation of CHORUS (and of its parent ABSTRUSE) is that its relatively long duration leaves it vulnerable to *J*-modulation if large homonuclear couplings are present. This can be seen in the case of a sample of sodium perfluorooctanoate (NaPFO) in DMSO-d_6, where the 6 ms duration of the CHORUS sequence used is long enough for significant evolution under the ^{19}F–^{19}F couplings in the PFO anion, leading to distorted multiplets and reduced integrals (see ESI,† Fig. S8a and b). Analytes of this nature, therefore, are less easy to quantify using CHORUS. A further limitation is that the relatively long duration leads to small losses due to spin–spin relaxation. In both cases it should be possible to improve performance by optimising the sequence, for example using overlapping chirp pulses and/or optimal control theory[8,9] to reduce its duration.

The ABSTRUSE sequence is highly effective at providing pure phase band-selective excitation, and in this role requires no phase correction. In its original form it is however not ideally suited to quantitative excitation of the sorts of spectra described here, first because the hyperbolic secant waveform does not make optimum use of the RF power available, and second because the residual phase errors as a function of frequency reduce excitation slightly towards the edges of the band when opposed sweep acquisitions are combined. Changing from hyperbolic secant to simple chirp pulses sacrifices the appealing simplicity of ABSTRUSE, requiring that time-dependent phase correction be applied to one or more of the component pulses, but allows very accurate constant-amplitude and constant-phase excitation to be achieved over much wider bandwidths.

This CHORUS variant of ABSTRUSE offers a new approach to accurate NMR quantification that for many samples offers a great improvement over the conventional use of a simple 90° pulse. CHORUS uses standard instrumentation and shows excellent reproducibility and robustness in the measurement of signal integrals over very wide frequency ranges (>500 ppm for ^{19}F at 470 MHz). The radiofrequency energy deposited per transient is still relatively low, so sample heating is not a problem and CHORUS can allow wider bandwidths for excitation than are generally practical for heteronuclear decoupling. All broadband sequences have to address the limitations imposed by resonance offset effects and, to a greater or lesser extent, B_1 inhomogeneity; with the sequence structure introduced with ABSTRUSE and the phase correction added in CHORUS, these limitations are overcome for quantitative excitation. Even greater proportional improvements in bandwidth can result when the same principles are applied to multiple pulse sequences.

This work was funded by the Engineering and Physical Sciences Research Council (grant numbers EP/L018500 and EP/M013820) and by an Industrial CASE award from AstraZeneca and the EPSRC.

Notes and references

1 U. Holzgrabe, *eMagRes*, 2015, **4**, 45–56.
2 R. Tycko, H. M. Cho, E. Schneider and A. Pines, *J. Magn. Reson.*, 1985, **61**, 90–101.
3 R. Freeman, S. P. Kempsell and M. H. Levitt, *J. Magn. Reson.*, 1980, **38**, 453–479.
4 T. L. Hwang, P. C. M. van Zijl and M. Garwood, *J. Magn. Reson.*, 1997, **124**, 250–254.
5 A. Tannús and M. Garwood, *NMR Biomed.*, 1997, **10**, 423–434.
6 S. Odedra and S. Wimperis, *J. Magn. Reson.*, 2012, **214**, 68–75.
7 S. Odedra, M. J. Thrippleton and S. Wimperis, *J. Magn. Reson.*, 2012, **225**, 81–92.
8 K. Kobzar, S. Ehni, T. E. Skinner, S. J. Glaser and B. Luy, *J. Magn. Reson.*, 2012, **225**, 142–160.
9 T. E. Skinner, T. O. Reiss, B. Luy, N. Khaneja and S. J. Glaser, *J. Magn. Reson.*, 2004, **167**, 68–74.
10 T. E. Skinner, K. Kobzar, B. Luy, M. R. Bendall, W. Bermel, N. Khaneja and S. J. Glaser, *J. Magn. Reson.*, 2006, **179**, 241–249.
11 E. Kupče and R. Freeman, *J. Magn. Reson.*, 1994, **108**, 268–273.
12 E. Kupče and R. Freeman, *J. Magn. Reson.*, 1995, **117**, 246–256.
13 G. Garwood and L. DelaBarre, *J. Magn. Reson.*, 2001, **153**, 155–177.
14 J. M. Bohlen, M. Rey and G. Bodenhausen, *J. Magn. Reson.*, 1989, **84**, 191–197.
15 J. M. Bohlen, I. Burghardt, M. Rey and G. Bodenhausen, *J. Magn. Reson.*, 1990, **90**, 183–191.
16 J. M. Bohlen and G. Bodenhausen, *J. Magn. Reson., Ser. A*, 1993, **102**, 293–301.
17 V. L. Ermakov, J. M. Bohlen and G. Bodenhausen, *J. Magn. Reson., Ser. A*, 1993, **103**, 226–229.
18 V. L. Ermakov and G. Bodenhausen, *Chem. Phys. Lett.*, 1993, **204**, 375–380.
19 K. E. Cano, M. A. Smith and A. J. Shaka, *J. Magn. Reson.*, 2002, **155**, 131–139.
20 D. G. Norris, *Concepts Magn. Reson.*, 2002, **142**, 89–101.